

REPORT DOCUMENTATION PAGE			Form Approved OMB No. 0705-0188	
1. AGENCY USE ONLY (Leave blank)		2. REPORT DATE 950930	3. REPORT TYPE AND DATES COVERED ANNUAL REPORT 2/1/94-6/30/95	
4. TITLE AND SUBTITLE "METHODS FOR CONTROLLING SURFACE FORCES TO INCREASE THE RELIABILITY OF ADVANCE CERAMICS AND THEIR COMPOSITES VIA COLLOIDAL PROCESSING"			5. FUNDING NUMBERS N00014-90-J-1441	
6. AUTHOR(S) FRED F. LANGE				
7. PERFORMING ORGANIZATION NAME(S) AND ADDRESS(ES) MATERIALS DEPARTMENT COLLEGE OF ENGINEERING UNIVERSITY OF CALIFORNIA SANTA BARBARA, CA 93106			8. PERFORMING ORGANIZATION REPORT NUMBER	
9. SPONSORING/MONITORING AGENCY NAME(S) AND ADDRESS(ES) OFFICE OF NAVAL RESEARCH MATERIALS DIVISION 800 NORTH QUINCY STREET ARLINGTON, VA 22217-5000			10. SPONSORING/MONITORING AGENCY REPORT NUMBER	
11. SUPPLEMENTARY NOTES				
<div style="text-align: center;"> <p><del>19951019 021</del></p> <p>19970717 141</p> </div>				
<b>DISTRIBUTION STATEMENT A</b> <b>Approved for Public Release</b> <b>Distribution Unlimited</b>				
13. ABSTRACT (Maximum 200 words) <p>During FY 95, we have discovered a number of important phenomena towards our research goal. Tech. Rept. # 15 shows that elastic modulus and yield stress measurements can be used the particle pair potential, and shows that the a modified version of the classic DLVO theory could be used to explain the short-range repulsive potential produced by salt additions to dispersed, aqueous slurries. Tech. Rept. #13 shows that the bodies reformed via the VibraForming Method previous developed under this program (US Patent: US 5,188,780) could be gel by changing the pH in-situ via a urea decomposition. Tech. Rept. #12 and 16 show that cracking can be avoided in laminar composites, despite large differential strain that are produce either during processing or cooling, if the layers are less than a critical thickness. Tech. Rept #17 shows that laminar composites can be produced were thin layers under biaxial compressive stress cause cracks to bifurcate instead of passing through the layer. This is the first time that residual stresses have been shown to cause crack bifurcation. Laminate were prepared with crack bifurcating layers failed by sequential crack extension; specimens could be unloaded prior to failure.</p>				
14. SUBJECT TERMS Advance Ceramics, Composites, Colloidal			15. NUMBER OF PAGES 108	
DTIC QUALITY INSPECTED 8			16. PRICE CODE	
17. SECURITY CLASSIFICATION OF REPORT UNCLASSIFIED	18. SECURITY CLASSIFICATION OF THIS PAGE UNCLASSIFIED	19. SECURITY CLASSIFICATION OF ABSTRACT UNCLASSIFIED	20. LIMITATION OF ABSTRACT	



DEPARTMENT OF THE NAVY  
OFFICE OF NAVAL RESEARCH  
SEATTLE REGIONAL OFFICE  
1107 NE 45TH STREET, SUITE 350  
SEATTLE WA 98105-4631

IN REPLY REFER TO:

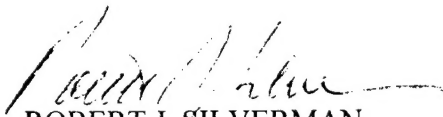
4330  
ONR 247  
11 Jul 97

From: Director, Office of Naval Research, Seattle Regional Office, 1107 NE 45th St., Suite 350, Seattle, WA 98105  
To: Defense Technical Center, Attn: P. Mawby, 8725 John J. Kingman Rd., Suite 0944, Ft. Belvoir, VA 22060-6218

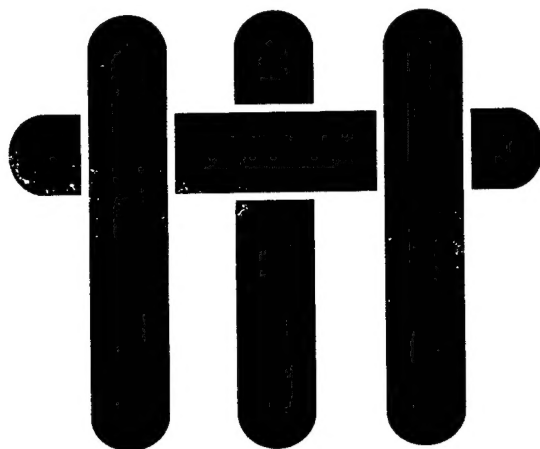
Subj: RETURNED GRANTEE/CONTRACTOR TECHNICAL REPORTS

1. This confirms our conversations of 27 Feb 97 and 11 Jul 97. Enclosed are a number of technical reports which were returned to our agency for lack of clear distribution availability statement. This confirms that all reports are unclassified and are "APPROVED FOR PUBLIC RELEASE" with no restrictions.

2. Please contact me if you require additional information. My e-mail is [silverr@onr.navy.mil](mailto:silverr@onr.navy.mil) and my phone is (206) 625-3196.

  
ROBERT J. SILVERMAN

# **M A T E R I A L S**



## **Effect of Surface Forces on the Rheology of Particle-Liquid Systems and the Consolidation of Ceramic Powders**

### **Second Annual Report and Technical Reports 12, 13, 14, 15, 16 and 17**

**February 1, 1994 through January 31, 1995**

**Office of Naval Research**

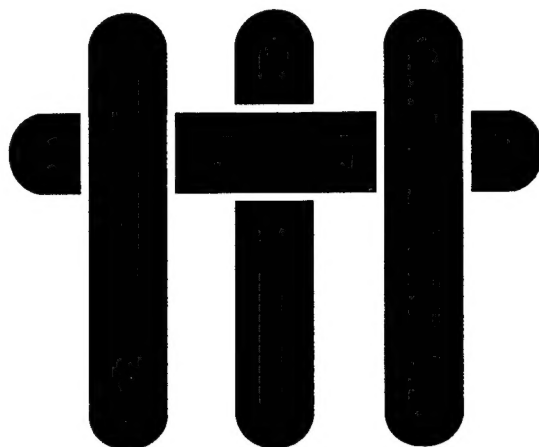
**Grant No. N00014-90-J-1441**

**Fred F. Lange**

**Principal Investigator**

**Materials Department  
University of California  
Santa Barbara, CA 93106**

# M A T E R I A L S



Technical Report Number 12

## Surface Cracking in Layers Under Biaxial, Residual Compressive Stress

S. Ho , C. Hillman, F. F. Lange and Z. Suo

Published in: J. Am. Ceram. Soc. 78 [9] 2353-59 (1995)

February 1, 1994 through January 31, 1995

Office of Naval Research

Grant No. N00014-90-J-1441

Fred F. Lange

Principal Investigator

Materials Department  
University of California  
Santa Barbara, CA 93106



# Surface Cracking in Layers Under Biaxial, Residual Compressive Stress

S. Ho,<sup>†</sup> C. Hillman,<sup>\*</sup> F. F. Lange,<sup>\*</sup> and Z. Suo

Materials Department, University of California, Santa Barbara, California 93106

Thin two-phase,  $\text{Al}_2\text{O}_3/t\text{-Zr(3Y)}\text{O}_2$  layers bounded by much thicker  $\text{Zr(3Y)}\text{O}_2$  layers were fabricated by co-sintering powders. After cooling, cracks were observed along the center of the two-phase,  $\text{Al}_2\text{O}_3/t\text{-Zr(3Y)}\text{O}_2$  layers. Although the  $\text{Al}_2\text{O}_3/t\text{-Zr(3Y)}\text{O}_2$  layers are under residual, biaxial compression far from the surface, tensile stresses, normal to the center line, exist at and near the surface. These highly localized tensile stresses can cause cracks to extend parallel to the layer, to a depth proportional to the layer thickness. A tunneling/edge cracking energy release rate function is developed for these cracks. It shows that for a given residual stress, crack extension will take place only when the layer thickness is greater than a critical value. A value of the critical thickness is computed and compared with an available experimental datum point. In addition, the behavior of the energy release rate function due to elastic mismatch is calculated via the finite element method (FEM). It is also shown how this solution for crack extension can be applied to explain cracking associated with other phenomena, e.g., joining, reaction couples, etc.

## I. Introduction

ATTENTION has been drawn to cracking in layered materials caused by residual stresses, because the problem frequently appears in adhesive joining, electronic packaging, and other technologies. When fabricated at an elevated temperature,  $T_0$ , and cooled to  $T$ , the two materials that form the layered system studied here suffer a mismatch strain of

$$\epsilon_M = \int_{T_0}^T (\alpha_2 - \alpha_1) dT \quad (1)$$

where  $\alpha_1$  and  $\alpha_2$  are the thermal expansion coefficients of the two materials.

Consider a laminate of a balanced stacking sequence of the two materials so the laminate does not bend. Denote  $t_1$  and  $t_2$  as the thicknesses of layers formed with materials 1 and 2, respectively. Far away from the free surface, the residual stress,  $\sigma_{R1}$ , in each layer is uniform and biaxial. The stress perpendicular to the layers, far from the free surface, is zero ( $\sigma_z = 0$ ). In the layer with the lower thermal expansion coefficient (material 1), the residual, biaxial compressive stress is given by

$$\sigma_{R1} = -\frac{\epsilon_M E_1'}{1 + \frac{t_1 E_1'}{t_2 E_2'}} \quad (2)$$

and in the layer with the greater thermal expansion coefficient (material 2), the biaxial, tensile stress is given by

$$\sigma_{R2} = -\sigma_{R1} \frac{t_1}{t_2} \quad (3)$$

Here  $E' = E/(1 - \nu)$ , where  $E$  and  $\nu$  are Young's modulus and Poisson's ratio. For the situation where  $t_1/t_2 \rightarrow 0$ , the biaxial stress in material 1 reduces to

$$\sigma_{R1} = -\frac{E_1}{1 - \nu_1} \epsilon_M \quad (4)$$

and the stress in material 2 vanishes ( $\sigma_{R2} \rightarrow 0$ ). For the experimental case considered below, subscripts 1 and 2 distinguish the thinner  $\text{Al}_2\text{O}_3/t\text{-Zr(Y)}\text{O}_2$  two-phase layers from the thicker  $t\text{-Zr(Y)}\text{O}_2$  layers, respectively. As shown in Table I,  $\alpha_1 < \alpha_2$ , and thus, biaxial, residual compressive stresses develop within the thinner  $\text{Al}_2\text{O}_3/t\text{-Zr(Y)}\text{O}_2$  two-phase layers far from the free surface, whereas the much thicker  $t\text{-Zr(Y)}\text{O}_2$  layers are nearly stress free.

It is well known that the stresses at the free surface of layered materials are different from those within the body of the material. Finite element calculations<sup>1,2</sup> show that although biaxial stresses exist far from the surface, a stress perpendicular to the layer plane exists near the free surface that is highly localized, decreasing rapidly from the surface to become negligible at a distance approximately on the order of the layer thickness. This stress has a sign opposite to that of the biaxial stresses deep within the layer. Thus, when the biaxial stresses are compressive deep within the material (case reported below), there is a tensile stress perpendicular to the layer at and near the surface. This reversal of stresses was also observed by Cox<sup>3</sup> during his analysis of inclusions located either within a body or at the surface. Thus, a tensile stress field, localized near the surface, will be present in layers when the stress far from the surface is biaxial compression. These tensile surface stresses can cause the extension of preexisting cracks.

It has been shown that the condition for crack extension within a highly localized stress field depends on both the magnitude of the tensile stress and the size of the body that gives rise to the stress field. This is independent of whether the stress field is residual<sup>4</sup> (e.g., differential thermal expansion) or an applied local stress<sup>5</sup> (e.g., contact stress). Strain energy release rate functions ( $G$ ) describing the condition for crack extension within thin films and layered materials have been recently reviewed.<sup>6</sup> These functions can be expressed as

$$G = \frac{Z\sigma^2 t}{E} \quad (5)$$

where  $\sigma$  is the tensile stress within the film or layer,  $t$  is the thickness,  $\bar{E} = E/(1 - \nu^2)$ , and  $Z$  is a dimensionless number that depends on the specific system. Although the topic of surface stresses in embedded layers was not reviewed in Ref. 6, Evans and co-workers<sup>7,8</sup> have analyzed a layered system where a thin metal layer joined two thicker ceramic layers. The thin metal layer was under biaxial tension far from the free surface and its surface was in a state of compression normal to the metal/ceramic interface. Tensile stresses were localized at the surface of the ceramic layers, close to the metal layer, and a strain energy release rate function similar to Eq. (5) was derived to explain the surface cracks observed in the ceramic layers.

M. Thouless—contributing editor

Manuscript No. 192983. Received December 7, 1994; approved April 3, 1995. Supported by the Defense Advanced Research Projects Agency through the University Research Initiative under the Office of Naval Research Contract No. N-0014-92-J-1808 and the Office of Naval Research Grant No. N00014-90-J-1441.

<sup>\*</sup>Member, American Ceramic Society.

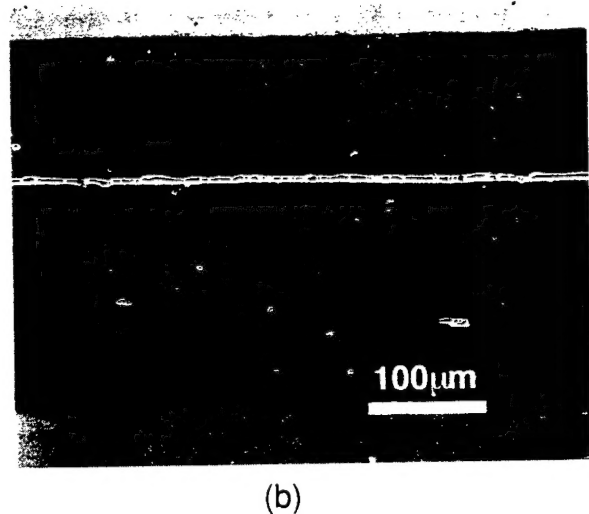
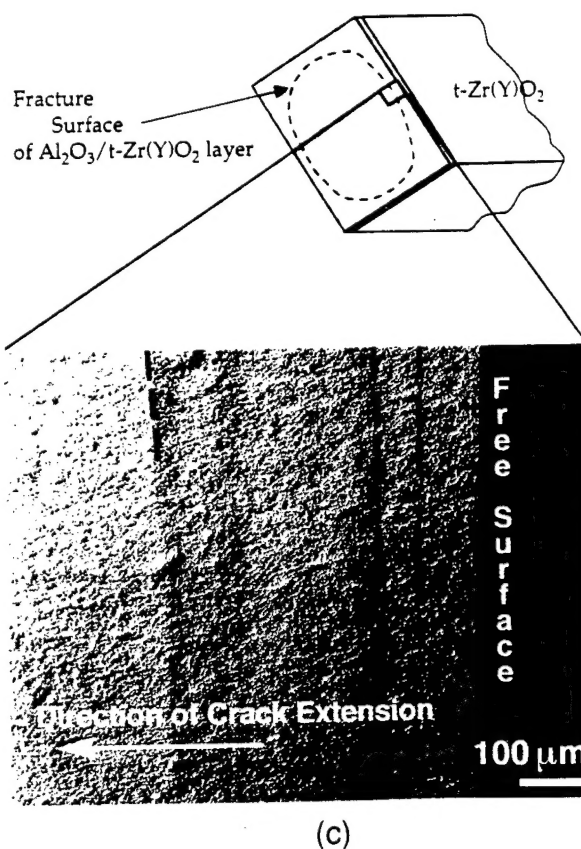
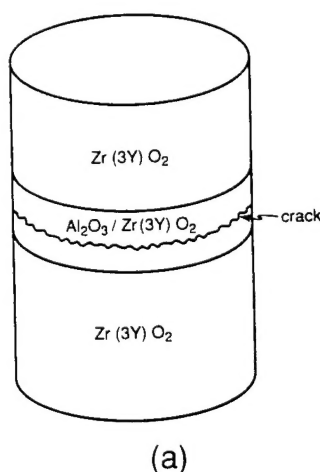
<sup>†</sup>Present address: Department of Theoretical and Applied Mechanics, University of Illinois, Urbana, Illinois 61801.

Table I. Material Parameters

	$\alpha$ ( $\times 10^{-6}/K$ )	$E$ (GPa)	$\nu$	$\Gamma$ (J/m <sup>2</sup> )
Al <sub>2</sub> O <sub>3</sub> /t-Zr(Y)O <sub>2</sub>	11.5 <sup>23</sup>	300 <sup>24,25</sup>	0.32 <sup>26,27</sup>	58 <sup>23</sup>
t-Zr(Y)O <sub>2</sub>	12.5 <sup>23</sup>	205 <sup>24</sup>	0.32 <sup>27</sup>	95 <sup>24</sup>

In the present paper, thin alumina–zirconia composite layers were fabricated between two thicker layers of zirconia at high temperature by co-sintering powders. After the laminate cooled to room temperature, a crack was observed along the center line of the alumina–zirconia layer. When the sample was diamond cut normal to the interfaces, similar cracks were observed on all fresh surfaces. Figure 1 shows a schematic diagram and a micrograph. Obviously, the biaxial compressive stress cannot cause cracks in the alumina–zirconia layer. A more careful study reveals that the phenomenon is a surface effect. Near the

surface, the stress is nonuniform in each layer and differs from that given in Eq. (4). In particular, the alumina–zirconia layer is under tension in the direction perpendicular to the layer plane. As illustrated in Fig. 2, the thin alumina–zirconia layer strives to contract less than the two zirconia layers, bending its surface and thereby inducing the tensile stress. Consequently, if a condition for crack extension exists due to the tensile stresses near the free surface, the crack should extend only to a certain depth. The purpose of this paper is to use a simplified elastic analysis to determine surface stresses in a layer under residual biaxial



**Fig. 1.** (a) A thin layer of Al<sub>2</sub>O<sub>3</sub>/Zr(Y)O<sub>2</sub> is bonded between two blocks of Zr(Y)O<sub>2</sub>. A crack runs parallel to the interfaces, in the Al<sub>2</sub>O<sub>3</sub>/Zr(Y)O<sub>2</sub> layer. (b) An optical micrograph of a crack running in the Al<sub>2</sub>O<sub>3</sub>/Zr(Y)O<sub>2</sub> layer. (c) SEM micrograph of fracture surface showing sequential positions of the crack front (partial dashed lines) extending from the surface near the center of the Al<sub>2</sub>O<sub>3</sub>/Zr(Y)O<sub>2</sub> layer.

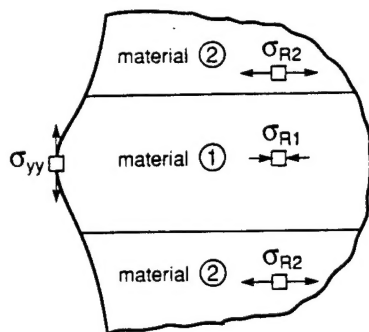


Fig. 2. Far away from the edge, the stress is biaxial in the plane of the laminate, compressive in  $\text{Al}_2\text{O}_3/\text{Zr}(\text{Y})\text{O}_2$ , and tensile in  $\text{Zr}(\text{Y})\text{O}_2$ . At the edge, there is a tensile stress normal to the interfaces in  $\text{Al}_2\text{O}_3/\text{Zr}(\text{Y})\text{O}_2$ .

compression far from the free surface, and to show how these surface stresses can induce cracking.

## II. Experiments

Microlaminates consisting of thin layers of  $\text{Al}_2\text{O}_3/t\text{-Zr}(\text{Y})\text{O}_2$  ( $\approx 300 \mu\text{m}$ ) sandwiched between thick layers of  $t\text{-Zr}(\text{Y})\text{O}_2$  ( $\approx 3000 \mu\text{m}$ ) were fabricated by sequential centrifugation. This method was previously used by Marshall *et al.*<sup>9</sup> to fabricate a new, multilayer laminate with increased fracture toughness. The method utilizes a new colloidal processing technique<sup>10,11</sup> where a short-range repulsive potential is produced by adding salt (e.g.,  $\text{NH}_4\text{Cl}$ ) to a dispersed, aqueous slurry. The short-range repulsive potential produces a weakly attractive particle network that allows particles to pack to a high relative density by either pressure filtration<sup>10,11</sup> or centrifugation,<sup>12</sup> and prevents mass segregation during centrifugation.<sup>13</sup>

A dispersed, aqueous slurry containing 0.10 volume fraction of  $t\text{-Zr}(\text{Y})\text{O}_2$  powder (TZ-3Y, Tosoh, Tokyo, Japan;  $\text{ZrO}_2$  with a tetragonal structure containing 3 mol%  $\text{Y}_2\text{O}_3$ ) was prepared at pH 2; 1.0M  $\text{NH}_4\text{Cl}$  was then added to create a weakly attractive network. This slurry was used to produce the  $t\text{-Zr}(\text{Y})\text{O}_2$  layers in the laminate. A second slurry, used to produce the layers with a lower thermal expansion coefficient, was prepared to contain 0.005 volume fraction of two powders (0.50 volume fraction  $\text{Al}_2\text{O}_3$  (AKP-50, Sumitomo Chemical Co., New York) plus 0.50 volume fraction  $t\text{-Zr}(\text{Y})\text{O}_2$  at pH 2 with 1.0M  $\text{NH}_4\text{Cl}$  to produce a weakly attractive particle network that prevents phase segregation. A volume  $V$  of the appropriate slurry containing the volume fraction of powder,  $\phi$ , was poured into the centrifuge tube, of area  $A$ , to form a layer of thickness

$$t = \frac{V\phi}{A}$$

Thus, by varying either the volume fraction of powder in the slurry or the volume poured into the tube, one could vary the desired layer thickness formed during centrifugation. For the current study, the predetermined volume of the  $t\text{-Zr}(\text{Y})\text{O}_2$  slurry was poured into a 50 mL polyethylene centrifuge tube (Nalgene) and centrifuged at 3200 rpm (centrifugal acceleration  $\sim 1900g$ ) for 2 h (optimum time for maximum particle packing density determined by Ref. 13). The tubes were accelerated slowly up to the highest speed to ensure a smooth surface, and a uniform layer thickness. After centrifugation of the  $t\text{-Zr}(\text{Y})\text{O}_2$  slurry, the clear supernatant was poured off, a predetermined volume of the  $\text{Al}_2\text{O}_3/\text{Zr}(\text{Y})\text{O}_2$  slurry was introduced into the tube for centrifugation. This process was repeated until the desired number of layers was achieved, i.e., by sequential centrifugation.

The laminates were air-dried and then heated at  $2^\circ\text{C}/\text{min}$  to  $1500^\circ\text{C}$  for 1 h to produce dense laminates. The laminates were sectioned by diamond cutting, polished, and then examined with a scanning electron microscope (SEM) (840 SEM, JEOL, Tokyo, Japan). Cracks, parallel to the interface, were observed near the centerline of the  $\text{Al}_2\text{O}_3/\text{Zr}(\text{Y})\text{O}_2$  layers (Fig. 1(b)).

To investigate the depth of the cracks, a flexural bar specimen ( $3.6 \text{ mm} \times 8.5 \text{ mm} \times 20 \text{ mm}$ ) was prepared such that the thin  $\text{Al}_2\text{O}_3/\text{Zr}(\text{Y})\text{O}_2$  layer containing the crack was at the center of the bar. When the specimen was loaded in 3-point bending, it failed from the preexisting crack in the thin  $\text{Al}_2\text{O}_3/\text{Zr}(\text{Y})\text{O}_2$  layer. When the fracture surface was observed in the scanning electron microscope, the position of the crack front prior to catastrophic extension by mechanical testing could be distinguished by a slight change in the crack plane, which clearly marked the crack front. In addition, as shown in Fig. 1(c), several other crack front positions were observed, each apparently caused during cooling by sudden crack extension and arrest. The deepest crack, i.e., the crack front position produced by mechanical fracture, extended from the surface by  $550 \mu\text{m}$ . The thickness of the  $\text{Al}_2\text{O}_3/\text{Zr}(\text{Y})\text{O}_2$  layer containing the crack was  $327 \mu\text{m}$ , i.e., the normalized crack depth was  $a/t = 1.68$ .

## III. Mechanics

### (1) Stress Distribution Prior to Cracking

The stress given by Eq. (4) prevails inside the alumina-zirconia layer, well away from the surface. Near the surface, the stress distribution is much more complex. To appreciate significant features, we first analyzed a simplified problem. Consider a thin layer of material 1 (thickness  $t_1$ ) bonded by two much thicker layers of material 2 (thickness  $t_2$ ), assuming that the two materials have different thermal expansion coefficients but identical elastic constants and that  $t_1/t_2 \rightarrow 0$ . Both materials are fabricated, without bonding, at high temperatures so that their areas are identical before they are cooled. At a lower temperature, the area of the lower expanding material (1) will be larger than the area of material 2. The stress field can be obtained analytically as follows.

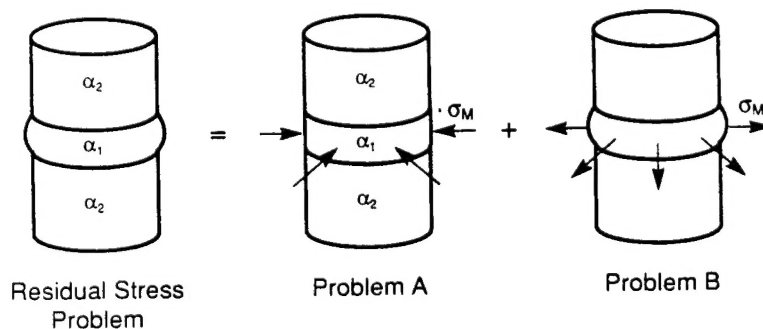


Fig. 3. The residual stress problem is a superposition of the following two problems: (problem A) a band of pressure of magnitude  $\sigma_M$  is applied in addition to the thermal mismatch; (problem B) a band of tensile traction of magnitude  $\sigma_M$  is applied, and there is no thermal mismatch.

The stress induced by thermal mismatch is calculated by superimposing problems A and B in Fig. 3. In problem A, the three layers are detached from one another and a compressive traction of magnitude

$$\sigma_M = \frac{E}{1-\nu} \epsilon_M \quad (6)$$

is applied at the edge of the thin layer, so that the areas of the two materials are perfectly matched. The stress distribution in problem A is trivial: the two thick layers are stress-free, and the thin layer is under biaxial compression of magnitude  $\sigma_M$  in the plane of the layer. In problem B, the specimen consists of the three bonded layers, all of which are stress-free: a tensile traction of magnitude  $\sigma_M$  is applied to the thin layer. The superposition of A and B gives just what we want: the stress field induced by the thermal expansion mismatch strain alone, with no surface tractions.

We are interested only in the stress field in the region scaled by the layer thickness; all other lengths—the size of the block and the diameter of the layer—are deemed too large to be relevant. This is a proper assumption for many materials with an embedded layer. Consequently, problem B can be further simplified to be a plane strain problem, i.e., a semi-infinite solid subjected to a band of surface tractions, which is simply a set of point forces along the thickness of the embedded layer (inset Fig. 4). This problem is readily solved by integrating the solution for a point force on a free surface<sup>14</sup> over the band where the tractions are applied. Figure 4 shows the distribution of the stress component  $\sigma_{yy}$  in problem B. This is also the distribution of the residual stress, since the stress component  $\sigma_{yy}$  vanishes in problem A. The centerline of the thin layer coincides with the  $x$ -axis. On the surface ( $x = 0$ ),  $\sigma_{yy}$  is a step-function, equal to  $\sigma_M$  in the thin layer,  $\sigma_M/2$  at the interface, and zero in the two thick layers. Along the centerline ( $y = 0$ ), the stress is given by

$$\sigma_{yy}(x)|_{y=0} = \frac{2}{\pi} \left[ \theta - \frac{1}{2} \sin 2\theta \right] \sigma_M \quad (7)$$

where  $\tan \theta = t/2x$ . For large depth  $x$ , i.e.,  $\theta \rightarrow 0$ , this stress decays as

$$\frac{\sigma_{yy}}{\sigma_M} \rightarrow \frac{4}{3\pi} \theta^3 \rightarrow \frac{1}{6\pi} \left( \frac{t}{x} \right)^3$$

Equation (7) is labeled as  $y/t = 0$  in Fig. 4. A similar solution was derived in Ref. 3.

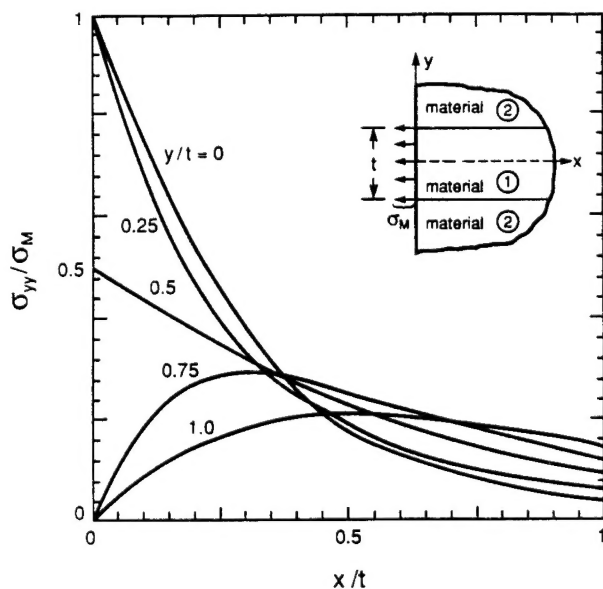


Fig. 4. Distribution of the stress component  $\sigma_{yy}(x,y)$  near the edge. The elastic mismatch in this system is assumed to be zero.

The results from Fig. 4 correspond well with the values determined via FEM by Kirchner *et al.*,<sup>2</sup> considering the limitations of FEM for small embedded layers and that Fig. 4 assumes no elastic mismatch.

## (2) Edge and Channel Cracking

Interacting with preexisting flaws, the tensile stress in Eq. (7) may induce crack extension. Figure 5 illustrates that two situations must be considered; one, the extension of a pre-existing crack into the thin layer to a depth  $a$  (termed "edging"), and second, the extension of a crack of depth  $a$  along the center line of the thin layer (termed "channeling"). Plane strain conditions apply if it is assumed that crack extension into the layer prevails as the crack extends along the center line. The strain energy release rate,  $G_{ED}$ , for extension into the layer (edging) is given by<sup>15</sup>

$$\frac{G_{ED} \bar{E}}{\sigma_M^2 t} = \frac{a}{t} s^2 \{ 1.122 - (1-s) \cdot [0.296 + 0.25s^{3/4}(0.75-s)] \}^2 \quad (8)$$

Here

$$\bar{E} = E/(1-\nu^2)$$

$$s = \frac{2}{\pi} \tan^{-1} \left( \frac{t}{2a} \right)$$

Equation (8) is plotted in Fig. 6 to show that as the crack depth  $a$  increases,  $G_{ED}$  increases when  $a$  is small, reaching the maximum at  $a \approx 0.3t$ , and then drops when  $a$  is large. This trend is expected because the tensile stresses are localized near the surface.

If the critical strain energy release rate of the thin layer material is  $\Gamma$ , then for crack propagation to occur,

$$G_{ED} = \Gamma \quad (9)$$

Graphically, this is analogous to drawing a horizontal line corresponding to  $\Gamma$  normalized by  $\bar{E}/\sigma_M^2 t$  in Fig. 6. When the residual stress becomes large enough during cooling, this line will intersect the  $G_{ED}$  curve at two points, corresponding to two crack depths. The larger depth is the crack's stable, equilibrium position; it will not grow deeper unless the residual stress increases because of a further decrease in temperature.

The strain energy release rate for channeling,  $G_{CH}$ , can be computed using<sup>16</sup>

$$G_{CH} = \frac{1}{a} \int_0^a G_{ED} da \quad (10)$$

This result is also plotted in Fig. 6. The overall trends for the two strain energy release rate functions are similar. At  $a = 0.55t$ , the  $G_{CH}$  function reaches its maximum value

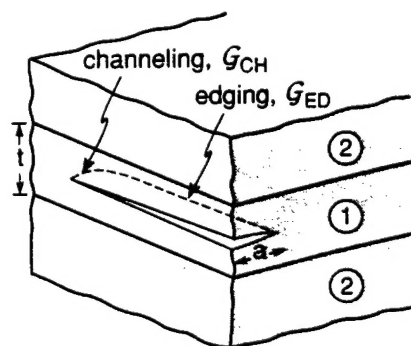


Fig. 5. Two crack fronts: extension deeper into the layer (edging) and spreading around the layer (channeling). The tensile traction  $\sigma_M$  is applied on the surface of layer 1 (not shown in the figure).

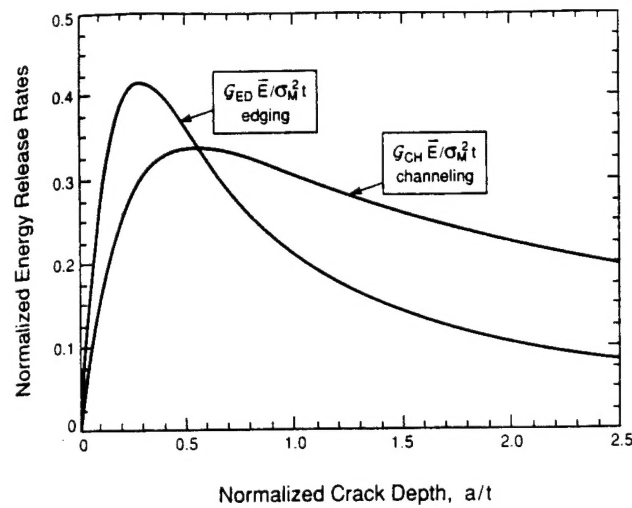


Fig. 6. The energy release rates of edging  $G_{ED}$  and channeling  $G_{CH}$  vary with the crack depth  $a$ . Elastic mismatch is assumed to be zero.

$$(G_{CH})_{\max} = \frac{0.34\sigma_M^2 t}{E} \quad (11)$$

No preexisting crack can channel along the layer when

$$(G_{CH})_{\max} < \Gamma \quad (12)$$

Combining Eqs. (11) and (12), one finds that channeling is possible only when

$$\frac{\Gamma \bar{E}}{\sigma_M^2 t} \leq 0.34 \quad (13)$$

Consequently, for a given material pair cooled to a prescribed temperature, there exists a critical thickness,  $t_c$ , below which channeling cannot occur, i.e., when

$$t \leq t_c = \frac{\Gamma \bar{E}}{0.34\sigma_M^2}$$

The following sequence of events is plausible as a laminate is cooled. The stresses increase from zero during cooling from the fabrication temperature. When the stress is low, favorably oriented, preexisting flaws will neither extend to a greater depth nor channel along the surface. As the stress increases during cooling and reaches the level determined by Eq. (13), a single flaw on the surface, of size around  $a = 0.55t$ , will be activated to channel along the layer. If the preexisting flaw is much smaller, larger stresses need to develop before the crack spontaneously both extends to a greater depth and channels. After channeling has occurred once, in a catastrophic manner, the crack can extend to greater depths (greater values of  $a$ ) as the temperature drops further. Because  $G_{ED}$  diminishes for large depths, the crack will stabilize at a larger depth determined by Eqs. (8) and (9).

### (3) Effect of Elastic Mismatch

When the two materials have different elastic constants, we solve the problem by using the finite element method. As illustrated in Fig. 5, a thin layer of Young's modulus  $E_1$  is bonded between two infinite blocks of Young's modulus  $E_2$ . Poisson's ratios are taken to be  $1/3$  for both materials. The elastic mismatch is conveniently described by

$$\frac{E_1 - E_2}{E_1 + E_2} \quad (14)$$

which lies between  $\pm 1$ , and is positive when material 1 is stiffer than material 2. The thin laminate is loaded by a tensile traction  $\sigma_M$  on the edge of layer 1.

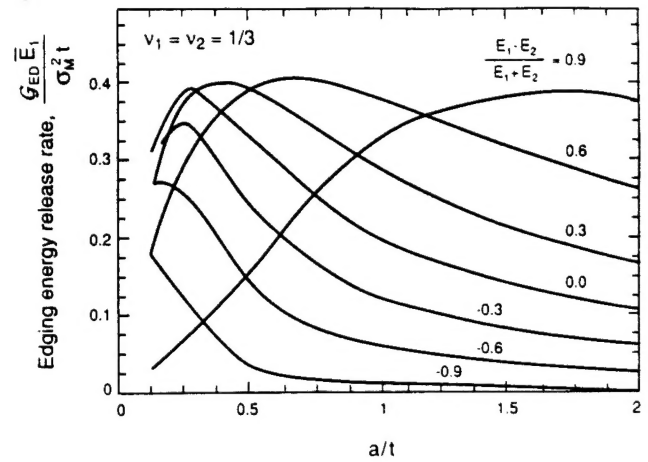


Fig. 7. Edging energy release rate as a function of crack depth and elastic mismatch.

Finite element meshes were generated for various crack sizes,  $a/t$ . The accuracy of each mesh was checked by comparing finite element results for  $E_1 = E_2$  with the solution presented in the previous section. The calculated strain energy release rates for edging ( $G_{ED}$ ) are plotted in Fig. 7, where Young's modulus of the thin layer  $E_1$  was used to normalize the energy release rate. Everything else being fixed, as the two thicker layers become more compliant, the curves spread toward the upper right; i.e., the crack will extend deeper into the thin layer.

Once  $G_{ED}$  is obtained, one can use Eq. (10) to compute  $G_{CH}$ . A more direct approach, more suitable for finite element analysis, is as follows. First the stress distribution  $\sigma_{xx}(x)$  on the line of the prospective crack is computed when there is no crack. Then the crack-opening profile,  $\delta(x)$ , is computed for a traction-free crack. Both computations are done using the finite element method. The channeling energy release rate is calculated by integrating<sup>17</sup>

$$G_{CH} = \frac{1}{2a} \int_0^a \sigma_{xx}(x) \delta(x) dx \quad (15)$$

The computed results are plotted in Fig. 8. Everything else being fixed, both the maximum,  $(G_{CH})_{\max}$ , and the depth where the maximum occurs increase as the two thicker layers become more compliant.

Crack channeling cannot occur when Eq. (12) is satisfied. The maximum on each curve in Fig. 8 is plotted in Fig. 9 as a function of the elastic mismatch ratio. For a given elastic mismatch, channel cracking is not possible when the dimensionless

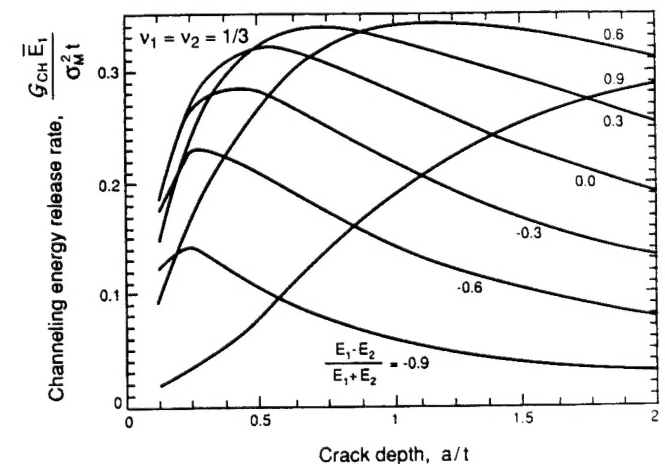


Fig. 8. Channeling energy release rate as a function of crack depth and elastic mismatch.



group,  $\Gamma \bar{E}_1 / \sigma_m^2 t$ , lies above the curve; this region is labeled "no cracking."

#### IV. Discussion

We have developed an analytical expression for the distribution of tensile stresses at and near the surface of a layer that is under biaxial compression far from the surface. These stresses are consistent with the surface crack observed to bisect the layer. We have also developed critical strain energy release rate functions that describe how far a surface crack will extend into the layer and when it will spontaneously extend along the layer. As for other cases where the tensile stress is highly localized,<sup>1,4-8</sup> it is shown that spontaneous extension along the layer can occur only when the dimensionless group,  $\Gamma \bar{E}_1 / \sigma_m^2 t$ , exceeds a critical value. That is, for a given set of material properties and residual stress, crack extension along the layer will not occur when the layer thickness is less than a critical value.

The strain energy release rate function, Eq. (8), can be tested by comparing the experimental value of the crack depth obtained by observing the fracture surface of the materials used in the current work with the value predicted with Eq. (8). A value of the normalized strain energy release rate of 0.17 is obtained by substituting the experimental crack depth/layer thickness ratio of 1.68 reported above into the right-hand side of Eq. (8) and using a value for the elastic mismatch parameter (Eq. (14)) of 0.2 for the current materials. Using the material properties in Table I, a value of 0.156 was obtained for the left-hand side of Eq. (8). The two values obtained from each side of Eq. (8), 0.17 vs. 0.156, appear to be in sufficient agreement to suggest that Eq. (8) can produce a good estimate for the condition for crack extension, given that the elastic mismatch is small.

The phenomenon described here can be important in many technical situations including the processing and use of multilayer materials, such as capacitors, electronic packaging, piezoelectric actuators, and laminar composites. In these applications, residual stresses arise during the codensification of powder layers due to differential shrinkage, and during cooling from the densification temperature due to differential thermal contraction. For example, in electronic packaging, layers of ceramics and metals are bonded together; the ceramic layers are typically under residual compression far away from the free surface, but under tensile stress at the free surface.

Other important applications include reaction layers formed between two materials at elevated temperatures and bonded joints. Reaction layers can develop between two materials at elevated temperatures. When the reaction product has a larger molar volume, the reaction layer is under biaxial compression far from the free surface but under tension at the surface. An example of this is cited in Ref. 18, where the reaction between nickel and  $\text{Al}_2\text{O}_3$  produces a spinel layer that results in an extremely weak joint. Since reactions often produce large molar volume changes, and thus, linear strains much larger than those associated with differential thermal expansion, the critical thickness of the reaction layer for spontaneous crack extension can be only a few nanometers; the depth of the crack is expected to increase as reaction proceeds to produce a thicker reaction layer.

Residual stresses can also arise when materials are bonded together with a third material (adhesives, brazes, etc.). In practice, it is well known that the strength of the join depends not only on the magnitude of the residual stress (due to the properties of the third material), but also on the thickness of the joining layer. For example, Kirchner *et al.*<sup>2</sup> have shown that the strength of joints produced between ceramics bonded together with a glass increases with decreasing glass bond thickness, although the maximum tensile stress at the surface was found, by finite element analysis, to be independent of the bond layer thickness. For cases such as these, where a tensile stress is superimposed on the residual tensile stress, the critical bond

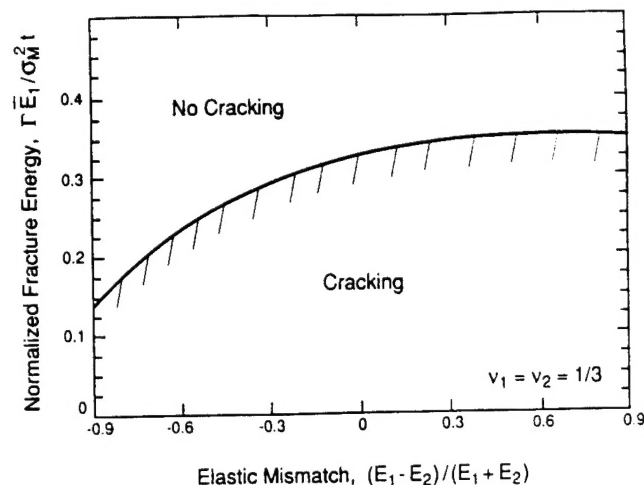


Fig. 9. Condition for the channel cracking to be suppressed.

layer thickness for spontaneous crack extension (i.e., fracture) will depend on the applied to residual stress ratio. Although the critical stress intensity function for this superimposed stress problem is beyond the scope of the present work, its solution is expected to show that the strength of the bonded joint will approach the statistical strength of the ceramic with decreasing bond layer thickness.

Other problems of a similar nature, involving fibers and inclusions under an apparent compressive stress, have been cited in the literature. Cracks have also been observed in fiber-reinforced composites. If fibers have a smaller thermal expansion coefficient than the matrix, the fibers within the matrix are placed under compressive stresses in all three directions during cooling from the processing temperature. However, at the free surface of the composite, tensile stresses develop in the direction normal to the fiber axis. A crack can channel along the fiber if the dimensionless group,  $\Gamma E / \sigma_m^2 R$ , exceeds a critical number.<sup>19</sup> Here  $\Gamma$ ,  $E$ , and  $R$  are the critical strain energy release rate, Young's modulus, and the radius of the fiber, and  $\sigma_m$  is the mismatch stress.

For inclusions, Lange and Metcalf<sup>20</sup> have shown that cracking due to tensile stresses occurs when an inclusion, nominally under compression when fully embedded in a matrix, is truncated by the surface. For this case, the residual stress in a surface inclusion has been analyzed by Cox<sup>3</sup> as a function of the inclusion shape. Analogous to the surface inclusion, when the surface of a brittle material is suddenly heated in a small region, e.g., when the surface is impinged with a melt droplet or a laser beam, the small region expands. The situation commonly gives a false impression that a compressive stress, parallel to the surface, develops at the heated spot. However, a recent analysis<sup>21</sup> has shown that crack extension can occur due to tensile stress parallel to the surface, under the heated spot.

Finally, it should be pointed out that the stress distribution reported above for free surface of an embedded layer is similar to those imposed by the "bridge" loading method, developed by Nose and Fujii,<sup>22</sup> to introduce a crack of finite depth into a bar specimen. With an appropriate testing method and stress intensity function, the cracked bar is used to determine the critical stress intensity factor of the material. The "bridge" is a slotted block. The bar specimen is compressed between the bridge and a flat surface; except for the region between the slot in the bridge, the opposing surfaces of the bar are compressed. At a critical load, a crack suddenly "pops" into the bar between the slot in the bridge. In this loading configuration, the unloaded region in the bar, defined by the slot in the bridge, is analogous to the layer in the problem analyzed above. That is, localized tensile stresses arise within the bar defined by the slot in the bridge. Similar to the conditions for crack extension in the layer, the crack produced by bridge loading only extends into

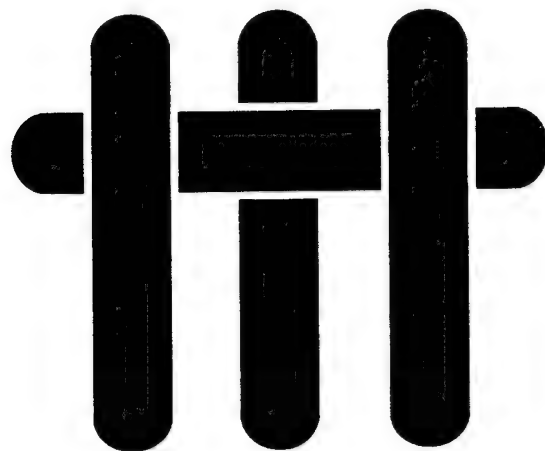
the bar to a depth that is proportional to the width of the slot. Thus, although the loading condition is compressive, localized tensile stresses within the unloaded slot region lead to the sudden extension of a crack that arrests at a depth proportional to the width of the slot.

**Acknowledgment:** Finite element analyses are carried out with ABAQUS.

## References

- <sup>1</sup>N. L. Harrison and W. J. Harrison, "The Stresses in an Adhesive Layer," *J. Adhes.*, **3**, 195-212 (1972).
- <sup>2</sup>H. Kirchner, J. Conway, and A. E. Segall, "Effect of Joint Thickness and Residual Stresses on the Properties of Ceramic Adhesive Joints: I. Finite Element Analysis of Stresses in Joints," *J. Am. Ceram. Soc.*, **70** [2] 104-109 (1987).
- <sup>3</sup>B. N. Cox, "Surface Displacements and Stress Generated by a Semi-Ellipsoidal Surface Inclusion," *J. Appl. Mech.*, **56**, 564-70 (1989).
- <sup>4</sup>F. F. Lange, "Criteria for Crack Extension and Arrest in Residual Localized Stress Fields Associated with Second Phase Inclusions," p. 599 in *Fracture Mechanics of Ceramics*, Vol. 2, Edited by R. C. Bradt, D. P. Hasselman, and F. F. Lange, Plenum Press, New York, 1974.
- <sup>5</sup>F. F. Lange, "Crack Extension and Arrest for Contact Stress Fields," *Int. J. Fract.*, **12** [3] 409-17 (1976).
- <sup>6</sup>J. W. Hutchinson and Z. Suo, "Mixed-Mode Cracking in Layered Materials," *Adv. Appl. Mech.*, **29**, 63-191 (1991).
- <sup>7</sup>H. C. Cao, M. D. Thouless, and A. G. Evans, "Residual Stresses and Cracking in Brittle Solids Bonded with a Thin Ductile Layer," *Acta Metall.*, **36** [8] 2037-46 (1988).
- <sup>8</sup>M. Y. He and A. G. Evans, "The Strength and Fracture of Metal/Ceramic Bonds," *Acta Metall.*, **39** [7] 1587-93 (1991).
- <sup>9</sup>D. Marshall, J. Ratto, and F. F. Lange, "Enhanced Fracture Toughness in Layered Microcomposites of Ce-ZrO<sub>2</sub> and Al<sub>2</sub>O<sub>3</sub>," *J. Am. Ceram. Soc.*, **74** [12] 2979-87 (1991).
- <sup>10</sup>B. V. Velamakanni, J. C. Chang, F. F. Lange, and D. S. Pearson, "New Method for Efficient Colloidal Particle Packing via Modulation of Repulsive Lubricating Hydration Forces," *Langmuir*, **6**, 1323-25 (1990).
- <sup>11</sup>J. C. Chang, F. F. Lange, and D. S. Pearson, "Viscosity and Yield Stress of Alumina Slurries Containing Large Concentrations of Electrolyte," *J. Am. Ceram. Soc.*, **77** [1] 19-26 (1994).
- <sup>12</sup>J. C. Chang, F. F. Lange, D. S. Pearson, and J. P. Pollinger, "Compaction of Al<sub>2</sub>O<sub>3</sub> Slurries by Centrifugation: The Effect of Interparticle Potentials," *J. Am. Ceram. Soc.*, **77** [5] 1357-60 (1994).
- <sup>13</sup>J. C. Chang, B. V. Velamakanni, F. F. Lange, and D. S. Pearson, "Centrifugal Consolidation of Al<sub>2</sub>O<sub>3</sub> and Al<sub>2</sub>O<sub>3</sub>/ZrO<sub>2</sub> Composite Slurries vs Interparticle Potentials: Particle Packing and Mass Segregation," *J. Am. Ceram. Soc.*, **74** [9] 2201-204 (1991).
- <sup>14</sup>S. P. Timoshenko and J. N. Goodier, *Theory of Elasticity*, 3rd ed. McGraw-Hill, New York, 1970.
- <sup>15</sup>H. Tada, P. C. Paris, and G. R. Irwin, *The Stress Analysis of Cracks Handbook*, p. 8.11, Del Research, St. Louis, MO, 1985.
- <sup>16</sup>G. Gilie, "Strength of Thin Films and Coatings," Ch. 7 in *Current Topics in Materials Science*, Vol. 12, North-Holland Publishing Co., Amsterdam, Netherlands, 1985.
- <sup>17</sup>S. Ho and Z. Suo, "Tunneling Cracks in Constrained Layers," *J. Appl. Mech.*, **60**, 890-94 (1993).
- <sup>18</sup>K. P. Trumble and M. Ruhle, "The Thermodynamics of Spinel Interphase Formation at Diffusion-Bonded Ni/Al<sub>2</sub>O<sub>3</sub> Interfaces," *Acta Met. Mater.*, **39** [8] 1915-24 (1991).
- <sup>19</sup>J. W. Hutchinson; unpublished work.
- <sup>20</sup>F. F. Lange and M. Metcalf, "Processing-Related Fracture Origins: II. Agglomerate Motion and Cracklike Internal Surfaces Caused by Differential Sintering," *J. Am. Ceram. Soc.*, **66**, 398-406 (1983).
- <sup>21</sup>V. Tvergaard, Z. C. Xia, and J. W. Hutchinson, "Cracking Due to Localized Hot Shock," *J. Am. Ceram. Soc.*, **76**, 729-36 (1993).
- <sup>22</sup>T. Nose and T. Fujii, "Evaluation of Fracture Toughness for Ceramic Materials by a Single-Edge-Pre-cracked-Beam Method," *J. Am. Ceram. Soc.*, **71**, 328-33 (1988).
- <sup>23</sup>C. Hillman and F. F. Lange; unpublished work.
- <sup>24</sup>F. F. Lange, "Transformation Toughening. Part 4: Fabrication, Fracture Toughness and Strength of Al<sub>2</sub>O<sub>3</sub>-ZrO<sub>2</sub> composites," *J. Mater. Sci.*, **17**, 247-54 (1982).
- <sup>25</sup>Dr. Dieter Schneider; private communication.
- <sup>26</sup>K. Wefers and C. Misra, "Oxides and Hydroxides of Aluminum," Alcoa Laboratories, Pittsburgh, PA, 1987.
- <sup>27</sup>B. Eigenmann, B. Scholtes, and E. Macherauch, "Roentgenologic Stress Determination in Ceramics and Metal-Ceramic Composites. Theory and Applications," *Materialwiss. Werkstofftech.*, **20**, 314-25 (1989).

# **M A T E R I A L S**



**Technical Report Number 13**

## **VibraForming and In-situ Flocculation of Consolidate, Coagulated Alumina Slurries**

**George V. Franks, Bhaskar V. Velamakanni, and Fred F. Lange**

**Published in: J. Am. Ceram. Soc. 78 [5] 1324-28 (1995)**

**February 1, 1994 through January 31, 1995**

**Office of Naval Research**

**Grant No. N00014-90-J-1441**

**Fred F. Lange**

**Principal Investigator**

**Materials Department  
University of California  
Santa Barbara, CA 93106**



# VibraForming and *In Situ* Flocculation of Consolidated, Coagulated, Alumina Slurries

George V. Franks,\* Bhaskar V. Velamakanni,\*\* and Fred E. Lange\*

Materials Department, University of California, Santa Barbara, California 93106

Aqueous, alumina slurries dispersed at low pH form weakly attractive networks when excess counterions are added. These slurries can be consolidated to a high relative packing density via either pressure filtration or centrifugation without mass segregation or density gradients. These saturated, consolidated bodies can be reshaped by vibrating them into a complex-shaped die cavity, a process termed VibraForming. The yield stress of these bodies can be increased by adding urea to the slurry before consolidation and then heating the VibraFormed body to change the pH of the water within the body to the isoelectric point for the alumina powder. The increased yield stress, characterized by stress relaxation experiments, allows the body to be removed from the die cavity without shape distortion.

## I. Introduction

LABORATORY<sup>1</sup> and pilot-plant<sup>2</sup> demonstrations have shown that the mean strength of a ceramic can be dramatically increased by removing strength-degrading heterogeneities (agglomerates, inclusions, etc.) from dispersed slurries prior to consolidating the powder into an engineering shape. The heterogeneities are removed by either sedimentation or filtration. More importantly, because strength-degrading heterogeneities greater than a given size are removed, the strengths of the fired bodies exhibit a truncated distribution<sup>2</sup> as if the material was proof tested prior to strength measurements. This greatly lowers the probability that any test specimen (component) will fail below a given minimum stress level.

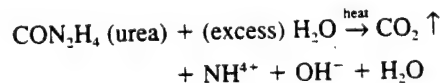
Although long-range, repulsive interparticle potentials are required to produce dispersed slurries that can be filtered, it has been demonstrated<sup>3,4</sup> that once filtered, short-range repulsive potentials are more desirable for further processing and shape forming.<sup>5</sup> Short-range repulsive potentials, combined with the attractive van der Waals potential, produce a weakly attractive particle network (termed a coagulated slurry) that is resistant to mass segregation even during centrifugation.<sup>6</sup> Short-range repulsive potentials also allow particle packing densities near the maximum during consolidation at modest pressures (a few megapascals),<sup>3,7</sup> a packing density that is pressure insensitive,<sup>7</sup> and they produce plastic (claylike) bodies with a modest yield stress (between approximately 0.01 and 0.1 MPa).<sup>8</sup> Short-range repulsive potentials can be produced either by strongly adsorbing short molecules that prevent attractive particles from touching<sup>9,10</sup> or by adding an indifferent electrolyte to a slurry dispersed by the diffuse, electric double-layer method.<sup>3,4</sup>

The diffuse, electric double-layer method, described by the classical Derjaguin-Landau-Verwey-Overbeek (DLVO) theory, allows the slurry to first be dispersed, required for the

removal of heterogeneities via filtration, and then coagulated by simply adding salt. Although the cause of the short-range repulsive potential, first described as a hydration potential,<sup>1</sup> is still a subject of research, it has been shown that once the critical coagulation concentration has been exceeded, the network becomes stronger with increasing concentration of salt.<sup>11</sup> For alumina powders at low pH, the network strength, characterized with viscosity,<sup>3,4</sup> elastic modulus,<sup>11</sup> and yield stress measurements,<sup>4,11</sup> appears to plateau at higher ( $\geq 1.5M$ ) concentrations of salt. For the same slurry, the strength of the coagulated network is significantly lower than that for the network produced at the isoelectric point where only the attractive van der Waals potential persists.

The discovery of weakly attractive particle networks and their attributes for ceramic processing has led to several innovative shape-forming technologies. It was first demonstrated that two-phase, coagulated slurries could be centrifuged without mass and phase segregation to produce a body with a uniform packing density, despite the large pressure gradients inherent to centrifugation.<sup>6</sup> This demonstration showed that complex shapes could be formed by centrifugation and layered composites could be formed by sequential centrifugation.<sup>12</sup> Later it was demonstrated that saturated bodies, consolidated by either centrifugation or pressure filtration, could be fluidized by vibration and made to flow into a complex die cavity despite a particle packing density near (or at) the maximum value for the powder.<sup>5</sup> Although the bodies formed by vibratory shaping would dramatically increase their apparent yield stress as soon as the vibration was turned off, the yield stress was not high enough to allow the body to be pushed out of the die cavity without some shape distortion. As we demonstrate in this paper, the yield stress of the molded body can be dramatically increased by a chemical reaction that causes *in situ* flocculation, that is, by changing the pH of the reformed saturated consolidated powder compact from a low value (pH 4) to the isoelectric point of alumina.

The change in pH can be accomplished by the thermal decomposition of urea, added to the slurry before consolidation, according to



With the appropriate pH change the particles will flocculate at the isoelectric point where the yield strength is significantly increased, as demonstrated by stress relaxation measurements described below.

The authors discovered that similar work was ongoing simultaneously,<sup>13</sup> which used enzyme-catalyzed urea decomposition to change the pH of unconsolidated slurry to create a stiff green body.

## II. Experimental Procedure

### (1) Slurry Preparation

$\alpha$ -Alumina (Sumitomo Chemical Co., New York, Grade APK50) powder with an average particle size of 0.2  $\mu\text{m}$  and a

J. W. Halloran—contributing editor

Manuscript No. 193337. Received August 8, 1994; approved December 7, 1994. Supported by the Office of Naval Research under Contract No. N00014-92-J-1808.

\*Member, American Ceramic Society.

\*\*Now with the 3M Corporate Research Laboratory, 3M Center, St. Paul, Minnesota 55144.

9.9 m<sup>2</sup>/g surface area was prepared as an aqueous slurry containing 0.20 volume fraction of solids at pH 4.0 as described elsewhere.<sup>12</sup> The powder develops a positive surface charge at low pH, reaching a maximum zeta potential of about +60 mV at  $\leq$ pH 5.<sup>14</sup> The zeta potential gradually decreases from its maximum at pH 5 to zero at pH 9. After dispersing at pH 4, the slurry was then either coagulated by the addition of 0.5M NH<sub>4</sub>Cl (Fisher Chemical, Fair Lawn, NJ, analytical grade) to create a weakly attractive network or flocculated by changing the pH to 9. Urea was added to the coagulated slurry at a concentration of 40% of the weight of the water present in the slurry. This reduced the solids loading of the urea-containing slurry to 0.16 volume fraction due to the increased volume of solution. The pH was adjusted to the desired pH ( $\pm 0.1$  pH units) with analytic grades of either HNO<sub>3</sub> or NH<sub>4</sub>OH.

## (2) Consolidation

The slurries were consolidated by pressure filtration as described elsewhere.<sup>15</sup> A predetermined volume of slurry was poured into a pressure filtration cavity (2.54 cm in diameter) to consolidate bodies  $\approx 1.5$  cm in height with a pressure of 8 MPa. Bodies consolidated from the slurry that did not contain urea only required  $\approx 35$  min to reach their equilibrium packing density (recognized when the movement of the die plunger ceased). Bodies consolidated from slurries containing urea required  $\approx 50$  min to reach their equilibrium packing density, due presumably to their lower initial fraction of solids. In all cases, the pressure was maintained for an additional 10 min after reaching their apparent equilibrium packing density. The consolidated bodies were stored in plastic bags containing a piece of paper towel saturated with water. Different bodies were consolidated for measuring relative density, VibraForming experiments, and stress relaxation experiments.

The relative density of the consolidated bodies was determined using the weight difference method. The weight of the consolidated body was determined immediately after pressure filtration, after drying at 60°C for  $>16$  h, and after pyrolyzing all additives (salt and urea) at 350°C for 3 h. The densities were calculated on the basis of the weight contributions of the constituents. It is assumed that only water is removed at 60°C and the NH<sub>4</sub>Cl and urea are removed at 350°C. In this method, the relative density of the powder within the saturated body is determined.

## (3) VibraForming Experiments and In Situ Flocculation

The formulation of slurry used in this work (pH 4 with 0.5M NH<sub>4</sub>Cl) was chosen to produce a consolidated body that would readily liquefy based on the work of Velamakanni *et al.*<sup>8</sup> A small die cavity was designed and fabricated out of aluminum to produce a pseudorotor that incorporated both varying cross section and vanelike protrusions to demonstrate the process capability. Figure 1(a) shows the size and shape of the die cavity. A second, simple cylindrical mold was fabricated so that samples could be reshaped into cylinders to be tested in stress relaxation experiments to determine if the properties of the consolidated body changed after VibraForming and *in situ* flocculation. Silicone grease was used as a mold release agent. The mold with its lid removed was placed on a vibrating table (Cleveland Vibrator Co., Cleveland, OH, Model CM-30). The mold was filled by placing the pressure-filtered, consolidated body containing urea in the die cavity with its cylindrical axis parallel to the horizontal surface of the die cavity. When the vibrating table was turned on, the consolidated body liquefied and flowed under the influence of gravity to fill the mold. Any excess material that overflowed the die cavity was removed before the lid to the die cavity was fastened. It was also found that the die cavity could similarly be filled by tapping the die cavity by hand on a horizontal surface. Once the die cavity was filled, the lid was securely fastened. The die cavity was

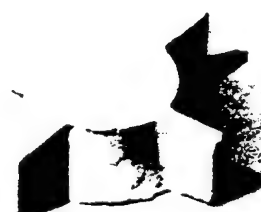
designed to be airtight to prevent any evaporation from the consolidated body during subsequent processing.

The die cavity, filled with the VibraFormed body, was placed in a hot water bath, to initiate the urea decomposition. The hot water bath was chosen over a dry oven due to the better heat transfer characteristics of the liquid. VibraFormed specimens were heat-treated at temperatures between 80° and 95°C and times between 20 and 120 min. After heat treatment, the die cavity was cooled to room temperature (either by quenching in cool water or slowly cooling in air) before being opened. The mold was then opened and the sample removed. A qualitative judgment was made as to whether the sample had sufficient yield stress to be handled. In this way a temperature vs time map was constructed to distinguish between heat treatments that produced either "brittle" or "plastic" bodies. Specimens that were to be mechanically tested were placed in a plastic bag with a piece of saturated paper towel to prevent the sample from drying out before testing. Specimens not designated for mechanical testing were weighed immediately after demolding and then again after drying at 60°C and pyrolyzing at 350°C to calculate relative densities as described above.

No attempt was made to measure the pH of the water in the bodies after heat treatment, although it is assumed that the pH



(a)



(b)

**Fig. 1.** (a) Aluminum mold used to form pseudorotors by VibraForming. The mold outside diameter is 6.35 cm (2.5 in.). (b) Fired alumina pseudorotor produced by VibraForming and *in situ* flocculation process. The outside diameter of the part (including vanes) is 3.3 cm and its height is 0.95 cm.

increased because of the urea decomposition evident by the strong ammonia smell and evidence in a related research program. In the related research program, slurries containing 0.25 volume fraction of the same alumina powder were prepared with urea (20% and 50% by weight of water in the slurry) and were heat-treated at 93°C for 20 min then cooled. The pH of these slurries was measured before and after heat treatment. All samples for both urea levels showed an increase in pH from 4.1 to between 8.1 and 8.5 after the heat treatment.<sup>16</sup> Control samples without urea were heat-treated with the same schedule that produced "brittle" compacts in the urea-containing samples.

After the VibraFormed bodies were removed from the die cavity, dried at 60°C/16 h, and pyrolyzed at 350°C/3 h, they were densified by heating at 5°C/min to 1400°C for 2 h. The Archimedes method was used to measure the "fired" density.

#### (4) Stress Relaxation Experiments

Stress relaxation measurements were performed using a servo-hydraulic mechanical test machine previously described by Velamakanni *et al.*<sup>8</sup> The cylindrical specimens, contained within the plastic bag, were deformed in compression under the displacement control mode of machine operation. Either a 4450 N (1000 lb) or an 890 N (200 lb) load cell was used depending on the peak stress of the sample being tested. Initial testing was done using the 4450 N load cell and samples that exhibited only low loads were reproduced and tested with the 890 N load cell to take advantage of its better resolution at low loads. A small compressive load of 0.5 to 2.0 N was applied to ensure that the specimen was in good contact with the loading platens. Although no aging effects of the saturated bodies were observed in the previous study,<sup>8</sup> any effects of aging were minimized by testing the specimens within a period of 30 to 90 min after they were produced.

Each stress relaxation experiment consisted of applying a 2% compressive strain on the sample at a predetermined loading rate and then fixing the crosshead while the stress within the specimen relaxed. The load was measured and recorded during the loading as well as during the relaxation period. The test was terminated when the load either relaxed to zero or relaxed to a constant value. A constant displacement rate of 25 mm/min was used, corresponding to an initial strain rate of  $0.030/s \pm 0.005$ . (Slightly different specimen dimensions produced the strain rate variation.) Similar results were found for specimens tested at 5 mm/min. Stress was calculated by assuming no change in area of the specimen during the test.

### III. Results and Discussion

#### (1) Demolding after VibraForming

Figure 2 maps the time-temperature conditions that produced bodies that were either "brittle" or "plastic." Bodies denoted "brittle" did not deform significantly before cracking. Those denoted "plastic" showed significant plastic deformation before cracking. The "brittle" bodies were rigid enough to be removed from the die cavity and handled without deformation. When the die cavity was quenched from 95°C to room temperature in a cool water bath, the bodies were found to be cracked when the mold was opened; cooling in air avoided this problem. The "plastic" bodies tended to adhere to the mold walls and deform during demolding. This led to distortion (and eventually fracture) of thin "vane" sections. The "plastic" bodies did not crack even when quenched from 95°C. Figure 1(b) shows a VibraFormed component made with the condition within the "brittle" region of Fig. 2. Although silicone grease was used as a mold release, it was only partly successful. Many attempts at molding pseudorotors were unsuccessful because of the vane sections sticking to the mold and cracking off during demolding.

#### (2) Relative Density

The relative density results are summarized in Table I. Bodies consolidated from coagulated slurries either with or without

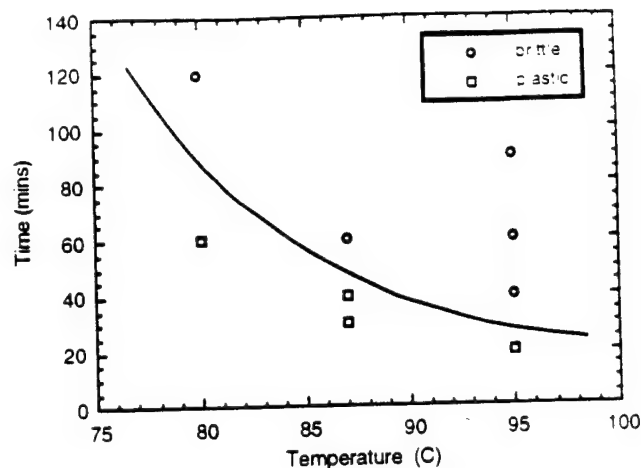


Fig. 2. Body rheology map that shows the heat treatments that produced either "brittle" or "plastic" bodies. The hand-drawn line separates the region that produces "brittle" bodies from the region that produces "plastic" bodies.

urea pack to a much higher relative density ( $\approx 0.58$ ) relative to bodies consolidated from flocculated slurries ( $\approx 0.51$ ). The *in situ* flocculation phenomenon, produced by a heat treatment, does not change the relative density. It was also shown that the stress relaxation experiments did not have a significant effect on the packing densities of the coagulated or flocculated specimens.

#### (3) Stress Relaxation

Typical stress relaxation (stress vs time) plots are shown in Figs. 3(a-d). The two distinguishing features of these plots are the peak stress ( $\sigma_0$ ) and the saturation stress ( $\sigma_s$ ), which is the yield stress of the body when the strain rate is zero. This saturation stress is the parameter which controls the fracture/deformation behavior of the body during demolding. When  $\sigma_s$  is larger than the strength of the saturated powder compact, the body fractures before it can be plastically deformed; viz., the body is brittle. When  $\sigma_s$  is less than the fracture strength, the body is plastic. When  $\sigma_s$  is too low, the body will not retain its shape after molding or deforms during demolding.

The stress relaxation data are summarized in Table II for the different conditions examined; an average of four different specimens are reported for each condition. Other interesting aspects of these tests including elastic modulus and relaxation rate-stress relationships are the subject of ongoing research.

As shown in Table II, specimens containing urea that were not flocculated via heating are quite similar to the coagulated samples (i.e., pH 4, 0.5M  $\text{NH}_4\text{Cl}$ ) without urea. In other words, they are essentially plastic (i.e., low  $\sigma_0$  and  $\sigma_s/\sigma_0 \rightarrow 0$ ). The samples with urea that were heat-treated exhibit the brittle behavior that is indicative of flocculated samples (i.e., high  $\sigma_0$  and  $\sigma_s/\sigma_0 > 0$ ). The *in situ* flocculated specimens have a somewhat lower peak stress and lower saturation stress compared to samples made from a flocculated slurry. This might suggest that the heated specimens may not have been completely flocculated. It is expected that the higher relative density of the *in situ* flocculated specimens would produce a much stronger network relative to the lower density bodies consolidated from the flocculated slurry.<sup>11</sup> At the moment, we can only assume that the flocculation is not complete during the heat treatment. This in no way detracts from the usefulness of this technique in producing complex-shaped components. In fact, a little ductility may be beneficial in preventing cracking during demolding.

#### (4) Fired Densities

The specimens heated to 1400°C for 2 h achieved a relative density  $> 97\%$ . For specimens containing urea that were not heat-treated, the average relative density of four specimens was

Table I. Relative Packing Densities

Slurry preparation	Packing densities
Coagulated, pH 4.0, 0.5M NH <sub>4</sub> Cl	
Before stress relaxation	0.578 ± 0.007 (8)
After stress relaxation	0.576 ± 0.007 (8)
Coagulated with urea, pH 4.0, 0.5M NH <sub>4</sub> Cl, no heat treatment	
Before stress relaxation	0.593 ± 0.010 (3)
After stress relaxation	0.585 ± 0.013 (4)
Coagulated with urea, pH 4.0, 0.5M NH <sub>4</sub> Cl, <i>in situ</i> flocculated	
Before stress relaxation	0.586 ± 0.007 (4)
After stress relaxation	0.589 ± 0.010 (4)
Flocculated, pH 9.0	
Before stress relaxation	0.511 ± 0.002 (3)
After stress relaxation	0.514 ± 0.002 (8)

Numbers in parentheses show the number of specimens measured.

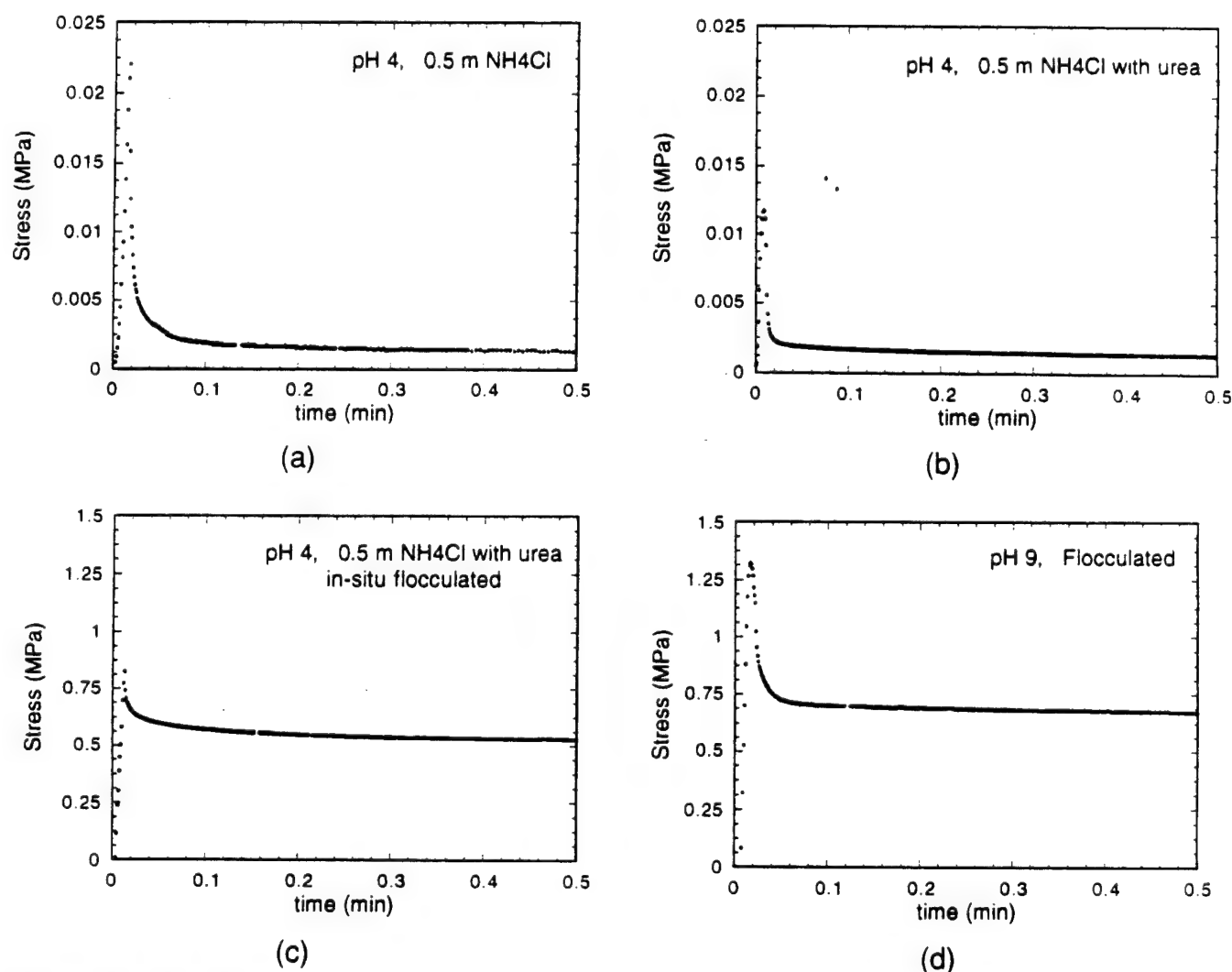


Fig. 3. Typical stress relaxation curves for bodies consolidated from slurries as follows: (a) coagulated (pH 4.0, 0.5M NH<sub>4</sub>Cl); (b) coagulated (pH 4.0, 0.5M NH<sub>4</sub>Cl) with urea, not heat-treated; (c) coagulated (pH 4.0, 0.5M NH<sub>4</sub>Cl) with urea, after 95°C heat treatment; (d) flocculated (pH 9.0).

Table II. Stress Relaxation Behavior

Slurry preparation	$\sigma_0$ (MPa) <sup>a</sup>	$\sigma_s$ (MPa) <sup>b</sup>	$\sigma_0/\sigma_s$
Coagulated, pH 4.0, 0.5M NH <sub>4</sub> Cl	0.035 <sup>3</sup>	0.002 <sup>4</sup>	0.057 <sup>2</sup>
Coagulated with urea, pH 4.0, 0.5M NH <sub>4</sub> Cl, no heat treatment	0.074 <sup>1</sup>	0.002 <sup>1</sup>	0.027 <sup>2</sup>
Coagulated with urea, pH 4.0, 0.5M NH <sub>4</sub> Cl, heated, <i>in situ</i> flocculated	0.79 <sup>1</sup>	0.37 <sup>1</sup>	0.468 <sup>2</sup>
Flocculated, pH 9.0	1.36 <sup>3</sup>	0.88 <sup>3</sup>	0.647 <sup>2</sup>

<sup>a</sup>Peak stress. <sup>b</sup>Saturation stress. <sup>1</sup>Average of four samples. <sup>2</sup>Average of two samples.

$3.88 \pm 0.02 \text{ g/cm}^3$ . The average density of the four specimens that were *in situ* flocculated after VibraForming was  $3.87 \pm 0.02 \text{ g/cm}^3$ .

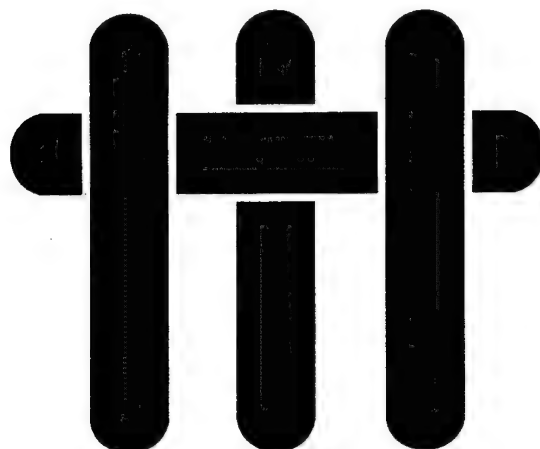
#### IV. Conclusions

A colloidal processing technique that allows dispersed slurries to be first filtered to remove flaw-generating heterogeneities, but takes advantage of short-range repulsion potentials, has been shown to be a promising technology for forming complex-shaped ceramic bodies by VibraForming. The plastic character of the coagulated system, produced by the short-range repulsive potential, was exploited to reshape bodies into more complex objects by simple vibration. An *in situ* flocculation technique via the change in pH due to the decomposition of urea was used to increase the yield stress to facilitate demolding after VibraForming. Stress relaxation experiments confirm that the *in situ* flocculation phenomenon was successful in changing the body rheology from a plastic to a pseudo-elastic behavior.

#### References

- <sup>1</sup>F. F. Lange, "Powder Processing Science and Technology for Increased Reliability," *J. Am. Ceram. Soc.*, **72** [1] 3–15 (1989).
- <sup>2</sup>V. K. Pujari, D. M. Tracey, M. R. Foley, L. C. Sales, and R. L. Yeckley, ORNL Ceramic Technology Project, Bimonthly Technical Progress Report, Oak Ridge National Laboratory, Oak Ridge, TN, October–November 1992.
- <sup>3</sup>B. V. Velamakanni, J. C. Chang, F. F. Lange, and D. S. Pearson, "New Method for Efficient Colloidal Particle Packing via Modulation of Repulsive Lubricating Hydration Forces," *Langmuir*, **6** 1323–25 (1990).
- <sup>4</sup>J. C. Chang, F. F. Lange, and D. S. Pearson, "Viscosity and Yield Stress of Alumina Slurries Containing Large Concentrations of Electrolyte," *J. Am. Ceram. Soc.*, **77** [1] 19–26 (1994).
- <sup>5</sup>B. V. Velamakanni and F. F. Lange, "Method for Preparation of Dense Ceramic Products," U.S. Pat. No. 5,188,780, February 23, 1993.
- <sup>6</sup>J. C. Chang, F. F. Lange, and D. S. Pearson, "Centrifugal Consolidation of  $\text{Al}_2\text{O}_3$  and  $\text{Al}_2\text{O}_3$ - $\text{ZrO}_2$  Composite Slurries vs Interparticle Potentials: Particle Packing and Mass Segregation," *J. Am. Ceram. Soc.*, **74** [9] 2201–204 (1991).
- <sup>7</sup>J. C. Chang, F. F. Lange, D. S. Pearson, and J. P. Pollinger, "Compaction of  $\text{Al}_2\text{O}_3$  Slurries by Centrifugation: The Effect of Interparticle Potentials," *J. Am. Ceram. Soc.*, **77** [5] 1357–60 (1994).
- <sup>8</sup>B. V. Velamakanni, F. F. Lange, F. W. Zok, and D. S. Pearson, "Influence of Interparticle Forces on the Rheological Behavior of Pressure-Consolidated Alumina Particle Slurries," *J. Am. Ceram. Soc.*, **77** [1] 216–20 (1994).
- <sup>9</sup>T. Kramer and F. F. Lange, "Rheology and Particle Packing of Chem- and Phys-Adsorbed, Alkylated Silicon Nitride Powders," *J. Am. Ceram. Soc.*, **77**, 922–28 (1994).
- <sup>10</sup>L. Bergstrom, C. H. Schilling, and I. A. Aksay, "Consolidation Behavior of Flocculated Alumina Suspensions," *J. Am. Ceram. Soc.*, **75**, 3305–14 (1992).
- <sup>11</sup>J. A. Yanez, T. Shikata, D. S. Pearson, and F. F. Lange, "Shear Modulus and Yield Stress of Attractive Particle Networks vs Depth of Potential Well," unpublished work.
- <sup>12</sup>D. B. Marshall, J. J. Ratto, and F. F. Lange, "Enhanced Fracture Toughness in Layered Microcomposites of Ce- $\text{ZrO}_2$  and  $\text{Al}_2\text{O}_3$ ," *J. Am. Ceram. Soc.*, **74** [12] 2979–87 (1991).
- <sup>13</sup>F. H. Baader, T. J. Graule, L. J. Gauckler, private communication; "Direct Coagulation Casting—A New Shaping Technique, Part I: Process Principles, Part II: Application to Alumina," Proceedings of the 8th CIMTEC—World Ceramics Congress and Forum on New Materials, Florence, Italy, June 29–July 4, 1994.
- <sup>14</sup>B. V. Velamakanni and F. F. Lange, "Effect of Interparticle Potentials and Sedimentation on Particle Packing Density of Bimodal Particle Distributions During Pressure Filtration," *J. Am. Ceram. Soc.*, **74** [1] 166–72 (1991).
- <sup>15</sup>F. F. Lange and K. T. Miller, "Pressure Filtration: Consolidation Kinetics and Mechanics," *Am. Ceram. Soc. Bull.*, **66** [10] 1498–504 (1987).
- <sup>16</sup>J. A. Yanez; private communications, 1994.

# M A T E R I A L S



Technical Report Number 14

## Colloidal Processing of Structurally Reliable $\text{Si}_3\text{N}_4$

F.F. Lange and E.P. Luther

Published in: Tailoring of Mechanical Properties of  $\text{Si}_3\text{N}_4$  Ceramics, edited by M.J. Hoffmann and G. Petzow, Kluwer Academic Publishers, 1994

February 1, 1994 through January 31, 1995

Office of Naval Research

Grant No. N00014-90-J-1441

Fred F. Lange

Principal Investigator

Materials Department  
University of California  
Santa Barbara, CA 93106



## COLLOIDAL PROCESSING OF STRUCTURALLY RELIABLE $\text{Si}_3\text{N}_4$

F. F. LANGE AND E. P. LUTHER

Materials Department  
University of California at Santa Barbara  
Santa Barbara, CA 93106

**ABSTRACT.** The interparticle potentials developed in a ceramic system govern the rheological behavior of both the slurry and the consolidated body. Proper control over these potentials allows for the reduction of strength degrading flaws and new forming methods. Post-consolidation shaping of a saturated ceramic body requires a body rheology which is plastic. A plastic, clay-like rheology not only allows complex shaping without the concern of density gradients but also eliminates the problem of stress induced cracking due to the release of forming pressures. Short-range repulsive potentials that persist during packing result in consolidated bodies which are plastic. Three methods of producing short-range repulsive potentials in silicon nitride systems have been investigated. As demonstrated previously for  $\text{Al}_2\text{O}_3$  systems, the addition of salt to dispersed  $\text{Si}_3\text{N}_4$  slurries is shown to produce a short-range repulsion not predicted by classic DLVO theory. Microencapsulation of  $\text{Si}_3\text{N}_4$  with  $\text{Al}_2\text{O}_3$  has also been performed in order to mimic the behavior of the  $\text{Al}_2\text{O}_3$  powder. Steric stabilization of  $\text{Si}_3\text{N}_4$  by either chem- or phys-adsorbed hydrocarbon chains also results in a short-chain repulsive potential. The existence of the potential is demonstrated by viscosity and packing density measurements which show a difference between systems described above and systems in which only van der Waals attraction operates. Only in the case of chem-adsorbed hydrocarbon chains has the short-range repulsion been seen to persist during packing. As a result, only bodies consolidated from these slurries exhibit plastic behavior.

### 1. Introduction

The failure probability of a ceramic component can be determined with statistical parameters describing the flaw populations within the material (e.g., either two or three Weibull parameters) if the tensile stress distribution within the component and the volume of the component at each stress level are known.[1] Strength-stress history effects (sub-critical crack growth) and proof testing can also be included in this analysis.[1] Although the statistical approach is a critical tool for designing components with brittle materials, it can only be used when the statistical parameters are invariant with manufacturing, i.e., the same statistical parameter must persist from the time they are determined through component manufacture. Physically, the statistical parameters that govern failure probability depend on the probability of finding different flaw populations, each with their different size distribution within the component, which must be assumed to be invariant from component to component. Most flaw populations are introduced during material processing and component fabrication.[2] Different flaw populations exist within the powder used to fabricate the materials; these persist through all stages of processing (different types of agglomerates, organic and inorganic inclusions, large particles, etc.). Others can be introduced when the powder is formed into an engineering shape (e.g., cracking due to strain recovery immediately after pressure consolidation). Other flaw populations can be introduced during densification (e.g., the growth of large grains) and still others can be introduced during component fabrication (e.g., surface flaws via diamond machining). Today, most ceramic manufacturers do not recognize the relation between their processing method and the flaws they introduce during processing. The introduction of large flaws in some standard industrial processing methods is unavoidable,

e.g., the practice of spray drying to produce a flowable, agglomerated powder for dry pressing must be abandoned because each agglomerate can produce a large flaw; also, spray drying can introduce air-born flaws. Clean rooms can not remove flaw populations contained within the as-received powder. Variable manufacturing processes (e.g., new lots of powder, worker cleanliness, variable humidity during dry pressing, etc.) produce variable flaw populations and thus, variable statistical parameters.

Although more than one flaw population is commonly observed at different fracture origins within a set of fractured specimens, one population generally dominates the extreme, lower strength values. A change in processing that 'removes' this dominate population, by truncating its size, not only increases the mean strength but also uncovers another flaw population that becomes dominate. Sequential 'removal' of dominate flaw populations by consecutive processing changes leads to a regular increase in the mean strength. Processing changes of this nature not only increase the mean strength and reliability of a ceramic, but, more importantly, cause the manufacturer to develop a new methodology that ensures processing reproducibility and thus, improved component reliability.

As previously reviewed,[2] processing methods exist to minimize the size of common flaw populations. All methods must initiate with the powder itself. A powder can easily be 'cleansed' of heterogeneities (agglomerates, organic and inorganic inclusions, particles greater than a given size, e.g., 5  $\mu\text{m}$ ) by dispersing it in a liquid and passing the resulting slurry through a filter. Powders for a multi-component system can be treated separately and mixed after 'cleansing'. Filtration of the slurry requires the development of long-range, repulsive interparticle potentials to produce stable, dispersed powder slurries. The extensive literature available on this subject has made it relatively simple to stabilize slurries of nearly any chemistry. Once cleansed, the powder can not be separated from the liquid by drying without introducing many of the same heterogeneities removed by filtration; thus, engineering shapes must be formed from the slurry state by piping the slurry to a consolidation and shaping device. Here resides the problem that challenges the leading edge of both colloid and ceramic science.

Because the volume fraction ( $f$ ) of powder within a slurry that can be filtered is less ( $f < 0.40$ ) than the maximum packing density ( $f_{\text{max}} > 0.55$ ), shape forming from the slurry state requires particle consolidation ( $f \rightarrow f_{\text{max}}$ ). Shape forming can be either concurrent with consolidation, e.g., during either pressure filtration or centrifugation, or subsequent to consolidation, e.g., via plastic deformation by press forming, injection molding, etc. Although a high relative density is desired, modest densities ( $f$  somewhat less than  $f_{\text{max}}$ ) are certainly acceptable provided density gradients are not present. Density gradients cause shrinkage gradients during drying and thermal densification that cause warping and/or cracking. Because pressure gradients exist within die cavities, powders that pack to the same density over a wide range of pressures are desired. In addition, some forming methods can not be used if the powder's relative density is pressure sensitive. For example, centrifugation, which naturally produces large pressure gradients, can only be used to form shapes when the powder exhibits pressure insensitive packing. Thus, in ceramics processing, achieving pressure insensitivity of particle packing is a greater issue, relative to obtaining the maximum relative density.

Particles can be either attractive or repulsive. The van der Waals potential always causes particles with similar dielectric properties to be attractive when they are surrounded by a fluid with different dielectric properties. By itself, the van der Waals potential will produce a strong network of particles in elastic contact that is difficult to rearrange due to contact friction. When only van der Waals potential exists, saturated consolidated bodies with a high packing density are brittle and support crack extension (yield stress  $>$  fracture strength). These bodies often crack due to strain recovery when the forming pressure is



released after consolidation. A long-range repulsive potential can be produced by several methods; and, the net interparticle potential can be repulsive when the magnitude of the long-range repulsive potential is larger than the van der Waals potential. Repulsive particles are described as 'dispersed' within their surrounding fluid. Even when the volume fraction of particles is small, dispersed particles form an interactive network because their movement is hindered by neighbors, e.g., dispersed slurries containing high volume fractions of particles can not be passed through a filter. Surface chemistries can also be modified to produce a repulsive potential that is only 'felt' when the particles are close enough to be attracted by the van der Waals potential. These short-range repulsive potentials prevent the attractive particles from touching. As reviewed below, short-range repulsive potentials can produce a weakly attractive network relative to the touching network produced by the van der Waals potential alone. Provided they persist as particles are pushed together during packing, both long- and short-range repulsive potentials can ease particle rearrangement and yield pressure insensitive packing which allows particles to consolidate to their maximum relative density.

Consolidated bodies with weakly attractive particle networks are desired in ceramic processing because they can be used to form complex shapes by methods that involve plastic deformation. Saturated, consolidated clay exemplifies this behavior because its yield stress is large enough to allow shape retention, but low enough to allow plastic forming, i.e., its yield stress < fracture strength. Strongly attractive networks form when only the van der Waals potential acts between particles; these networks can be brittle (yield stress > strength). A weakly attractive network forms when a short-range repulsive potential keeps particles from touching overwhelming the van der Waals potential at small separations, viz., the particles 'sit' apart, in a potential well. As detailed elsewhere, [3-5] the strength of attractive networks in the slurry state can be described by the relative magnitude of their elastic modulus, yield stress and/or viscosity at a given strain rate. High relative packing densities can be obtained by consolidating slurries with weakly attractive networks by either pressure filtration or centrifugation without the problems of particle segregation [6] or pressure sensitivity, [7] whereas the packing density of strongly attractive networks is lower and very pressure sensitive. [5]

As demonstrated in the laboratory [2] and in at least one industrial pilot plant, [8] heterogeneities can be removed by the colloidal process to dramatically increase the mean strength of important structural ceramics. The most impressive demonstration was recently disclosed by Norton-St.-Gobain Industrial Ceramics, [8] where the 'Closed Loop' process for a silicon nitride ceramic was developed. Their 'Closed Loop' process not only involves slurry filtration to eliminate heterogeneities greater than 5  $\mu\text{m}$ , but also the characterization of the consolidated body by sophisticated non-destructive evaluation tools that could detect small density gradients prior to densification. Although their consolidation and shaping method is currently not commercially viable, they have fabricated, at different times and with different powder batches more than 300 tensile specimens via a colloidal method to achieve a mean strength slightly greater than 1000 MPa. More important, they show that the statistical distribution of the more than 300 tensile strengths exhibit a threshold strength of  $\approx 650$  MPa. Threshold strengths are generally only achieved when the strength distribution is truncated by proof testing. In this case, the filtration process, which eliminated flaws within the powder greater than 5  $\mu\text{m}$ , was the effective 'proof test' responsible for the observed threshold strength.

The commercial viability of the "Closed Loop" process will depend on the development of a method in which the particles in a filtered, dispersed slurry can be changed into a weakly attractive network prior to shape forming from the slurry state. This development requires changing the long-range repulsive potential to a short-range repulsive potential that persists during particle packing to impart pressure insensitive particle packing, a high

particle packing and a yield stress low enough to allow plastic behavior (yield stress < fracture strength), but high enough to achieve shape retention after forming (yield stress > maximum shear stress within the formed body). One key ingredient of this development is the understanding of how short-range repulsive potentials, and thus, weakly attractive particle networks, can be achieved for important ceramic powders. The objective of this review is to describe how short-range repulsive potentials can be developed and some approaches that have been taken for  $\text{Si}_3\text{N}_4$  powders.

## 2. Interparticle Potentials

The reader is referred to Horn's [9] review of most phenomena, along with their functional forms, that contribute to the interactive potential between particles in liquid media appropriate to ceramics. Here, only the van der Waals attractive potential and several methods of achieving repulsive potentials will be briefly outlined to set the stage for understanding how short-range repulsive potentials might be developed.

The van der Waals interparticle potential always describes an attractive force between like particles in a fluid with different dielectric properties. It arises from the correlated, attractive interaction of oscillating, electric dipoles associated with atoms and molecules. In the absence of any repulsive potential, the van der Waals potential produces very strong, attractive forces at small interparticle separations (usually < 5 nm for particles  $\approx 1 \mu\text{m}$  in diameter). The magnitude of the van der Waals potential depends on the Hamaker constant, which depends on the high frequency dielectric properties of the particles and their surrounding fluid. For a given system, van der Waals potential also increases with particle size.

When the volume fraction of particles is very small, initially separated particles moving about via Brownian motion, will form small, low density clusters with fractal dimensions. As the clusters become larger, they sediment and pile on one another to form a continuous, touching network. For particle-liquid systems (slurries) containing volume fractions of practical interest for ceramic processors (> 0.1), a connective network of touching particles quickly forms when a vigorously stirred slurry becomes quiescent. Since the particles are in elastic contact, the network is 'strong' i.e., it requires the greatest effort to break apart. It is called a flocced network, schematically illustrated in Fig. 1a. To avoid this strong network, one must produce a repulsive interparticle potential sufficient to counter the attractive van der Waals potential.

A net repulsive potential is produced when a long-range repulsive potential is added to the van der Waals potential. As shown in Fig. 1b & c, the dispersed particles form a non-touching, but interactive network. One method to generate a long-range, repulsive potential is to produce surfaces with a net charge density which is neutralized with ions of opposite charge that hover in solution near the surface. This potential is called an electrical double-layer. Charged oxide surfaces can be produced in water when the -M-OH surface sites react with either  $\text{H}_3\text{O}^+$  or  $\text{OH}^-$  ions. By controlling the pH, the net surface charge can be either positive (acidic conditions), neutral, or negative (basic conditions). The pH that produces a neutral surface is called the iso-electric point (iep). The pH required to maximize the surface charge density (either positive or negative) depends on the surface chemistry and its equilibrium with  $\text{H}_3\text{O}^+$  and  $\text{OH}^-$ . The surface is neutral at an intermediate pH (iep), where the surface contains a large fraction of neutral -M-OH sites and equal proportions of hydrated, positive sites (-M- $\text{H}_2\text{O}^+$ ) and negative (-M- $\text{O}^-$ ) sites. Ions in the solution (e.g., those used to change the pH, those produced by the slight solubility of the particles, and those purposely added as a salt) with an opposite charge relative to the surface, known as counterions, attempt to neutralize the surface by forming a diffuse 'cloud' layer around each particle. The 'cloud' layer contains both positive and

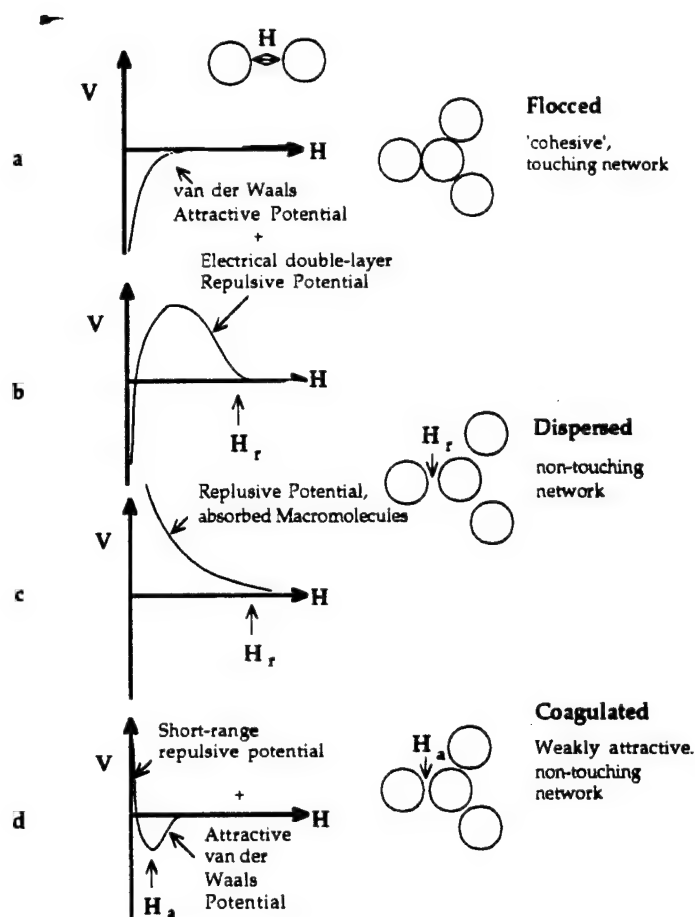


Figure 1 Schematic of different interparticle potentials and their particle networks.

negative ions, but with a concentration gradient of counterions that decreases from the surface into the liquid. The thickness of this 'cloud' layer, generally called the Debye length, decreases with increasing concentration of counterions in solution. The charged surface and its diffuse cloud of oppositely charged counterions is the electrical double layer. Although an easy way to understand this repulsive potential is to simply state that the charged particles repel one another, the repulsive potential is really due to an osmotic pressure caused by the increase in ion concentration within the diffuse layer when the particles are brought closer together. The Debye length is large when few counterions are present and decreases with increasing counterion concentration. The largest electrostatic potential is achieved for a high surface charge density (or surface potential) and a large Debye length (few counterions). The magnitude of the repulsive electrostatic potential can be reduced to zero by either adding an excess of salt and/or by changing the pH to the iep to produce a neutral surface.

The DLVO (Derjaguin, Landau, Verwey and Overbeek) theory adds the van der Waals attractive potential and the repulsive electrical double-layer potential together to produce a combined interparticle potential that can be either repulsive or attractive, depending on the magnitude of the repulsive potential. One form of a combined interactive potential (high surface charge and low salt content) is shown in Fig. 1b. For this condition, as particles approach one another, they encounter a repulsive energy barrier. The particles remain

separated if the energy barrier is many times their kinetic energy. When they crowd together at moderate volume fractions, they attempt to 'sit' at positions that minimize their interaction potential, viz., they form a non-touching, but interactive network with a separation distance usually  $> 10$  nm shown schematically in Fig. 1b. Since the particles in the network are not touching one another, the system is called a 'dispersed' slurry. Because the electrical double-layer potential is estimated with an exponential function and the van der Waals potentials with a power law function, the latter 'wins' at very small separations ( $< 0.5$  nm). Thus, the particles will 'fall' into a deep potential well if they are strongly pushed together.

If the repulsive part of the combined, DLVO potential is reduced (e.g., decreasing the surface charge by changing pH), a condition can be achieved where the repulsive barrier is no longer sufficient to prevent particles from slipping into the deep potential well caused by the van der Waals attractive potential; and, a strongly cohesive, touching network is produced as described above. Thus, the DLVO theory teaches that although the combined repulsive interaction (magnitude of the repulsive barrier and equilibrium separation distance) can be controlled and optimized (by controlling pH and salt content), particles should always fall into a deep potential well to form a cohesive, flocced network when conditions are much less than optimum. That is, DLVO theory offers no help in understanding how one might control the depth of the attractive well.

A second method to produce a long-range repulsive potential is to either chem- or phys-adsorb macromolecules on the particle's surface as shown in Fig. 2a. These macromolecules would prefer to be in solution if the particle's surface was not present. The molecules can either be adsorbed to the surface at one end (bi-functional molecules) or adsorbed at different places along its length with loops extending into the liquid. If the molecule is attached with extended loops, the surface of each particle must be fully saturated so that macromolecules from one particle can not link to another to cause flocculation. The repulsive potential due to the molecules becomes finite at approximately twice the molecule (or loop) length, and increases as the molecules (or loops) are pushed together as shown in Fig. 2a. This phenomena is called steric stabilization; it is commonly used to disperse particles in non-polar liquids where the electrical double-layer approach is not useful. If the molecules are weakly attached to the surface (phys-adsorbed), recent evidence [10] suggests that they can be pushed away during particle packing. Thus, strongly attached (chem-adsorbed) molecules are desired.

A short-range repulsive potential can arise when small molecules within the liquid can lower their free energy by either weakly bonding or ordering themselves at the surface. Attempting to remove the adsorbed molecules by forcing two surfaces together requires work, and thus can give rise to a very short-range, highly repulsive potential, commonly called a solvation potential. [9] Since the molecules are very small and/or form a very thin layer of ordered molecules, the particles are attractive due to the reasons discussed above, but sit apart within a potential well. Under certain conditions, the basal surface of mica is known to develop a special solvation potential called the hydration potential. Using the surface force apparatus, Israelachvili, Pashley and co-workers [11,12] showed that when mica is placed in water, the potassium ion in its structural surface site can be strongly hydrated by water molecules to produce a layer of 'structured' water molecules. A sufficient concentration of  $K^+$  ions must exist in solution, to keep the hydrated  $K^+$  ions in the surface from dissolving into the water. In effect, when a sufficient amount of a potassium salt is dissolved in the water, water molecules become bound to the surface through the hydrated potassium ions which, in turn, are bound within their structural surface sites. They also showed that by adding other salts to the water, the hydrated potassium ion can be exchanged with another hydrated cation to change the 'strength' of the hydration potential. When no long-range repulsive potential is present, their surface

force measurements show that the net surface potential has a functional form similar to that shown in Fig. 1d, i.e., attractive at separation distances  $> \approx 2$  nm, and highly repulsive at smaller separations. Because of the structural similarities with mica and a host of other evidence, [13] it is believed that clay surfaces also develop a hydrated surface layer and, thus, a repulsive hydration potential.

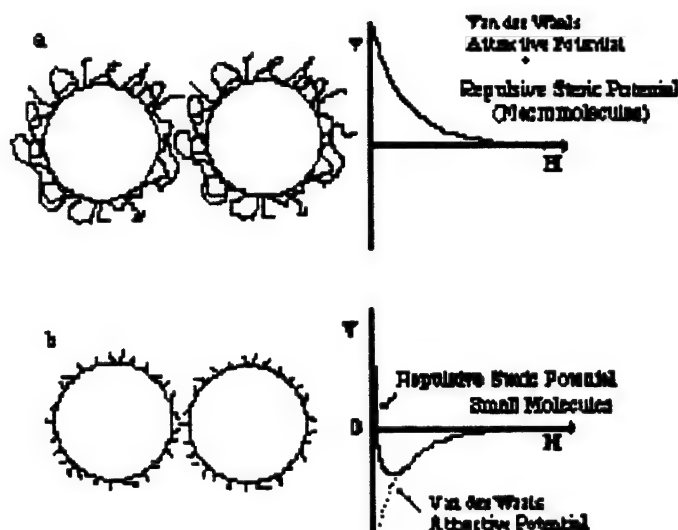


Figure 2 Adsorbed molecules can produce a) long-range repulsive potentials and b) short-range repulsive potentials.

Velamakanni et al.[3] has shown that a short range repulsive potential can also be developed on the surfaces of  $\text{Al}_2\text{O}_3$  particles. This short range, repulsive potential was developed when salt was added to an aqueous  $\text{Al}_2\text{O}_3$  slurry prepared at a pH known to produce a positive surface charge and, thus, a highly dispersed particle network. When sufficient salt was added to the slurry it was noted that the dispersed network was altered to what superficially appeared as a flocced network predicted by DLVO theory. After further experiments, primarily concerned with packing [3,7] and network strength determinations, [4] it was concluded that the salt did change the dispersed network to an attractive network, but this new attractive network was not strongly cohesive. That is, unlike a flocced network produced by changing the pH to the iso-electric point, the particles in this new network could easily be rearranged. Yield stress and viscosity vs. shear rate measurements [4,5] of slurries also showed that the strength of the attractive network could be increased to a maximum value that was still below the strength of the flocced network by adding salt.

All evidence now shows that when the salt is added, the counterions diminish the magnitude of the repulsive, long-range electrostatic potential as predicted by DLVO theory, but they also produce a short-range, repulsive potential not suggested by classical DLVO theory. The short-range repulsive potential due to added salt has been recently confirmed with sapphire plates in the surface force apparatus by Ducker et al. [14] The short-range interparticle potential is currently believed to be due to a hydrated layer of counterions similar to that found for mica surfaces, [11,12] and for clay surfaces.[13] Chang et al.[15] have recently modeled this behavior summing the functions for the electrical double-layer potential ( $V_{LR}$ ), the van der Waals potential ( $V_A$ ) and an exponential function used to describe the short-range potential ( $V_{SR}$ ) for  $\text{Al}_2\text{O}_3$  particles



with a radius of 0.125  $\mu\text{m}$ , a surface potential of 40 mV, and a Hamaker constant of  $4.9 \times 10^{-20}$  J:

$$V = V_{\text{LR}} + V_{\text{A}} + V_{\text{SR}}. \quad (1)$$

The short-range potential was described by

$$V_{\text{SR}} = C \exp\left(-\frac{H}{B}\right), \quad (2)$$

where  $H$  is the separation distance between surfaces of the particles, the pre-exponential factor  $C$  represents how strongly the molecules (hydrated counterions) are bonded to the surface, and  $B$  describes the range of the interaction. Based on experimental determinations of the lowest concentration of salt needed to first form an attractive network (known as the critical coagulation concentration = CCC, e.g., for  $\text{NH}_4\text{Cl}$ , CCC = 0.12 molar [15]) and the assumption that the network would be attractive when the potential well was  $< -5$  kT, values of  $C = 30$  kT and  $B = 5$  nm were calculated. Figure 3 illustrates the total potential,  $V$ , for different ionic strengths ( $I$ ), which only effect the magnitude of the electrical double-layer potential ( $V_{\text{LR}}$ ). As shown in Fig. 3, when  $I < 0.12$  molar, the particles are repulsive, and when  $I \geq 0.12$  molar, the particles are attractive and 'reside' in a potential well that increases in depth from  $\approx -5$  kT ( $I = 0.12$  molar) to  $\approx -30$  kT ( $I = 1.0$  molar); larger salt concentrations do not significantly deepen the potential well. The change in the depth of the well is consistent with the strength of the attractive network for increasing salt concentrations. [15] This modeling, combined with rheological properties shows that the salt additions have two effects. First, the added salt produces a short-range repulsive potential for reasons not clearly understood. Second, as predicted by DLVO theory, the salt decreases the long-range repulsive potential, which in turn, causes the potential well to deepen with salt content to a maximum depth of  $\approx -30$  kT.

Pressure filtration [3] and centrifugation [7] studies show that alumina bodies produced with slurries where particles are attractive, but non-touching exhibit high particle packing. It appears that the short-range repulsive forces can act as a 'lubricant' to aid in the rearrangement process required for particle packing.[3] Due to the attractive nature of the interparticle potentials, bodies can be formed by centrifugation without mass segregation [6] as recently demonstrated by the processing of unique multi-layered transformation toughened composites. [16] In addition, bodies formed from coagulated slurries exhibit plastic-like body rheology [17] and can be reshaped to fill complex die cavities by vibration. [18] In many respects, coagulated slurries and the bodies they form can have rheological characteristics similar to clay systems.

### 3. Silicon Nitride: Development of Short-Range Repulsive Potentials

Three methods [10,19,20] are reviewed to develop short-range repulsive potentials for a commercial silicon nitride powder (Ube, SN-E3). In one method, salt is added to a dispersed slurry as described above for  $\text{Al}_2\text{O}_3$ . For the second, the chemistry of the  $\text{Si}_3\text{N}_4$  surface is changed to resemble  $\text{Al}_2\text{O}_3$  by two different methods, such that the behavior mimics  $\text{Al}_2\text{O}_3$  in the slurry state. In the third method, short hydrocarbon chains are either chem-adsorbed (attached by a chemical reaction) or phys-adsorbed on the surface. Of all of these methods, only the short-range repulsive potential produced by the chem-adsorbed, hydrocarbon chains persists during particle packing.

The surface chemistry of different  $\text{Si}_3\text{N}_4$  powders was determined by Bergstrom et al [21] to consist of  $-\text{Si}-\text{OH}$  and  $-\text{Si}_2-\text{NH}$  surface groups. The ratio of these two groups was dependent on the powder, which was presumed to depend on how the powder was synthesized and treated after synthesis. The iso-electric point (iep: pH were the most sites

are uncharged and the number density of positive and negative sites are equal) can range between pH  $\approx$  2, the case for SiO<sub>2</sub>, to pH  $>$  8, the case where the 'surface SiO<sub>2</sub>' is dissolved in basic solutions. Contrary to common belief, the iep of many Si<sub>3</sub>N<sub>4</sub> powders lies between pH 4 and 6, suggesting that the surface chemistry ranges between Si<sub>2</sub>N<sub>2</sub>O and SiO<sub>2</sub>; the Ube SN-E3 powder used here had an iep at pH = 5.5 and a mean particle diameter of  $\approx$  0.7  $\mu$ m.

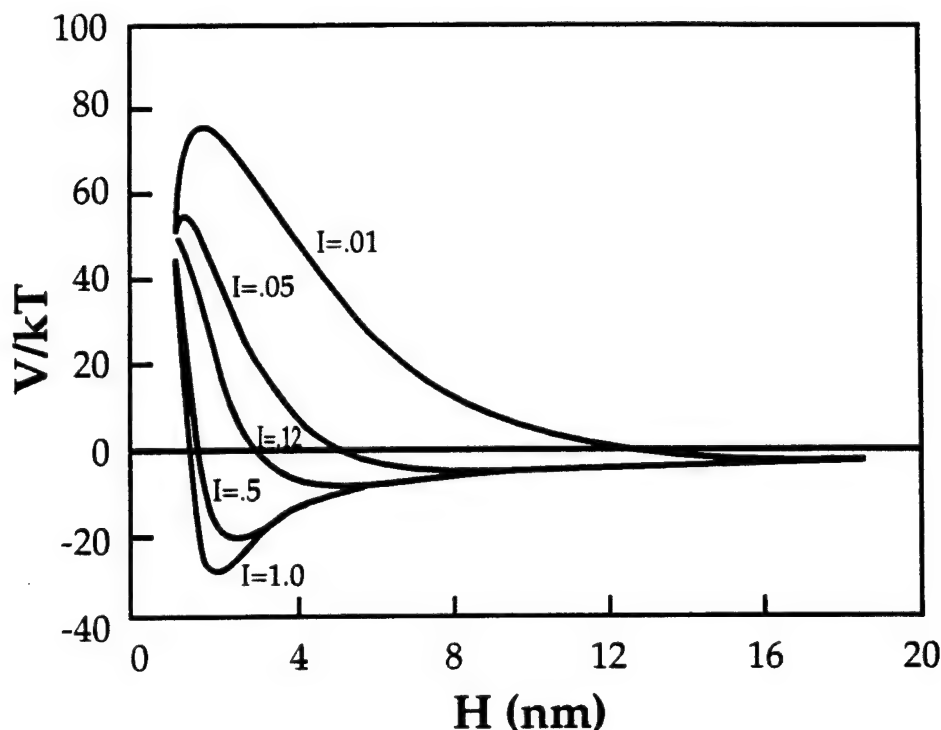


Figure 3 Sum of van der Waals ( $HC = 4.9 \times 10^{-20}$  J, 0.25  $\mu$ m dia. particles), electrical double-layer ( $V_z = 40$  mV), and exponential, short-range repulsive potentials for different ionic ( $I$ , molar, NH<sub>4</sub>Cl) strengths. [15]

As recently reported by Luther et al., [19] the properties of aqueous, dispersed, silicon nitride slurries can be changed with additions of NH<sub>4</sub>Cl. Because the iep of the Si<sub>3</sub>N<sub>4</sub> used was pH = 5.5, dispersed slurries could be produced at low pH and high pH, where the surface is positive and negative, respectively. At pH 10 the effect of adding NH<sub>4</sub>Cl is similar to that suggested by DLVO theory, namely, for concentrations  $\geq$  0.5 M, the viscosity vs. shear rate behavior, yield stress, elastic modulus and the relative packing density is identical to slurries prepared at the iso-electric point. On the other hand, the effect of salt on dispersed slurries prepared at pH 2 differ from the behavior implied by classical DLVO theory, i.e., measurement of the same properties showed that the attractive interparticle potential was much weaker relative to that produced at the iso-electric point. For example, when 0.7 moles of NH<sub>4</sub>Cl was added, the elastic modulus of a pH 2 slurry containing 0.30 volume fraction of the powder was more than an order of magnitude lower than that of the same slurry either at the iep or dispersed at pH 10 with the same salt content. Similar to alumina slurries, these results suggest that a short-range, repulsive interparticle potential is developed in salt added slurries prepared at pH 2 which prevents the attractive particles from touching. The same short-range potential apparently is not

developed with salt additions at pH 10. Thus, a coagulated aqueous slurry (weakly attractive particle network) could be developed for both Ube SN-E3  $\text{Si}_3\text{N}_4$  and  $\text{Al}_2\text{O}_3$  powder when salt was added to dispersed slurries at low pH.

Although the coagulated silicon nitride and alumina slurries were similar at low pH, two differences were observed after particle packing. First, as shown in Fig. 4, the relative density of saturated bodies produced from coagulated  $\text{Si}_3\text{N}_4$  slurries (pH 2, 0.5 M  $\text{NH}_4\text{Cl}$ ) were intermediate between those produced from either dispersed (pH 2) or flocced (pH 7) bodies. In contrast, the packing density for a coagulated  $\text{Al}_2\text{O}_3$  slurry is only slightly lower than a dispersed slurries. Second, bodies consolidated from any silicon nitride slurry (dispersed, coagulated or flocced) are brittle (i.e., fracture before they flow) unlike the plastic bodies produced from coagulated, alumina slurries. Both results show that although either long- or short-range repulsive potentials can be developed in the slurry state, both are removed when the  $\text{Si}_3\text{N}_4$  particles are pushed together during packing.

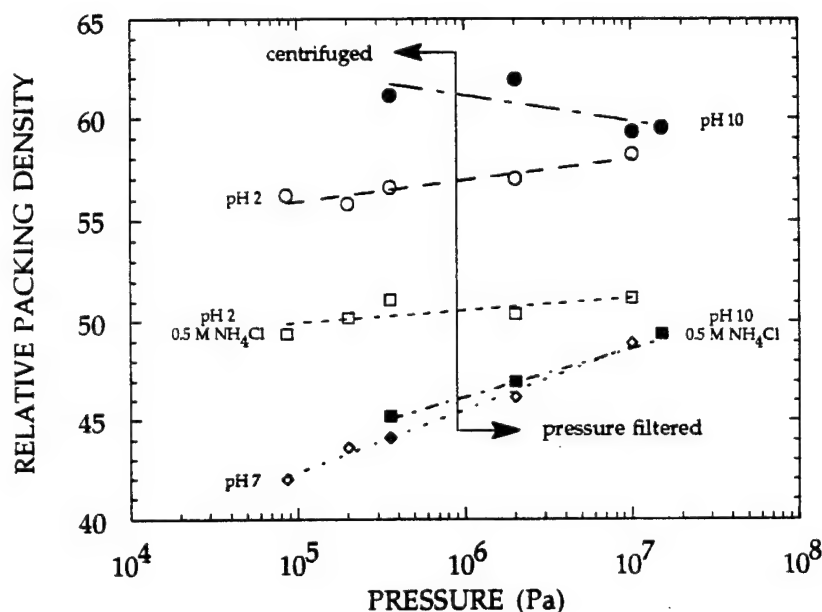


Figure 4 Relative density of saturated  $\text{Si}_3\text{N}_4$  bodies consolidated by either centrifugation or pressure filtration from the different slurries shown. [19]

In a second approach to produce short-range repulsive potentials in aqueous  $\text{Si}_3\text{N}_4$  slurries, Luther et al. [20] used two methods to coat the surface of the  $\text{Si}_3\text{N}_4$  particles to make them behave as  $\text{Al}_2\text{O}_3$  particles. In one method, used by Garg and De Jonghe [22] to micro-encapsulate silicon nitride with either yttria and yttria-alumina sintering aids, a slurry containing silicon nitride particles,  $\text{Al}(\text{NO}_3)_3$  and urea was heated to force the precipitation of aluminum hydroxide. As the solution is heated, the urea decomposes and the slurry becomes basic. Under appropriate conditions, precipitation nucleates on the particle surface. In the second method, modified from that reported by Liden et al., [23] a small quantity of aluminum sec-butoxide was introduced at room temperature to a slurry



of previously dried silicon nitride powder and anhydrous hexane held under dry nitrogen. After the initial alkoxide- $\text{Si}_3\text{N}_4$  surface reaction was complete <sup>a</sup>, the slurry was subjected to nitrogen gas bubbled through water to hydrolyze the alkoxide molecules attached to the  $\text{Si}_3\text{N}_4$  surface. After hydrolysis was complete <sup>a</sup>, Al-alkoxide was introduced again under dry nitrogen to first react with the surface and then later with water from saturated nitrogen. This cyclic reaction was continued until the washed and dried powder behaved like  $\text{Al}_2\text{O}_3$  when dispersed in water.

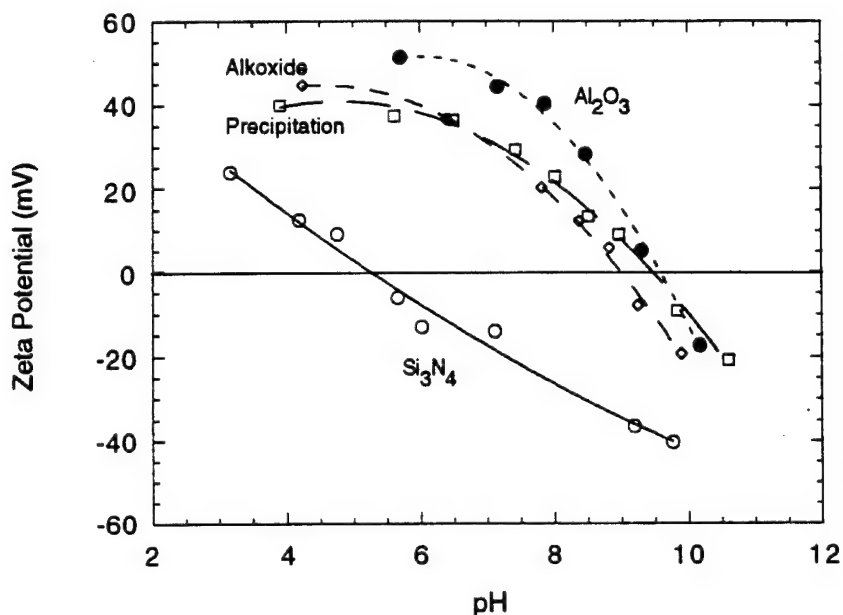


Figure 5 Zeta potential vs pH for as-received  $\text{Si}_3\text{N}_4$ ,  $\text{Si}_3\text{N}_4$  coated with ' $\text{Al}_2\text{O}_3$ ' by two different methods, and a  $\text{Al}_2\text{O}_3$  powder. [20]

After the appropriate reaction conditions,[20] Fig. 5 shows that aqueous slurries of both ' $\text{Al}_2\text{O}_3$ ' coated  $\text{Si}_3\text{N}_4$  powders exhibited an electrokinetic behavior nearly identical to  $\text{Al}_2\text{O}_3$  powder. That is, the iep was increased from  $\text{pH} \approx 5.5$ , for unreacted  $\text{Si}_3\text{N}_4$  powder, to  $\text{pH} \approx 9$  for the coated powder. Transmission electron microscopy confirmed the existence of these thin ( $\approx 5$  nm) coatings. Figure 6 illustrates the viscosity vs. shear rate data for the alkoxide coated  $\text{Si}_3\text{N}_4$  powder (0.20 volume fraction) showing Newtonian behavior of the slurry dispersed at pH 4 (without added salt), shear thinning

<sup>a</sup> The apparent reaction of the Al-alkoxide molecules with the -Si-OH surface sites was observed to dramatically lowered the viscosity of the slurry, yet, the particles within the slurry were still attractive, i.e., they agglomerated when stirring was stopped. This observation strongly suggests that the chem-adsorbed, but not fully hydrolyzed Al-alkoxide molecules produced a short-range repulsive potential. When water was added, via saturated flowing nitrogen, to hydrolyze the chem-adsorbed alkoxide molecules, the viscosity dramatically increased.

behavior of dispersed slurries (pH 4) when  $\text{NH}_4\text{Cl}$  was added at concentrations  $> 0.1$  molar, increased viscosity with increasing salt concentration to a maximum value at  $\approx 1$  to 2 molar, and the much larger viscosity of the slurry flocced at the iep (pH 9). Elastic modulus measurements on slurries containing attractive networks (pH 9 and salted slurries at pH 4), showed that these values for the salt added slurries were more than an order of magnitude lower relative to the flocced slurry. These rheological measurements exhibited nearly identical behavior to that previously reported for  $\text{Al}_2\text{O}_3$ , [3,4] and show that a short-range repulsive potential exists for the case where salt is added to the dispersed (pH 4) slurries.

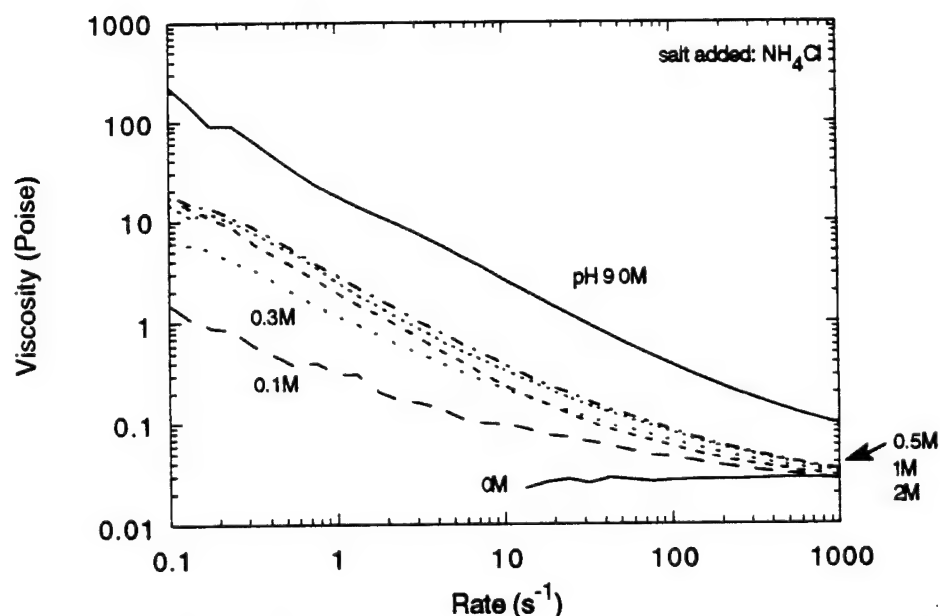


Figure 6 Viscosity vs shear rate for aqueous slurries of  $\text{Si}_3\text{N}_4$  powder (0.20 volume fraction) coated 'Al $_2\text{O}_3$ ', dispersed (pH 4), coagulated (pH 4 with added salt), and flocced (pH 9). [20]

Despite the apparent development of a short-range repulsive potential for 'Al $_2\text{O}_3$ ' coated  $\text{Si}_3\text{N}_4$  powder, the upper portion of Table 1 shows that when the coagulated (dispersed, salt added) slurries were consolidated via pressure filtration (at 2 MPa) the relative density was identical to that achieved for both un-coated (as-received) and coated powder at their iso-electric points (flocced slurries), pH 5.5 and pH 9, respectively. In addition, bodies consolidated with either coagulated or flocced slurries were brittle, i.e., they cracked when subjected to forming pressures. Thus, it was concluded that the apparent short-range repulsive potential that was developed for the 'Al $_2\text{O}_3$ ' coated powder did not persist during particle consolidation.

The third method [10] of producing a short-range repulsive potential is simply to attach short molecules to the surface as schematically shown in Fig. 2b. When the molecule is  $< 5\text{nm}$  (depending on the magnitude of the van der Waals potential via the Hamaker constant), the repulsive steric potential only begins when the particles are already attractive due to the van der Waals potential. Although the long- and short-range repulsive steric potential can be estimated with a complex function, [24] it is convenient to estimate the

interaction length by truncating the van der Waals potential at twice the length of the adsorbed molecule\* (each surface has adsorbed molecules) when it is known that the molecule is attached at one end. Thus, adsorbed molecules that are short enough to allow particles to be attractive due to their van der Waals potential, but sufficiently long enough to keep particles from touching and thus falling into a deep potential well, are expected to produce a weakly attractive particle network. Kramer and Lange [10] chose to demonstrate this concept for the same  $\text{Si}_3\text{N}_4$  powder used above by using the reaction of different alcohols with -M-OH surface groups, a method patented by Iler [25] for grafting carbon chains to the surface of silica particles for lubrication applications.

**Table 1 Packing Density of Ube E-3 Silicon Nitride**

<u>Surface Modification</u>	<u>Condition</u>	<u>Relative Density</u>
<b>As-received <math>\text{Si}_3\text{N}_4</math> Powder</b>		
	Dispersed (pH 2, no salt added)	0.57
	Dispersed (pH 10, no salt added)	0.61
	Flocculated (pH 6, no salt added)	0.47
	Salt Added (pH 2, 0.5 M $\text{NH}_4\text{Cl}$ )	0.50
	Salt Added (pH 10, 0.5 M $\text{NH}_4\text{Cl}$ )	0.47
<b><math>\text{Si}_3\text{N}_4</math> Powder Coated with '<math>\text{Al}_2\text{O}_3</math>', Precipitation Method</b>		
	Dispersed (pH 4, no salt added)	0.58
	Flocculated (pH 9, 0 M $\text{NH}_4\text{Cl}$ )	0.48
	Salt Added (pH 4, 0.5 M $\text{NH}_4\text{Cl}$ )	0.51
<b><math>\text{Si}_3\text{N}_4</math> Powder Coated with '<math>\text{Al}_2\text{O}_3</math>', Alkoxide Method</b>		
	Dispersed (pH 4, no salt added)	0.59
	Flocculated (pH 9, no salt added)	0.48
	Salt Added (pH 4, 0.5 M $\text{NH}_4\text{Cl}$ )	0.52
<b><math>\text{Si}_3\text{N}_4</math> Powder Reacted with Different Alcohols (Chem-Adsorbed)</b>		
Octadecanol	(MW = 270.5 gm/m, length = 2.3 nm)	0.60
Dodecanol	(MW = 186.3 gm/m, length = 1.5 nm)	0.59
Octanol	(MW = 130.2 gm/m, length = 1.0 nm)	0.51
none, in dodecane		0.48

Three alcohols (octanol, dodecanol, and octadecanol) with extended carbon chain lengths between  $\approx 1$  and 2 nm were chem-adsorbed on the  $\text{Si}_3\text{N}_4$  powder by reacting with hydroxyl surface groups with the alcohol at temperatures  $\leq 200^\circ\text{C}$  ( $-\text{Si}-\text{OH} + \text{ROH} \rightleftharpoons -\text{Si}-\text{OR} + \text{H}_2\text{O}$ ). After washing and drying, a slurry was formed of the reacted powder in dodecane. Slurry rheology, particle packing density and body rheology were determined for dodecane slurries formed with these chem-adsorbed powders. These same properties were determined for slurries where the alcohol was simply added, but not reacted with the powder (phys-adsorbed powders).

The viscosity of chem-adsorbed slurries was shear-thinning with longer chains producing lower viscosities at a given shear rate as shown in Fig. 7. As shown in Table 1, the relative density of the saturated powder compacts produced by pressure filtration (10 MPa) was high ( $\sim 0.60$ ) for octadecanol and dodecanol reacted powders, and lower ( $\sim 0.50$ ) for the octanol reacted powder. When a sufficient amount ( $> 10$  times that required for chem-adsorption) of the same alcohol was simply added to the unreacted  $\text{Si}_3\text{N}_4$  slurry system, the phys-adsorbed slurries exhibited similar rheological behavior as the chem-adsorbed slurries, but unlike chem-adsorbed slurries, their packing density was lower and their slurries were de-stabilized by water vapor. Stress relaxation experiments showed that bodies formed with the octadecanol chem-adsorbed powders were plastic after consolidation, whereas phys-adsorbed bodies were brittle (fractured before flow).

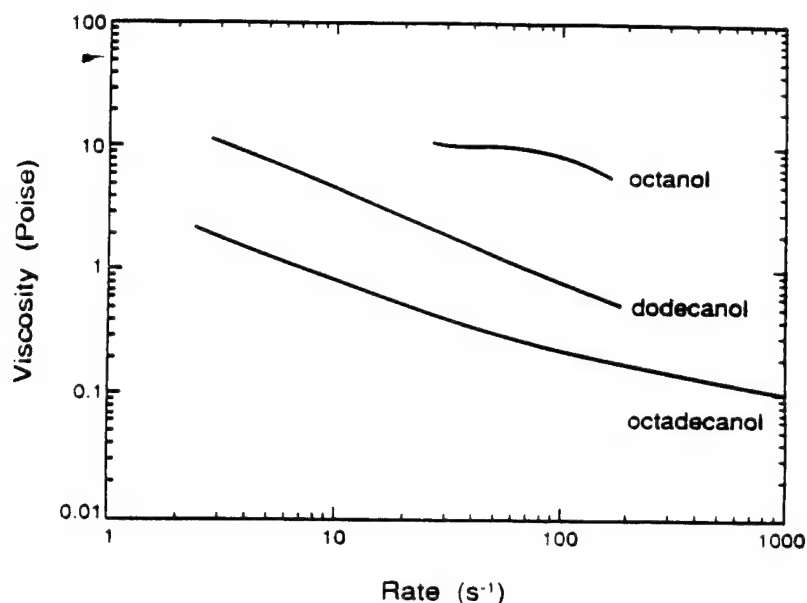


Figure 7 Viscosity vs shear rate for  $\text{Si}_3\text{N}_4$  toluene slurries (0.20 volume fraction) with different chem-adsorbed hydro-carbon chains. [10]

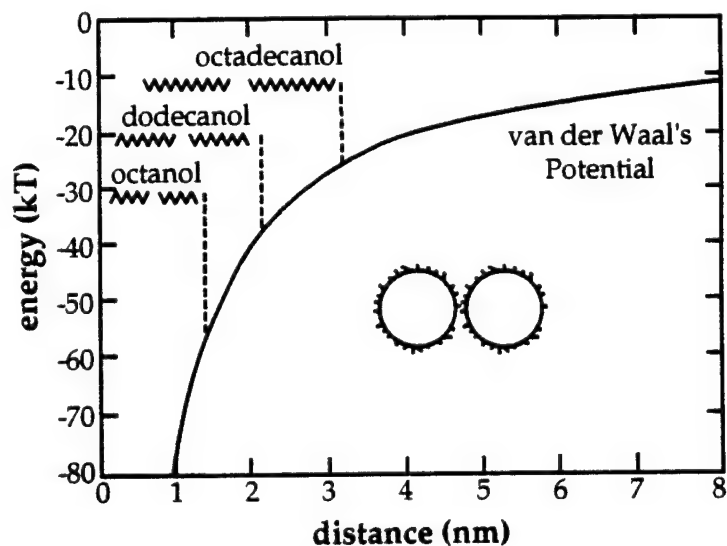


Figure 8 Van der Waals potential for silicon nitride particles ( $0.5 \mu\text{m}$  dia.) truncated with three different chem-adsorbed alcohol molecules. [10]

All evidence suggests that the short chained alkyl groups are steric 'stabilizers' at small interparticle distances, and thus prevent the particles from making surface-surface contact in common organic liquids, i.e., they produce a short-range interparticle, repulsive potential. Figure 8 schematically illustrates the van der Waals potential for  $0.5 \mu\text{m}$

diameter  $\text{Si}_3\text{N}_4$  particles in toluene (Hamaker Constant =  $2 \times 10^{-20}$  J), and illustrates how 3 different chem-adsorbed, carbon chains would truncate this potential to produce 3 different potential wells.[4] Comparing the viscosity vs. shear rate data, it can be seen that the strength of the 3 attractive  $\text{Si}_3\text{N}_4$  powders networks produced with each of the 3 chem-adsorbed molecules is inversely proportional to the depth of the potential well, viz., the deeper the well, the stronger the network. Molecules with extended lengths within the range of approximately 1 nm to 2 nm produce a network that is attractive, but much weaker than that produced by the attractive van der Waals potential alone. Shorter molecules ( $\leq 1$  nm) appear to produce networks that are as strong as networks formed with only the van der Waals potential.

#### 4. Concluding Remarks

In this last method used to develop short-range repulsive potentials for  $\text{Si}_3\text{N}_4$  slurries,[10] it was shown that chem-adsorbed molecules, but not phys-adsorbed molecules, persist during particle packing (and in moist environments). It is reasonable to hypothesize that the chem-adsorbed molecules are strongly attached to the surface and can not be 'pushed' away during particle packing. In contrast, it appears that the phys-adsorbed molecules, which also produce a weakly-attractive network in the slurry state, could be displaced from the surface during particle packing to allow particles to be 'pushed' into their deep potential well governed only by the van der Waals potential. The reason why the short-range repulsive potentials produced with the other two approaches did not persist during particle packing is not as clearly evident. For the method where the particles are coated with ' $\text{Al}_2\text{O}_3$ ', it could be argued that the coating was not sufficiently adherent and did not persist during particle packing.

Although the short-range steric method, where hydrocarbon chains are attached to the surface by a reaction, appears attractive, it is not consistent with the overall goal for improved processing reliability. That is, although the short-range steric method does produce a plastic consolidated body, it does not allow for the long-range repulsive potentials, which are initially needed to remove the heterogeneities by filtration. Thus, the quest continues, where each new approach leads to a greater understanding.

#### Acknowledgment

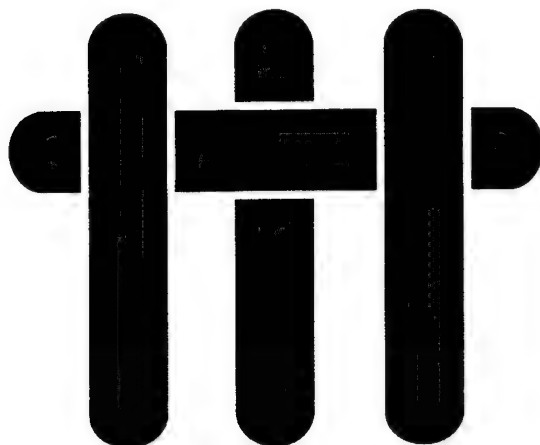
Research sponsored by the U.S. Department of Energy, Assistant Secretary for Conservation and Renewable Energy, Office of Transportation Systems, as part of the Ceramic Technology for Advanced Materials Development Program under Contract DE-AC05-84OR21400 with Martin Marietta Energy Systems, Inc. W.B.S 1.1.4.4.

#### References

1. A. G. Evans and S. M. Wiederhorn, "Crack Propagation and Failure Prediction in  $\text{Si}_3\text{N}_4$  at Elevated Temperatures," *J. Mat. Sci.* 9 270-78 (1974).
2. F. F. Lange, "Powder Processing Science and Technology of Increased Reliability," *J. Am. Ceram. Soc.* 72 [1] 3-15 (1989).
3. B.V. Velamakanni, J.C. Chang, F.F. Lange and D.S. Pearson, "New Method for Efficient Colloidal Particle Packing via Modulation of Repulsive Lubricating Hydration Forces", *Langmuir*, 6, 1323-5 (1990).
4. J.C. Chang, F.F. Lange and D.S. Pearson, "Viscosity and Yield Stress of  $\text{Al}_2\text{O}_3$  Slurries Containing Large Concentrations of Electrolyte", *J. Am. Ceram. Soc.* (in press).
5. J. Yanez, T. Shikata, D.S. Pearson, and F.F. Lange, "Shear Modulus of Attractive, Particle Networks vs. Depth of Potential Well", to be published
6. J.C. Chang, F.F. Lange and D.S. Pearson, "Centrifugal Consolidation of  $\text{Al}_2\text{O}_3$  and  $\text{Al}_2\text{O}_3/\text{ZrO}_2$  Composite Slurries vs. Interparticle Potentials: Particle Packing and Mass Segregation", *J. Am. Ceram. Soc.*, 74, 2201-4 (1991).

7. J.C. Chang, F.F. Lange, D.S. Pearson and J. P. Pollinger, "Pressure Sensitivity for Particle Packing of Aqueous  $\text{Al}_2\text{O}_3$  Slurries vs Interparticle Potential," J. Am. Ceram. Soc. (in press).
8. V.K. Pujari, D.M. Tracey, M.R. Foley, L.C. Sales and R.L. Yeckley, ORNL Ceramic Tech. Project, Bimonthly Tech. Prog. Rept. Oct.-Nov. 1992.
9. R. G. Horn, "Surface Forces and Their Action in Ceramic Materials," J. Am. Ceram. Soc. 73 [5] 1117-1135 (1990).
10. T. Kramer and F. F. Lange, "Rheology and Particle Packing of Chem- and Phys-Adsorbed, Alkylated Silicon Nitride Powders," J. Am. Ceram. Soc. (in press).
11. R.M. Pashley, "DLVO and Hydration Forces between Mica Surfaces in  $\text{Li}^+$ ,  $\text{Na}^+$ ,  $\text{K}^+$  and  $\text{Cs}^+$  Electrolyte Solutions: A Correlation of Double-Layer and Hydration Forces with Surface Cation Exchange Properties", J. Coll. Inter. Sci., 83, 531-46 (1981).
12. J.N. Israelachvili and R.M. Pashley, "DLVO and Hydration Forces Between Mica Surfaces in  $\text{Mg}^{2+}$ ,  $\text{Ca}^{2+}$ ,  $\text{Sr}^{2+}$  and  $\text{Ba}^{2+}$  Chloride Solutions", J. Coll. Inter. Sci., 97, 446-55 (1984).
13. H. van Olphen, *An Introduction to Clay Colloid Chemistry*, John Wiley and Sons, New York, 1977, p 99.
14. W.A. Ducker, Z. Xu, J.N. Israelachvili and D.R. Clarke, "The Forces Between Alumina Surfaces in Salt Solutions: Non-DLVO Forces and Their Effect on Colloid Processing", to be published.
15. J.C. Chang, F.F. Lange and D.S. Pearson, "Functional Form of Interparticle Potentials for Weakly Attractive  $\text{Al}_2\text{O}_3$  Networks Produced at High Concentrations of Electrolyte," to be published
16. D. B. Marshall, J. J. Rato, and F. F. Lange, "Enhanced Fracture Toughness in Layered Microcomposites of Ce- $\text{ZrO}_2$  and  $\text{Al}_2\text{O}_3$ ," J. Am. Ceram. Soc. J Am. Ceram.Soc., 74, 2979 (1991).
17. B.V. Velamakanni, F.F. Lange, F.C. Zok, and D.S. Pearson, "Influence of Interparticle Forces on Rheology of Consolidated Ceramic Particulate Bodies", J. Am. Ceram. Soc. (in press).
18. F. F. Lange and B. V. Velamakanni, "Method for Preparation of Dense Ceramic Products," US Patent 5,188,780, Feb. 23, 1993.
19. E. P. Luther, T. M. Kramer, F. F. Lange and D. S. Pearson, "Development of Short Range Repulsive Potentials in Aqueous Colloidal Processing of Silicon Nitride," J. Am. Ceram. Soc. (in press).
20. Erik P. Luther, Fred F. Lange and Dale S. Pearson, "Surface Modification of Silicon Nitride for Enhanced Colloidal Processing," to be published
21. L. Bergstrom, and E. Bostedt, "Surface Chemistry of Silicon Nitride Powders: Electrokinetic Behavior and ESCA Studies," Colloids and Surfaces, 49, 183-97 (1990).
22. A.K. Garg and L.C. De Jonghe, Microencapsulation of Silicon Nitride Particles with Ytria and Ytria-Alumina Precursors," J. Mater. Res., 5 [1], 136-42 (1990).
23. E. Liden, L. Bergstrom, M. Persson, R. Carlson, "Surface Modification and Dispersion of Silicon Nitride and Silicon Carbide Powders," J. Europ. Ceram. Soc.
24. D. H. Napper, *Polymeric Stabilization of Colloidal Dispersions*, Academic Press, London (1983).
25. R.K. Iler, US Patent 2,657,149 (1953) referenced p.573 in R.K. Iler, *The Chemistry of Silica*, Wiley-Interscience, New York, (1979).

# **M A T E R I A L S**



**Technical Report Number 15**

## **Shear Modulus and Yield Stress Measurements of Attractive Alumina Particle Networks in Aqueous Slurries**

**Joseph A. Yanez, Toshi Shikata, Fred F. Lange, and Dale S. Pearson**

**Sent to: J. Amer. Ceramic Society**

**February 1, 1994 through January 31, 1995**

**Office of Naval Research**

**Grant No. N00014-90-J-1441**

**Fred F. Lange**

**Principal Investigator**

**Materials Department  
University of California  
Santa Barbara, CA 93106**

# Shear Modulus and Yield Stress Measurements of Attractive Alumina Particle Networks in Aqueous Slurries

Joseph A. Yanez, Toshi Shikata, Fred F. Lange, Dale S. Pearson

Department of Chemical Engineering and Materials Department, University of California Santa Barbara, Santa Barbara, CA 93106

## Abstract

The shear modulus and yield stress of attractive alumina particle networks in aqueous slurries was determined as a function of volume fraction (0.1 to 0.5), pH (2, 4, 5, 6, and 9), and salt ( $\text{NH}_4\text{Cl}$ ) concentration using both vane and couette rheological tools.

Consistent with previous observations concerning the relative strength of attractive particle networks, the shear modulus increased to a plateau value with salt concentration. In this work we have shown that the salt concentration at which this plateau value is achieved is a function of the pH, and thus, the surface charge density.

The values of the shear modulus  $[G']$ , yield stress  $[\tau_y]$ , and yield strain  $[\gamma_y]$  of the attractive networks can be described with power law functions for particle volume fraction  $[\phi]$ :  $G' \propto \phi^{4.75}$ ,  $\tau_y \propto \phi^{3.6}$ , and  $\gamma_y \propto \phi^{-1.1}$ , and salt concentration  $[c]$ :  $G' \propto [c]^{2.0}$ ,  $\tau_y \propto [c]^{1.15}$ , and  $\gamma_y \propto [c]^{-0.85}$ .



## 1. Introduction

The use of colloid science in the processing of advance ceramic powders has emphasized the removal of heterogeneities from powders that lead to strength limiting flaws in the final body [1-2] and the development of new shape forming technologies [3-4]. The colloidal processing method includes: 1) the development of a long-range repulsive potential to disperse the powder in a suitable liquid, 2) the removable of heterogeneities by filtering the dispersed slurry, 3) changing the interparticle potentials to produce a weakly attractive particle network, and 4) the consolidation of the particles within the slurry to form an engineering shape. Removing heterogeneities via filtration requires a low viscosity slurry containing a high volume fraction of solids which can only be achieved with long range repulsive potentials. [5-7] Once detrimental heterogeneities are removed, the long-range repulsive potential should be replaced with a short-range repulsive potential in order to develop a weakly attractive particle network. With the weakly attractive network, mass segregation due to sedimentation is avoided in the slurry state [8], particles can be packed to high relative density during consolidation [9-10] and the consolidated body can be plastic. The plastic behavior is desired to avoid damage during strain recovery after consolidation [11] and it allows new shape forming technologies to be used for advanced ceramic powders [3], which are classical for traditional, clay technologies. Thus to fully implement colloidal powder processing, a processor must first disperse a specific powder to remove heterogeneities via filtration, then make it weakly attractive for further processing.

One common method for dispersing ceramic particles is taught by the DLVO theory. [12-14] The surface of a particle containing neutral hydroxide sites can be charged by reacting the neutral sites with either  $H^+$  or  $OH^-$  to produce either positive or negative sites, respectively. DLVO theory teaches that an atmospheric layer of counterions (ions with an opposite charge relative to the dominate surface sites)

surrounds and neutralizes each particle. An osmotic pressure ( i.e., repulsive potential) arises when the layer of counterions around one particle penetrates another to increase the concentration of counterions between them. DLVO teaches that the thickness of the counter ion layer, and thus the separation distance when particles strongly repel one another, is inversely proportional to the concentration of counterions in solution. When the counterion concentration is small, the repulsive potential initiates at a large separation and overwhelms the pervasive, attractive van der waal's potential. Under these conditions the particles strongly repel one another and thus, they are dispersed within the slurry. DLVO teaches that the particles become attractive either at high concentrations of counterions, where the layer of counterions is very thin, or near the iso-electric point where the number density of charged surface sites is small.

Velamakanni et al. [10] discovered that a weakly attractive network is produced when excess counterions are added to a dispersed  $\text{Al}_2\text{O}_3$  slurry, and that these networks are much weaker than the strongly attractive network produced at the pH where the surface is neutral (viz., at the iso-electric point). They postulated that the salt produced a short-range repulsive potential, not predicted by DLVO theory. This short-range repulsive potential was subsequently confirmed with experiments using the Surface Force Apparatus. [15] Thus, Velamakanni et al. [10] discovered a method to change a dispersed,  $\text{Al}_2\text{O}_3$  particle network to a weakly attractive network.

As discussed below, two rheological properties, i.e., the shear modulus and yield stress, can be used to characterize the strength of an attractive network at a given volume fraction of particles. The rheological properties of the weakly attractive network discovered by Velamakanni et al [10] has only been studied for a limited number of conditions [16, 8-11]. One of these studies [16] showed that most of the weakly attractive networks were too viscous to be studied with conventional rheological tools at volume fractions  $> 0.20$ .

Two methods are commonly used to determine the shear modulus and yield stress of attractive particle networks using conventional rheological instruments. [17-25] In one method, the torque is measured as the tool is rotated in one direction at a fixed strain rate; in the second, a sinusoidal oscillation, at a fixed amplitude and frequency, is applied to the tool. With the increasing strain method, an apparent elastic response is observed first (linear stress-strain response), followed by a non-linear 'yielding phenomena' prior to flow (increasing strain at constant stress). With this method, the slope of the initial linear region (shear modulus,  $G'$ ) is independent of the applied shear rate, but the stress where the deviation from linear behavior is observed ('yield stress'), increases with shear rate. With the oscillatory method, a given attractive network will exhibit a fixed value of the shear modulus ( $G'$ ) for conditions where the strain amplitude is small and the frequency is high. [21] A decrease in  $G'$  will occur at a 'yield strain'. Based on these two methods, it is generally concluded that although an attractive network can have a fixed shear modulus, its yield stress is not a singular property, but is strain rate dependent. [26,27] \*

When the attractive network is too 'stiff', a problem exists in determining its properties with conventional rheological tools, viz., the smooth surfaces of the rheological tool slips at the tool-slurry interface. Dzuy and Boger [18,19] have avoided this problem with the adaptation of the vane tool geometry commonly used in soil mechanics. Here, four flat vanes, spaced  $90^\circ$ , are attached to a central shaft. In essence, the vane replaces the central cylinder in the couette tool, i.e., it is assumed to be a cylinder of the same radius; torque, strain and strain rate are calculated as if it were a cylinder of the same radius. There is no possibility for slip in this geometry. Another

---

\* The yield stress ( $\tau_y$ ) is also estimated from shear stress vs. strain rate data, by assuming either a Bingham plastic model ( $\tau = \eta \dot{\gamma} + \tau_y$ ) or a Casson model ( $\tau^{1/2} = \eta^{1/2} \dot{\gamma}^{1/2} + \tau_y^{1/2}$ ) to estimate the yield stress by extrapolation of high shear rate data to zero strain rate ( $\dot{\gamma} \rightarrow 0$ ). Although this method is common, it neglects all data prior to flow, and the fact that data are rarely Newtonian at higher shear rates.

advantage is that the particle network is not strongly disturbed when the vane is inserted (conventional tools cause extensive flow when they are inserted). Griffiths et. al. [28] and Keentok et. al. [29] have analytically studied the vane tool. Dzuy and Boger[18] define the yield stress, with constant strain rate experiments, as the stress where the torque (stress) reaches a maximum value. Mewis and Meire [21], suggest that this measurement does not determine the yield stress of the network, but represents the stress where the rate in which the network is being broken is equal to the rate in which the network reforms. Since the yield strain is very large in these experiments, all evidence suggests that the network yields well before the torque reaches a maximum value. Although Dzuy's and Boger's 'yield stress' method is certainly useful for comparing the 'strength' of one network to another, it strongly over estimates the yield stress.

Alderman et. al. [20] have used the vane tool to measure the shear modulus of bentonite gels. In their experiments, they use the vane tool as if it were the central cylinder of in a couette geometry to determining the slope of the Hookian part of the stress vs strain curve in constant strain rate experiments. They show that the modulus measured with the vane tool is identical to that measured with the conventional couette geometry. Adderman et al. [20] also used the vane tool to determine the yield stress of the bentonite network at different strain rates.

The purpose of the present study was to obtain extensive shear moduli and yield stress data for attractive  $\text{Al}_2\text{O}_3$  networks produced by both adding salt to a dispersed slurry and formulating the slurry at the iso-electric point. In the present paper, we will discuss how these two properties are conceptually related to the particle pair potential and volume fraction of particles within the slurry.

### 3 Experimental Procedure

#### 3.1 Materials and Sample Preparation

An  $\alpha$ -aluminum oxide power, (AKP-50, Sumitomo Co, Japan), was used for the current study. Its average particle diameter is 0.2 microns (Leeds-Northrup Ultrafine Particle Analyzer). Figure 1 illustrates the zeta potential of this powder as a function of pH to show its iso-electric point is at pH 9.1.

Distilled water (14 mohm), nitric acid (Reagent grade, Fisher), ammonia hydroxide (Reagent grade, Fisher), and ammonia chloride (Reagent grade, Fisher) were used to prepare aqueous slurries. Slurry preparation initiated by adjusting the pH of the water to 2, then adding the powder while stirring. After all of the powder for the selected volume fraction was added to the distilled water, the slurry was ultrasonicated (Model W-380, Heat Systems-Ultrasonics) for 5-10 minutes. After ultrasonication, the desired amount of ammonia chloride (salt) was stirred into the slurry to produce the weakly attractive network discovered by Velamakanni et al. [10]. The pH of the system was then adjusted to the desired final pH and ultrasonicated again for 10 minutes. The slurry was then placed on a roller for at least two days prior to rheological experiments.

A large number of slurries were formulated of the powder with the averaged diameter of 0.2  $\mu\text{m}$ : pH 2 ( $\phi = 0.15$  to 0.40), pH 4 ( $\phi = 0.20$  to 0.50), pH 5 ( $\phi = 0.10$  to 0.40), pH 6 ( $\phi = 0.10$  to 0.30) and pH 9 ( $\phi = 0.10$  to 0.30), all containing salt concentrations up to at least 2.5 mole  $\text{NH}_4\text{Cl}$ .

#### 3.2 Rheological Measurements

Measurements were taken with one of two commercial rheometers (Rheometrics Dynamic Stress Rheometer (DSR) and Rheometrics Mechanical Spectrometer (RMS-800)). Although the vane tool was used for most measurements, the couette cell was used to obtain data at lower volume fractions where the torque was insufficient to use the vane tool with either rheometer. Data was also obtained with the couette cell to compare with data obtained with the vane tool. For the DSR, the diameters of the vane

and cup that held the slurry were 16mm and 32mm, respectively. For the RMS, they were 52.2mm and 25.4mm, respectively\*\*. These dimensions are well within the boundary conditions explored and defined by Boger [18] for the vane tool. For data analysis, the vane was assumed to be identical to a cylinder of the same diameter. Experiments were carried out by loading the slurry into the cup, positioning the cup in the rheometer, then inserting the vane into the slurry. Experience showed that the slurries did not need to sit in a quiescent state after insertion of the vane prior to the beginning of an experiment. However, it was discovered that once the measurement was initiated, successive experiments would not reproduce the initial measurement unless the vane was removed and reinserted into the slurry. For this reason, the slurry was never pre-sheared before any measurement. In addition, prior to each new measurement with the same slurry, the tool was removed and reinserted. Using this procedure, one could reproduce a previous measurement and use the same slurry for sequentially new experimental conditions.

The oscillatory method was used to obtain the data reported here. Strain sweep experiments, i.e. increasing strain amplitude at fixed frequency, were used to determine the 'yield strain' of the network at a frequency of 1 rad/sec. Experience showed that the frequency of 1 rad/sec was sufficiently large to obtain an elastic response from all the slurries investigated. A frequency sweep, i.e. increasing the frequency at fixed amplitude, was used to determine the shear modulus of the slurry. The plateau value of the shear modulus ( $G'$ ) was taken to be the shear modulus of the slurry. Figure 2 illustrates the results of a typical strain sweep experiment, showing that the behavior of the slurry changes from an elastic response ( $G'$  remains constant) to a flow response ( $G'$  decreases) with increasing strain amplitude. This figure also shows that the strain

---

\*\* It should be noted that initial measurements were carried out with a much more compliant vane. The realization that the vane was too compliant was obtained when all data at higher volume fractions of powder produced nearly the same value of the shear modulus, regardless of the apparent network strength.



amplitude where the slurry begins to flow is not unique, but occurs over a range of strain. Thus, for the present work, the yield strain was defined by extrapolating the linear line describing the region where the shear modulus is constant prior to flow (line d) to point where it intersects the line describing the non-linear behavior after flow (line e). The intersection of these two lines was assumed to be the yield strain of the network. With the assumption of a linear stress-strain relation up to the yield strain, the yield stress was determined from product of the yield strain and the shear modulus ( $\tau_y = \gamma_y G'$ .) Figure 3 illustrates a typical result of a dynamic frequency sweep, showing that the shear modulus remains relatively invariant with increasing frequency at high frequency.

## 4 Results

### 4.1 Comparison of Vane Tool and Conventional Tool

Figure 4 shows results of a dynamic frequency sweep obtained for a 30vol% alumina slurry at pH 6.0 with 0.5M  $\text{NH}_4\text{Cl}$ , using both a vane tool and the couette cell. As shown, both tools gave the same result for the shear modulus ( $G'$ ). However, the vane geometry seems to produce a smaller value of the loss modulus ( $G''$ ) at higher frequencies.

### 4.2 Shear Modulus

Figure 5 is a plot of the shear modulus for slurries containing the  $\text{Al}_2\text{O}_3$  powder prepared at pH 2.0 as a function of salt concentration. Each data point represents a different slurry and each curve represents a different volume fraction of alumina powder. The data shows that the shear modulus for slurries prepared with a specific volume fraction increases with salt concentration until the modulus appears to reach a constant value referred to as the 'saturation modulus'. In addition, the shear modulus increases with the volume fraction of powder. Similar data was obtained at pH 4, 5, and 6 i.e.,  $G'$  increased to a saturation value with increasing salt concentration and increased with volume fraction.

Data shown in Fig. 5 could be reduced to one common curve by dividing each data point by the volume fraction ( $\phi$ ) to the powder 4.7 for this specific series. Likewise, as shown in Fig. 6, all data obtained for slurries formulated at a common pH could be reduced to a common curve by dividing through by the following volume fraction dependence:

$$G' \propto \phi^{4.75 \pm 0.25} \quad (1)$$

The shear modulus data shown in Fig. 6 exhibit the following behavior: 1)  $G'$  increases as the pH moves closer to the iso-electric point (pH 9), 2)  $G'$  increases with salt concentration, reaching a saturation value at each pH\*\*\* and 3) the saturation modulus for pH 5.0 and 6.0 are identical to the modulus for slurries prepared at the iso-electric point (pH 9) and much larger than those of pH 2.0, and 4.0, and 4)  $G'$  for slurries formulated at the iso-electric point (pH 9) were relatively unaffected by additions of salt.

Prior to reaching the saturation modulus, the shear modulus vs salt concentration  $[c]$  data could be described with a power law function for slurries formulated at a common pH:

$$G' \propto [c]^{2 \pm .25} \quad (2)$$

#### 4.3 Apparent Yield Strain and Yield Stress

The extrapolated yield strain ( $\gamma_y$ ), determined with strain sweeps at a frequency of 1 rad/sec, was < 0.2 % for all slurries investigated. The yield strain was found to be related to the volume fraction of particles as:

$$\gamma_y \propto \phi^{-1.1 \pm .15}, \quad (3)$$

and, at a specific pH, related to the concentration  $[c]$  of salt as

$$\gamma_y \propto [c]^{-.85 \pm .10}, \quad (4)$$

Figure 7 is a plot of the apparent yield stress ( $\tau_y = \gamma_y G'$ ) vs salt concentration for the same slurries (pH 2.0) reported in Fig. 5. Because the apparent yield stress was determined with  $\tau_y = \gamma_y G'$ , were  $\gamma_y$  and  $G'$  were separately found to be dependent on the volume fraction of particles  $\phi$  and the salt concentration  $[c]$  at each specific pH, to fit on a common curve for each pH examined,

$$\tau_y \propto \phi^{3.6}, \quad (5)$$

as shown in Fig. 8. The relation between the apparent yield stress and salt concentration was

$$\tau_y \propto [c]^{1.15}, \quad (6)$$

As shown in Fig. 7, similar to shear modulus, the apparent yield stress increased with salt concentration to a saturation value\*\*\* for pH values indicative of a finite surface charge (pH values less than the iso-electric point). The saturation values for the yield stress at pH 5 and 6 are identical to the values for the slurries formulated at the isoelectric point (pH 9), which is relatively independent of salt concentration. \*\*\*

## 5 Discussion

The current data clearly show that the stiffness (shear modulus) and apparent strength (yield stress) of aqueous, alumina particle networks are a function of both the pH and salt content. Attractive networks formed by adding salt to a dispersed slurry (pH 2 and 4) are much weaker than the strongly attractive networks formulated at the

---

\*\*\* Increasing the  $\text{NH}_4\text{Cl}$  concentration to 5.5M, close to the solubility limit, at pH 2.0 and pH 4.0 did not change the values of either  $G'$  or  $\tau_y$ .

iso-electric point (pH 9). These results substantiate the previously reported behavior by Velamakanni, et al, [10] and Chang et al. [16] who obtained viscosity vs shear rate data and yield stress data for a limited number of slurries at pH 4 and 9. The current data further substantiates the initial hypothesis, i.e., the weakly attractive networks produced by adding salt to a dispersed slurry are a result of a pair potential characterized by a potential well. In addition, the current data show that for slurries formulated with a net surface charge ( $\text{pH} < 9$ ), both the shear modulus and yield stress systematically change with salt content, whereas slurries formulated at the iso-electric point (pH 9) are relatively independent of the salt content.

The mechanical properties of a static, attractive network are expected to depend on both the particle pair potential and the network configuration. Figure 9a schematically illustrates the potential between two particles as a function of their separation distance ( $h$ ) for a network where the particles are attractive, but do not touch. The dashed line illustrates the persistent, attractive van der Waals potential. The pair potential (solid line) is obtained by summing the persistent van der Waals attractive potential with a repulsive potential of an unspecified, physical origin. When the well is sufficiently deep to trap the particles, their Brownian motion is confined to vibration amplitudes that are limited by the potential well to produce an average equilibrium separation distance,  $h_{eq}$ , defined by the position of the potential well. Since  $h_{eq} > 0$ , particles in the network are attractive, but non-touching. Because the van der Waals potential always persists, the depth of the potential well will depend on the magnitude and range of the repulsive potential. When  $h_{eq}$  is large, i.e., when the range of repulsive potential is large, the depth of the potential well will be insufficient, relative to the kinetic energy of the particles, to form an attractive particle network. Thus, the network will only be attractive when the range of the repulsive potential is small, i.e., the repulsive potential must be short-range ( $\leq 10$  nm for particles considered here).

Figure 9b schematically illustrates the force ( $F = -\frac{dV}{dh}$ ) between the same two particles as a function of separation distance. When  $h = h_{eq}$ ,  $F = 0$ ; at this position, the second derivative,  $k = \left. \frac{d^2V}{dh^2} \right|_{h=h_{eq}}$ , is the effective 'spring constant' between each particle pair, [30-31] which must be related to shear modulus ( $G'$ ) of the network. The maximum force needed to separate the particle,  $F_{max}$ , occurs for a value of  $h$  ( $> h_{eq}$ ) where  $\frac{d^2V}{dh^2} = 0$ , i.e. the position of the inflection point on the potential curve (Fig. 9a). Since  $F_{max}$  is related to the force needed to break the network and allow it to flow, it is related to the yield stress of the attractive network.

Assuming that the van der Waals potential remains unchanged as the chemistry of the system is changed to vary the short-range repulsive potential, Fig. 9a schematically illustrates that the depth of the potential well is inversely related to the spring constant and the force ( $F_{max}$ ) needed to pull two particles apart. That is, for a given volume fraction of particles, the magnitude of both the shear modulus and yield stress is expected to increase as the chemistry of the system is changed to deepen the potential well.

For the data reported above, the strongest networks (largest modulus and apparent yield stress) were observed for slurries formulated at the iso-electric point (pH 9) where the pair potential is described with only the attractive, van der Waals potential. Weaker slurries are formulated at a lower pH, where the surface charge is finite and positive.

For a given pair potential, the mechanical properties of an attractive particle network will depend on the volume fraction of particles and the network connectivity. Figure 10 schematically illustrates the dependence of the normalized shear modulus ( $G'/G'_{max}$ ) on the normalized volume fraction ( $\phi/\phi_{max}$ ) for networks with two different connectivities.  $G'_{max}$  is the modulus for the most densely packed network,  $\phi_{max}$ .

One of the two networks is formed with identical, linear columns of particles, two particles per column. The relation between volume fraction ( $\phi$ ) and the particle radius ( $r$ ) is given by  $\phi = \frac{2\pi r^2}{3l^2}$ , where  $l$  is the length and width of the unit cell. For this linear column arrangement, the number of columns per unit area is

$$N = \frac{1}{l^2} = \frac{3\phi}{2\pi r^2} \quad (7)$$

When a stress ( $\tau$ ) is applied between the plates, each column will equally transmit a force given by

$$F_c = \frac{\tau}{N} = \frac{2\pi\tau r^2}{3\phi} = k\Delta h, \quad (8)$$

where  $k = \left. \frac{d^2V}{dh^2} \right|_{h=h_{eq}}$  is the 'spring constant', and  $\Delta h$  is the displacement of the

particles from their equilibrium separation distance,  $\Delta h = h - h_{eq}$ . Streng and Sonntag[32] use the following equation to relate  $\Delta h$  to the shear strain:

$$\Delta h = r\gamma \quad (9)$$

Rearrangement of the right hand side of eq (8) results in the relation between stress ( $\tau$ ) and strain ( $\gamma$ ):

$$\tau = \frac{3\phi k}{2\pi r^2} \Delta h = \frac{3\phi k}{2\pi r} \gamma = G'\gamma, \quad (10)$$

$$G' = \frac{3\phi k}{2\pi r} = \frac{3\phi}{2\pi r} \left. \frac{d^2V}{dh^2} \right|_{h=h_{eq}} \quad (11)$$

For the linear columnar network, Eq. (11) suggests that the modulus is linearly related to the volume fraction of particles as shown by the linear relation in Fig. 10.

Although the connectivity of particles in real, attractive particle networks is not known, some investigators [33-34] suggest that it could be described with a fractal dimension at low volume fractions, while others [35-36] have shown many

interpenetrating, percolative paths exist to support applied pressures at high volume fractions. These conceptual models suggest that the particle connectivity is very tortuous at all volume fractions. Since portions of the tortuous network are subjected to bending moments, they must be much more compliant than the linear, columnar network. The shear modulus as a function of volume fraction of such a tortuous network was modeled by Sen et al. [37]. They assumed a general isotropic particle pair potential (potential only depends on particle separation, without an angular dependence). In modeling the effect of volume fraction on the shear modulus, they changed the volume fraction of particles by randomly removing particles from a periodic array (face center cubic) of identical, spherical particles. Their model produced a power law function,  $G' \propto \phi^n$ , with  $n = 4.4$ , as shown by the non-linear relation in Fig. 10. The current work shows that the exponent for different series of slurries lies between  $4.5 \leq n \leq 5.0$  ( $n = 4.75 \pm 0.25$ ), suggesting a network similar to that modeled by Sen et al.

The power-law dependence on shear modulus and yield stress on volume fraction of particles has been documented often in the literature. Ball and Brown [38] have derived a power of 3.6 for the modulus of individual fractal aggregates. Sonntag and Russel [39] have found  $n$  in the relation  $G' \propto \phi^n$  to be 2.5 and 4.4 for fresh and aged polystyrene networks, respectively. Shih et. al. [40] have experimentally determined that  $n = 4.1$  for the modulus of agglomerated, platelike, boehmite alumina crystallites. Buscall et. al. [41] have found  $n = 4.3$  for the compressive yield stress of polystyrene latex systems aggregated with barium chloride. It is clear that these large values of  $n$  are due to the percolative nature of particle networks.

Although the shear modulus data shows that the configuration of the attractive network bears no resemblance to the linear column model, the yield strain is nearly inversely proportional to the volume fraction, i.e.,  $\gamma_y \propto \phi^{-1.1}$  or  $\approx \phi^{-1}$ , which is relation expected for the linear column model, where each column is expected to extend to the



same failure strain. Although less data exists for the yield stress of attractive networks, it is obvious that unlike the network modeled with linear particle arrays, which would break and flow once the maximum force was exceeded between any particle pair, due to their tortuous connectivity, real networks can exhibit a much greater extension (strain) prior to flow.

Our data shows that the non-DLVO force observed by Velamakanni et. al. [10] and Ducker et. al. [15] only exists in networks in which the particles have high surface charges, less than pH 4.0. When the pH was  $\geq 5$  and when sufficient salt was added, both the shear modulus and yield stress increased to the same values as slurries formulated at the iso-electric point, as predicted by DLVO theory. To insure that sufficient salt was added to the slurry formulated at pH 2 and 4, up to a 5.5 M  $\text{NH}_4\text{Cl}$  was added without any observed change in either the saturation modulus or the saturation yield stress. Conductivity measurements showed that all the electrolyte was completely dissolved at these concentrations.  $\text{NaCl}$ ,  $\text{KCl}$ , and  $(\text{NH}_4)_2\text{SO}_4$  were also added, but produced the same effect as the  $\text{NH}_4\text{Cl}$ . Further discussion of the effect of pH and salt will be presented in a companion paper that focus on the measurement and relation of surface charge density to the interparticle potential. [42]

## 6 Conclusions

Shear modulus and yield strength data suggest that there are two different interparticle regimes. For conditions where the particles have a low surface charge, the interparticle potential suggested by DLVO theory appears to predict the experimental results when excess salt is added, i.e., the strength of the attractive network become identical to that produced at the isoelectric point. On the other hand, when the particles have a high surface charge, evidence suggests that a non-DLVO, short-range repulsive force, as suggested by Velamakanni et. al. [10] and confirmed by Ducker et al. [15], must be added to the two other potentials in the conventional DLVO theory.

## Acknowledgment

This work was sponsored by the Office of Naval Research under contract No. N00014-92-J-1808.

## References

1. R.G. Horn, "Surface forces and their action in ceramic materials.", J. Am. Ceram. Soc., **73**, 5, 117-1135 (1990)
2. F.F. Lange, B.V. Velamakanni, J.C. Chang, and D.S. Pearson, Proceedings of the 11th. Riso International Symposium on Metallurgy and Materials Science: Structural Ceramics- Processing, Microstructure and Properties, Ed. J.J. Bentzen, J.B. Bilde-Sorensen, N. Christiansen, A. Horsewell, B. Ralph, Riso National Laboratory, Roskilde, Denmark, (1990)
3. B.V. Velamakanni, and F.F. Lange, "Method for Preparation of Dense Ceramic Products, U.S. Patent No. 5188780, Feb. 23, 1993
4. F.H. Baader, T.J. Graule, L.J. Gauckler, private communication, "Direct Coagulation Casting- A New Shaping Technique, Part I: Process principles, Part II: Application to Alumina, "Proceedings of the 8th CIMTEC - World Ceramics Congress and Forum on New Materials", Florence, Italy, June 29-July 4, 1994
5. Y.K. Leong and D.V. Boger, "Surface Chemistry Effects on Concentrated Suspension Rheology", J. Colloid and Interface Science, **136**, 1, (1990)
6. W.B. Russel, D.A. Saville, W.R. Schowalter, Colloidal dispersions, New York : Cambridge University Press, (1989)
7. T. Kramer, F.F. Lange, "Rheology and Particle Packing of Chem- and Phys-Adsorbed, Alkylated Silicon Nitride Powders", J. Am. Ceram. Soc., **77**, 4, 922-928, (1994)
8. J.C. Chang, B.V. Velamakanni, F.F. Lange, and D.S. Pearson, "Centrifugal consolidation of  $\text{Al}_2\text{O}_3$  and  $\text{Al}_2\text{O}_3/\text{ZrO}_2$  composite slurries vs. interparticle

- potentials: particle packing and mass segregation.", J. Am. Ceram. Soc., **74**, 9, 2201-4, 1991
9. J.C. Chang, F.F. Lange, D.S. Pearson, J.P. Pollinger, "Pressure sensitivity for particle packing of aqueous  $\text{Al}_2\text{O}_3$  slurries vs interparticle potential.", J. Am. Ceram. Soc., **77**, 5, 1357-60, (1994)
  10. B.V. Velamakanni, J.C. Chang, F.F. Lange, and D.S. Pearson, "New Method for Efficient Colloidal Particle Packing via. Modulation of Repulsive Lubricating Hydration Forces", Langmuir, **6**, 1323-1325 (1990)
  11. B.V. Velamakanni, and F.F. Lange, "Effect of Interparticle Potentials and Sedimentation on Particle Packing Density of Bimodal Particle Distributions During Pressure Filtration", J. Am. Ceram. Soc., **74**, 1, 166-72, (1991)
  12. J. Israelachvili, Intermolecular & Surface Forces, Second Edition, Academic Press, San Diego, (1991)
  13. P. Hiemenz, Principles of Colloid and Surface Chemistry, Second Edition, Marcel Dekker, New York, (1986)
  14. R.J. Hunter, Foundations of Colloidal Science, Volume 1, Oxford University Press, New York, (1989)
  15. W.A. Ducker, Z. Xu, D.R. Clarke, J.N. Israelachvili, "The Forces between Alumina Surfaces in Salt Solutions: Non-DLVO Forces and the Implications for Colloidal Processing", J. Am. Ceram. Soc., **77**, 2, 437-443, (1994)
  16. J.C. Chang, F.F. Lange, D.S. Pearson, "The Viscosity and Yield Stress of  $\text{Al}_2\text{O}_3$  Slurries Containing Large Concentrations of Electrolyte", J. Am. Ceram. Soc., **77**, 1, 19-26, (1994)
  17. D. Boger, "Measuring the Flow Properties of Yield Stress Fluids", Annual Review of Fluid Mechanics, **24**, 47-88(1992)
  18. Q.D. Nguyen, and D. Boger, "Yield Stress Measurement for Concentrated Suspensions", J. Rheology, **27**, 321-49(1983)

19. Q.D. Nguyen, and D. Boger, "Direct Yield Stress Measurement with the Vane Method", *J. Rheology*, **29**, 335-47(1985a)
20. N.J. Alderman, G.H. Meeten, and J.D. Sherwood, "Vane rheometry of bentonite gels", *J. of Non-New. Fluid Mec.*, **39**, 292-310(1991)
21. J. Mewis, C. Meire, "Yielding in Weakly Flocculated Systems", *Advance in Rheology*, ed. B. Mena, A. Garcia-Rejon, C. Rangel Nagaile, 2: Mexico City, 591-598(1984)
22. J.D. Sherwood and G.H. Meeten, "The use of the vane to measure the shear modulus of linear elastic solids", *J. of Non-New. Fluid Mec.*, **41**, 101-118(1991)
23. R. Buscall, "The Elastic Properties of Structured Dispersions: A Simple Centrifuge Method of Examination, *Colloids and Surfaces*", **5**, 269-283 (1982)
24. R. Buscall, and L. White, "The Consolidation fo Concentrated Suspensions", *J. Chem. Soc. Faraday Trans.*, **83**, 873-891 (1987)
25. J. Ferry, *Viscoelastic Properties of Polymers*, 2nd. Edition, Wiley Press, New York, (1970)
26. G. Astarita, "Letter to the Editor: The engineering reality of the yield stress", *J. of Rheology*, **34**, 2, 275-277 (1990)
27. J.P. Hartnett and R. Y. Z. Hu, "Technical Note: The Yield Stress-An Engineering Reality", *J. of Rheology*, **33**, 671 (1989)
28. D.V. Griffiths, and P.A. Lane, "Finite Element Analysis of the Shear Vane Test", *Computers and Structures*, **37**, 6, 1105-1116(1990)
29. M. Keentok, J.F. Milthorpe, "On the shearing zone around rotating vanes in plastic liquids: theory and experiment.", *J. Non-Newtonian Fluid Mechanics*, **17**, 23-25(1985)
30. R. Buscall, J.W. Goodwin, M.W. Hawkins, and R.H. Ottewil, "Viscoelastic Properties of Concentrated Latices", *J. Chem. Soc. Faraday Trans. 1*, **78**, 2889-2899 (1982)

31. R.W. Zwanzig and R. D. Mountain, "High-Frequency Elastic Moduli of Simple Fluids", *J. Chem. Phys.*, **43**, 4464, (1965)
32. H. Sonntag, and K. Streng, Coagulation Kinetics and Structure Formation, Plenum Press, New York, 172-175, (1987)
33. M.Y. Lin, H.M. Lindsay, D.A. Weitz, R.C. Ball, R. Klein, and P. Meakin, "Properties of Fractal Colloid Aggregates", *Nature*, **339**, 1, 360-362, (1989)
34. R. Jullien, "A new model of cluster aggregation", *J. Phys. A: Math. Gen.*, **19**, 2129-2136, (1986)
35. L.G.B. Bremer, T. van Vliet, P. Walstra, "Theoretical and Experimental Study of the Fractal Nature of the Structure of Casein Gels", *J. Chem. Soc. Faraday Trans. I*, **85**, 3359, (1989)
36. L.G. B. Bremer, B.H. Bijsterbosch, R. Schrijvers, T. van Vliet, and P. Walstra, "On the fractal nature of the structure of acid casein gels", *Colloids and Surfaces*, **51**, 159-170, (1990)
37. S. Feng, and P.N. Sen, "Percolation on Elastic Networks: New Exponent and Threshold", *Phy. Rev. Let.*, **52**, 3, 216-219, (1984)
38. W.D. Brown, pH.D. Thesis (Department of Physics, University of Cambridge, 1987)
39. R.C. Sonntag and W.B. Russel, "Elastic Properties of Flocculated Networks", *J. of Col. and Interface Science*, **116**, 2, 485-489, (1987)
40. W.H. Shih, W.Y. Shih, S.I. Kim, J. Liu, and I.A. Aksay, "Scaling Behaviour of the Elastic Properties of Colloidal Gels", *Physical Review A*, **42**, 8, 4772-4779, (1990)
41. R. Buscall, P.D. Mills, J.W. Goodwin, and D.W. Lawson, "Scaling Behaviour of the Rheology of Aggregate Networks formed from Colloidal Particles", *J. Chem. Soc. Faraday Trans. 1*, **84**, 12, 4249-4260, (1988)

42. J. A. Yanez and F. F. Lange, "Relation Between Surface Charge Density, Salt Concentration, Rheological Properties and Pair Potentials for Aqueous  $\text{Al}_2\text{O}_3$  Slurries,"

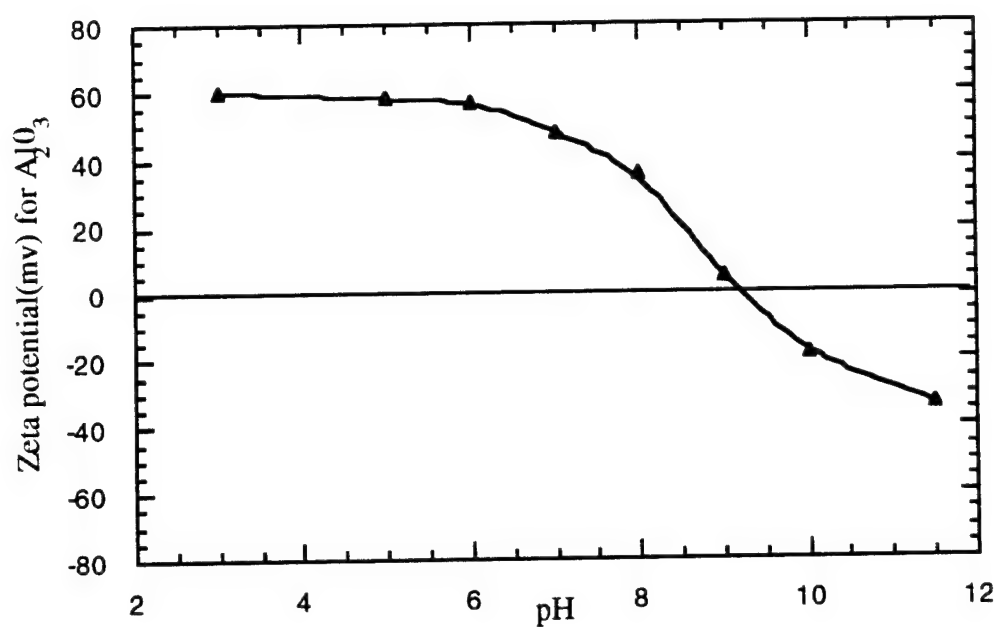


Figure 1 Zeta Potential of  $\text{Al}_2\text{O}_3$  powder versus pH.



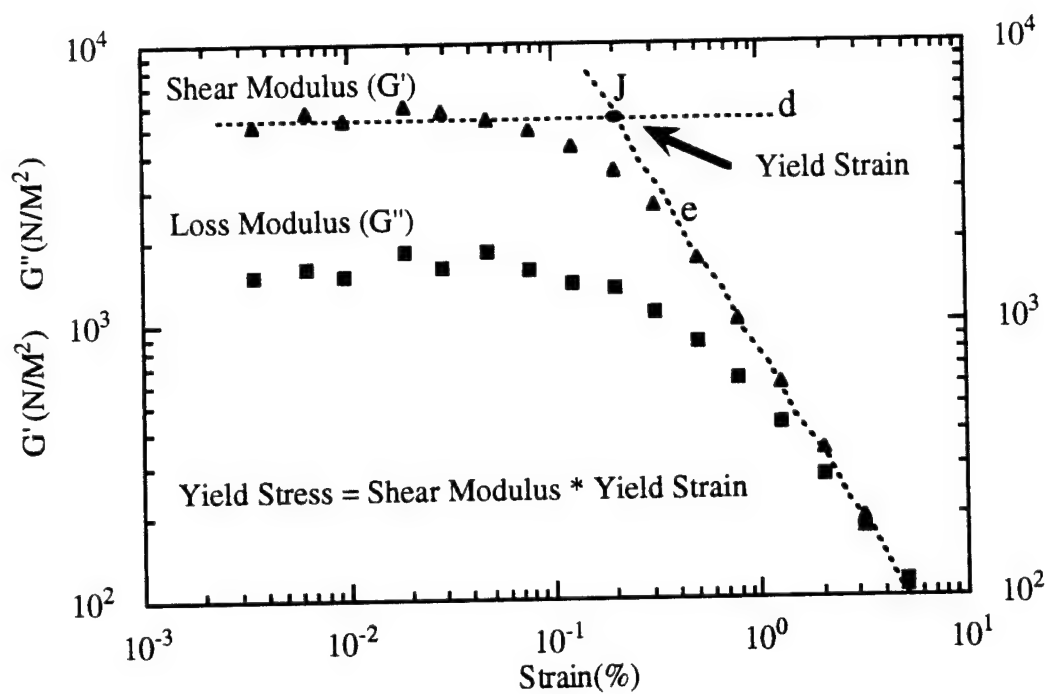


Figure 2 Technique for the determination of the yield stress for a pH 4.0, 2.5M  $NH_4Cl$ , 20vol%  $Al_2O_3$  particle network.

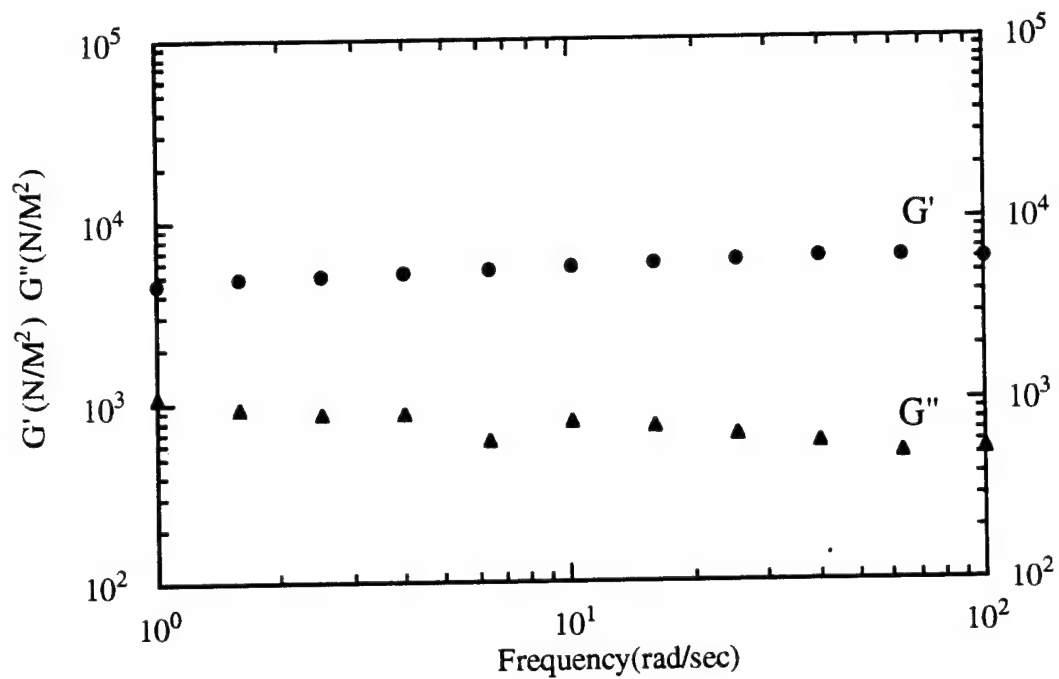


Figure 3 Determination of the shear modulus for a pH 4.0, 2.5M  $\text{NH}_4\text{Cl}$ , 20vol%  $\text{Al}_2\text{O}_3$  particle network.

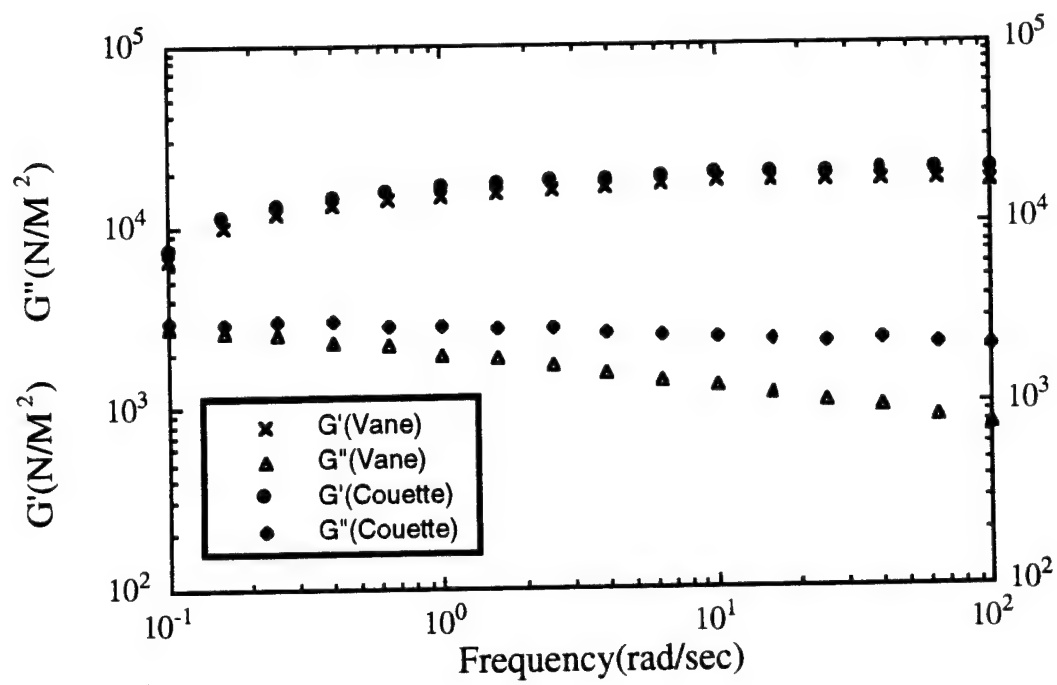


Figure 4 Comparison of vane and couette using a 30vol% pH 6.0, 0.5M  $\text{NH}_4\text{Cl}$ , alumina slurry.

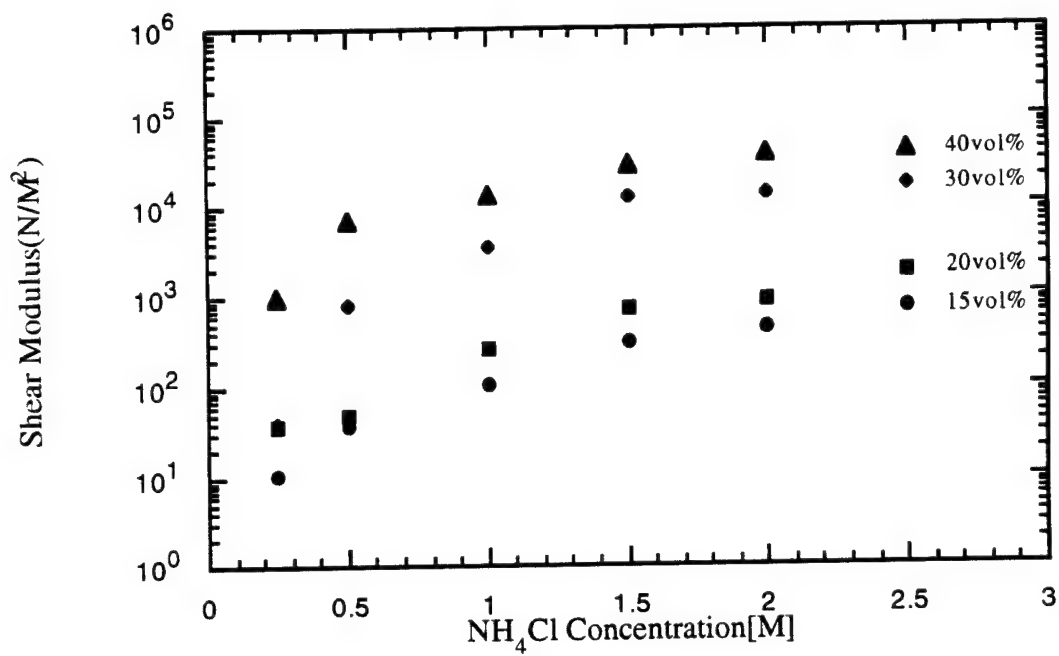


Figure 5 For various volume fractions of particles, shear modulus versus electrolyte concentration at fixed surface charge (pH 2.0).

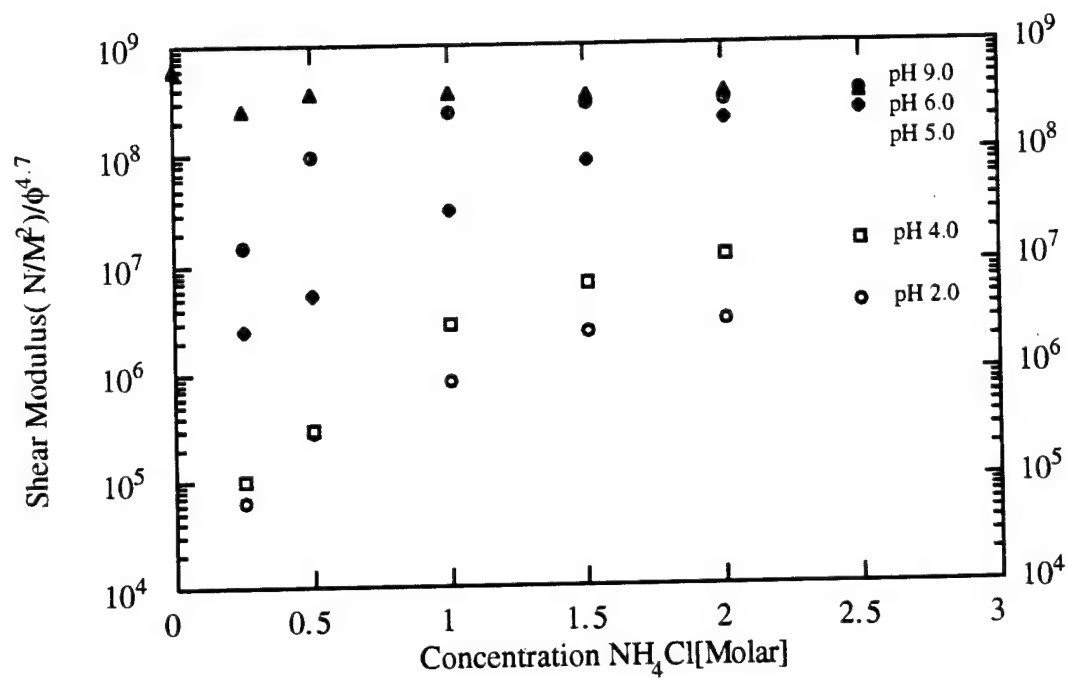


Figure 6 Shear modulus, normalized by the volume fraction dependence, versus concentration of electrolyte.

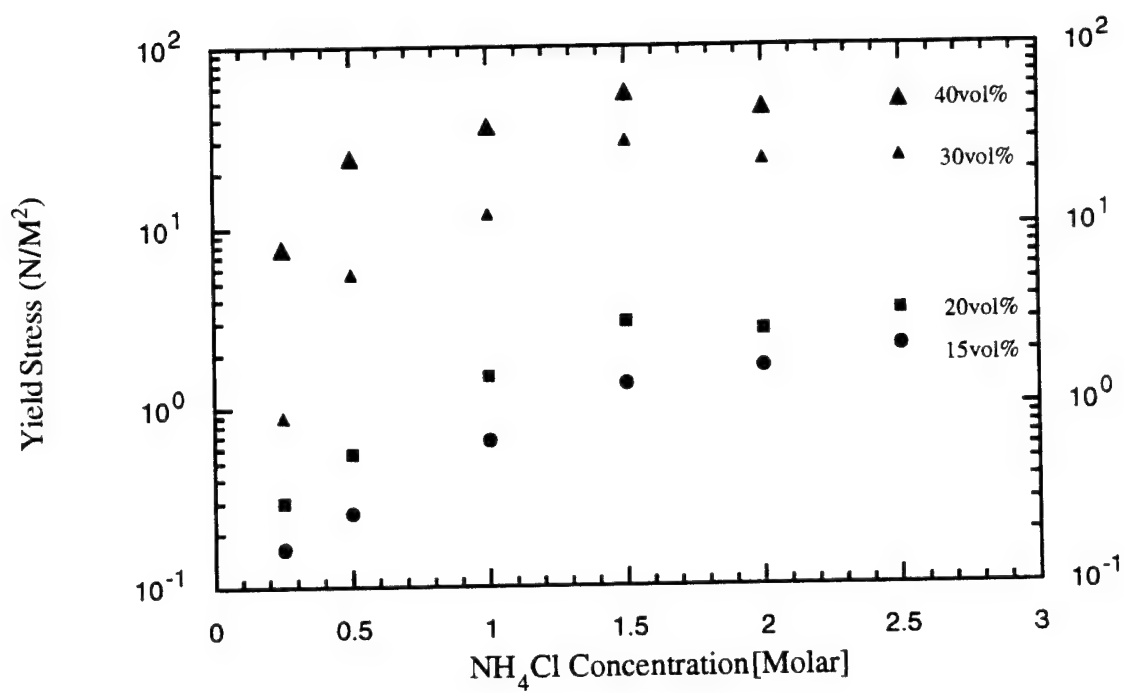


Figure 7 For various volume fractions of Al<sub>2</sub>O<sub>3</sub> particles, yield stress versus electrolyte concentration at fixed surface charge (pH 2.0).



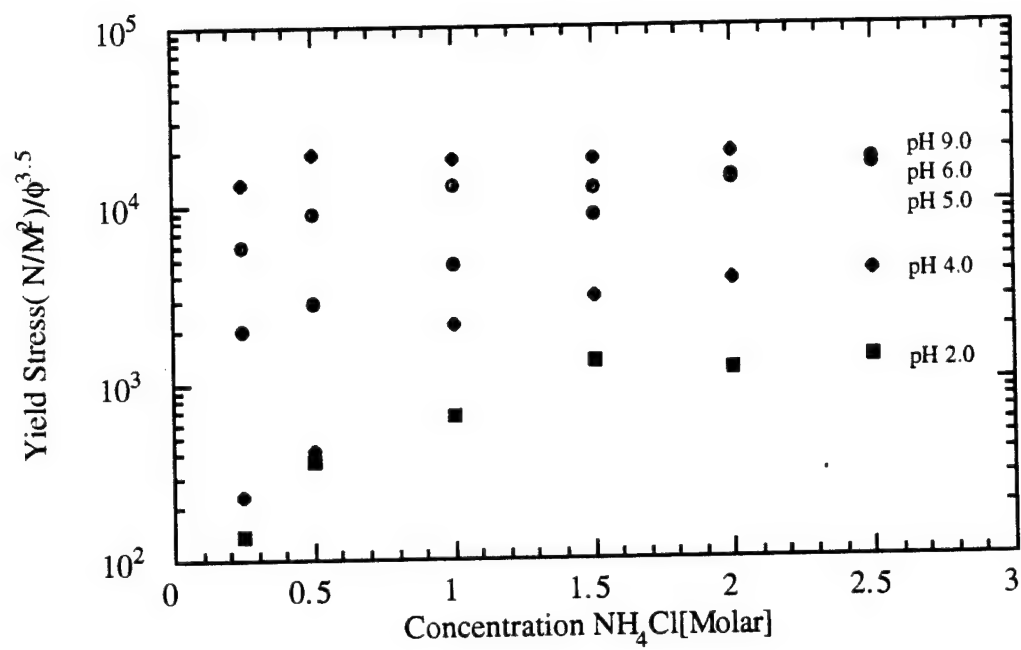


Figure 8 Yield Stress, normalized by the volume fraction dependence, versus concentration of electrolyte.

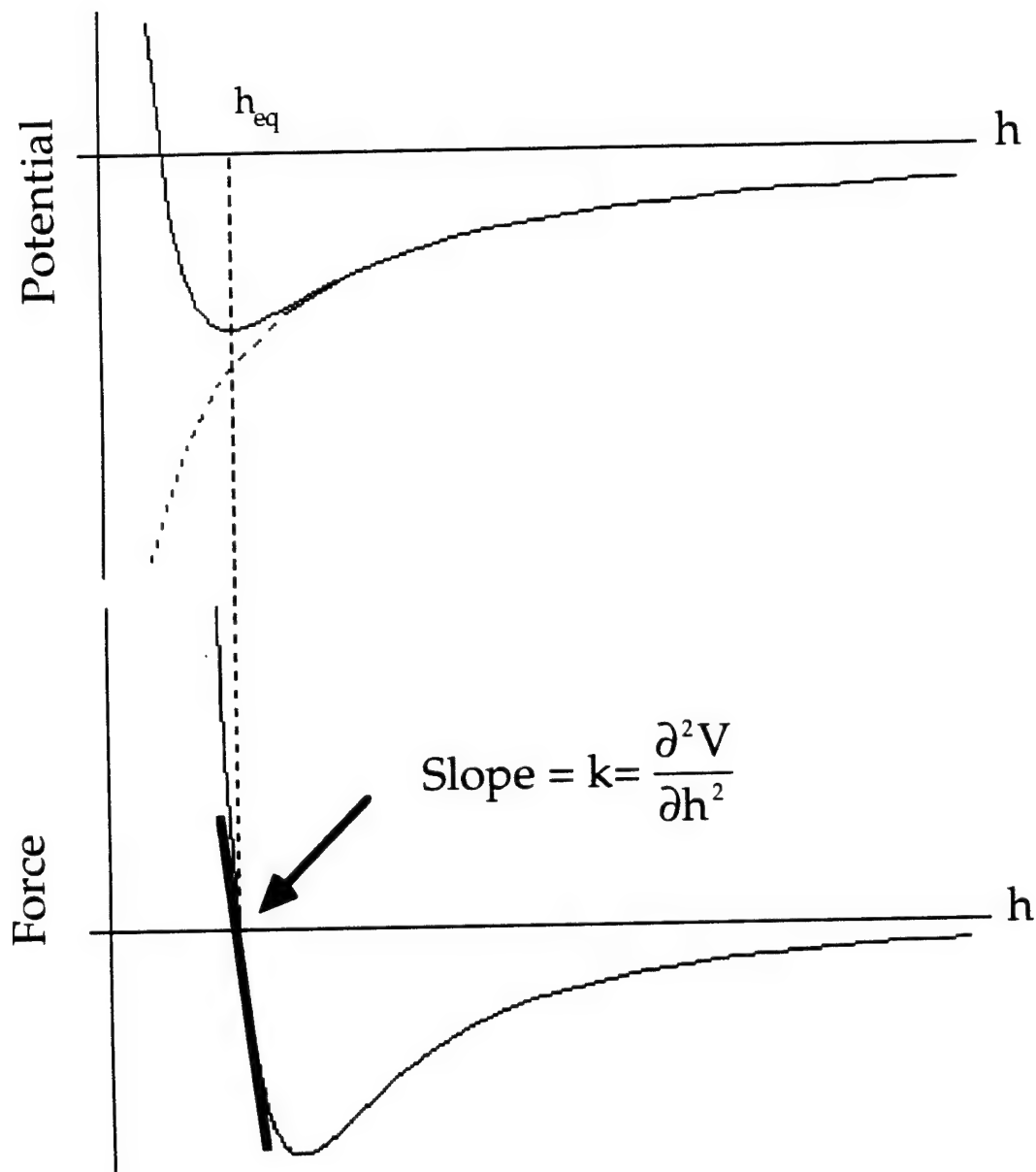


Figure 9 a) shows a schematic of how the two particle potential varies with particle separation distance; b) shows how the slope of the force vs. separation distance curve is related to the spring constant  $k$  (i.e.  $\frac{\partial^2 V}{\partial h^2}$ ).

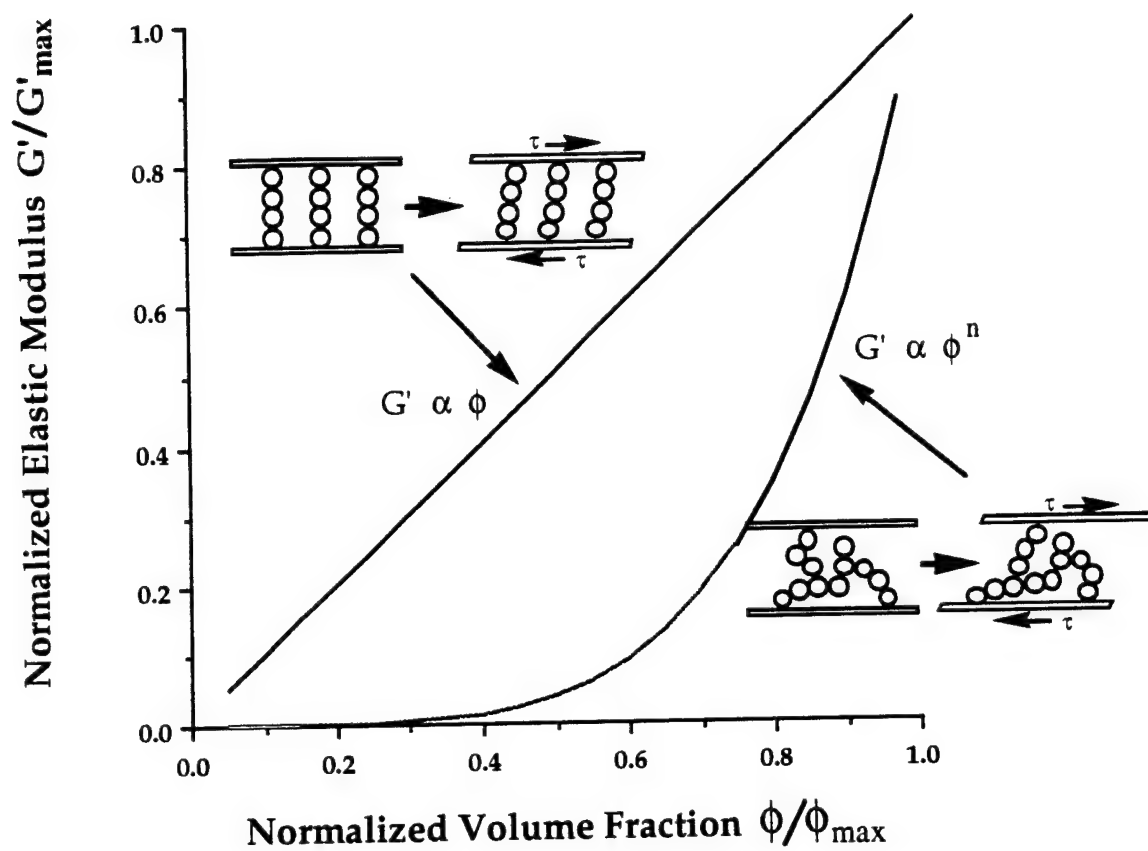
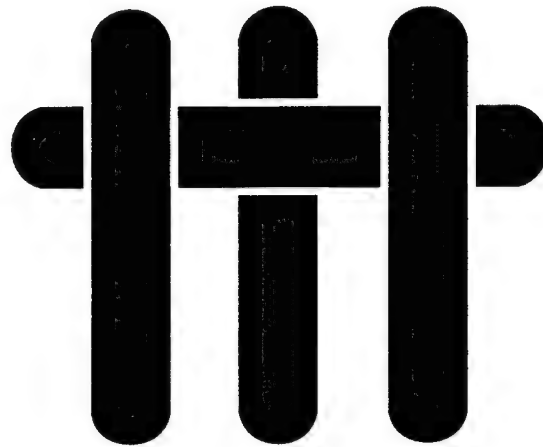


Figure 10 Schematic illustrating percolative nature of particle networks.

# **M A T E R I A L S**



**Technical Report Number 16**

## **Cracking of Laminates Subjected to Biaxial Tensile Strains**

**C. Hillman, Z. Suo, and F.F. Lange**

**Sent to: J. Amer. Ceramic Society**

**February 1, 1994 through January 31, 1995**

**Office of Naval Research**

**Grant No. N00014-90-J-1441**

**Fred F. Lange**

**Principal Investigator**

**Materials Department  
University of California  
Santa Barbara, CA 93106**

# CRACKING OF LAMINATES SUBJECTED TO BIAXIAL TENSILE STRAINS

C. Hillman, Z. Suo, and F. F. Lange

Materials Department

University of California, Santa Barbara

Santa Barbara, CA 93106

## Abstract

During the processing of laminar ceramic, biaxial, residual stresses can arise due to differential thermal contraction between unlike layers. If these stresses are tensile in nature, they can cause pre-existing flaws to extend across the layer and into the adjacent layers and then tunnel until they meet either another crack or a free surface. A previous analysis has shown that for a given residual stress there is a critical layer thickness ( $t_c$ ), below which no tunnel cracks will exist, regardless of initial flaw size. Here, the previous analysis was modified to take into account the crack extension into adjacent layers. To determine the validity of the analysis, laminates composed of alternating layers of zirconia and alumina/zirconia were fabricated by a sequential centrifugation technique. The composition of the alumina/zirconia layer was varied to change the biaxial, tensile stresses in the zirconia layer. Observations were then made to determine the critical layer thickness for tunnel cracks and their extension into the adjacent layers. These observations were compared to the theoretical predictions.

## 1. Introduction

Layered materials play an important role in technical applications. They have long been used in the microelectronics industry, as multilayer ceramic substrates [1], capacitors [2], and fuel-air sensors [3]. Ceramic laminates are currently being considered for structural applications [4-9] to impart damage tolerance for conditions where cracks extend at constant strain. The analysis and observations reported here also applies to two materials that are bonded together by a layer of a third material, as either an adhesive [10,11] or a braze [12].

During processing, residual stresses can arise within these laminates due to differential strains developed during drying, pyrolysis of binders, densification and contraction during cooling. If the residual tensile stress is large enough, it will cause pre-existing flaws to "tunnel" laterally until it reaches a free surface (either the surface of the laminate or another tunnel crack). In thick layers subjected to biaxial tension, multiple tunnel cracks produce a mud crack pattern, similar to those seen in thin films [13] and brittle adhesive layers [10,11].

Ho and Suo [14] developed a strain energy release rate expression for the tunnel crack in layers subjected to biaxial tension to show that for a given residual stress, a critical layer thickness exists below which no tunnel cracks will exist, regardless of the initial flaw size. The purpose of this paper was to experimentally verify Ho and Suo's theoretical predictions, which if correct, would allow crack-free ceramic laminates to be processed with a high degree of reliability. A similar paper on steady-state cracking in thin films was previously reported by Hu and Evans [15].

The ceramic laminates used in this experiment were composed of a thin zirconia layers sandwiched between two thicker alumina/zirconia layers (bulk material). The laminate was densified at high temperature. During cooling, if the layers were separated, the zirconia layer would shrink more than the bulk alumina/zirconia due to its higher

coefficient of thermal expansion (CTE),  $\alpha$  (Fig. 1). Because the zirconia layer is biaxially constrained from shrinking, a residual, tensile strain arises,

$$\epsilon_r = \int_{T_i}^{T_f} (\alpha_{Zr} - \alpha_{Al/Zr}) dT, \quad (1)$$

where  $T_i$  and  $T_f$  are the initial and final temperatures during cooling, and  $\alpha_{Zr}$  and  $\alpha_{Al/Zr}$  are the CTE's of the zirconia layer sandwiched between the alumina/zirconia layers, respectively. By varying the composition of the bulk alumina/zirconia layer, and thus varying  $\alpha_{Al/Zr}$ , the residual strain was changed in the thinner zirconia layers. The residual stress in the thin zirconia layer can be determined by [14]

$$\sigma_r = \frac{\epsilon_r E_{Zr}}{1 - \nu_{Zr}} \left[ 1 + \frac{t}{w} \frac{E_{Zr} / (1 - \nu_{Zr})}{E_{Al/Zr} / (1 - \nu_{Al/Zr})} \right]^{-1}, \quad (2)$$

where  $t$  and  $w$  are the thicknesses of the  $ZrO_2$  and the alumina/zirconia layers, and  $E$  and  $\nu$  are the elastic properties of the two layers. The stress state was simplified by forming the laminate such that the ratio  $t/w \ll 1$  (i.e., the alumina/zirconia layers are assumed to be semi-infinite). The residual stress in the zirconia layer becomes

$$\sigma_r = \frac{\epsilon_r E_{Zr}}{1 - \nu_{Zr}} \quad (3)$$

and the stress in the alumina/zirconia layers is reduced to zero.



## 2. Experimental Method

The laminates fabricated in this study consisted of thin layers of either tetragonal-Zr(3Y)O<sub>2</sub> or cubic-Zr(8Y)O<sub>2</sub><sup>a</sup> (thicknesses ranging between 10 μm to 500 μm) sandwiched between thick layers of Al<sub>2</sub>O<sub>3</sub>/Zr(Y)O<sub>2</sub> (≈ 3000 μm). Several Al<sub>2</sub>O<sub>3</sub>/Zr(Y)O<sub>2</sub> compositions were used in order to determine the critical thicknesses of Zr(Y)O<sub>2</sub> as a function of residual stress. These laminates were fabricated by a sequential centrifugation method described elsewhere. [6,16] The sequential centrifugation method utilizes a new colloidal processing technique [17,18] where a short-range repulsive potential is produced by adding salt (e.g., NH<sub>4</sub>Cl) to a dispersed, aqueous slurry. The short-range repulsive potential produces a weakly attractive particle network that allows particles to pack to a high relative density by either pressure filtration [17,18] or centrifugation [19], and prevents mass segregation during centrifugation [20].

A dispersed, aqueous slurry containing 0.005 volume fraction of Zr(Y)O<sub>2</sub> powder<sup>b</sup> was prepared at pH 2; 1.0 M of NH<sub>4</sub>Cl was then added to create a weakly attractive network. This slurry was used to produce thin Zr(Y)O<sub>2</sub> layers. In a similar manner, a second slurry was prepared containing 0.10 volume fraction of Zr(Y)O<sub>2</sub> and Al<sub>2</sub>O<sub>3</sub><sup>c</sup> powders (0.50 volume fraction each) was used to produce thick Al<sub>2</sub>O<sub>3</sub>/Zr(Y)O<sub>2</sub> layers. A volume V of the appropriate slurry containing the volume fraction of powder,  $\phi$ , was poured into the centrifuge tube, of area A, to form a layer of thickness

$$t = \frac{V\phi}{A}.$$

By changing either the volume fraction of powder in the slurry or the volume poured into the tube, one could vary the desired layer thickness formed during centrifugation. For the current study, the predetermined volume of the Al<sub>2</sub>O<sub>3</sub>/Zr(Y)O<sub>2</sub> slurry was poured into a

---

<sup>fa</sup> In the rest of the paper, t-Zr(3Y)O<sub>2</sub> and c-Zr(8Y)O<sub>2</sub> will both be referred to as Zr(Y)O<sub>2</sub> whenever it is more convenient

<sup>b</sup> Zr(Y)O<sub>2</sub> powder: TZ-3Y, TZ-8Y, Tosoh, Tokyo, Japan

<sup>c</sup> Al<sub>2</sub>O<sub>3</sub> powder: AKP-50, Sumitomo Chemical Co., New York

50 ml centrifuge tube <sup>d</sup> and centrifuged at 3200 rpm (centripetal acceleration ~ 1900 g's) for 2 hours (optimum time for maximum particle packing density determined in Ref. 20). The tubes were accelerated slowly up to the highest speed in order to ensure a smooth surface, and a uniform layer thickness. After forming one thick  $\text{Al}_2\text{O}_3/\text{Zr}(\text{Y})\text{O}_2$  layer, the clear supernatant was poured off, a predetermined volume of the  $\text{Zr}(\text{Y})\text{O}_2$  slurry was introduced into the tube to form a thin  $\text{Zr}(\text{Y})\text{O}_2$  layer by centrifugation. This process was repeated until the desired number of thin  $\text{Zr}(\text{Y})\text{O}_2$  layers were formed, each with a different thickness, sandwiched between much thicker  $\text{Al}_2\text{O}_3/\text{Zr}(\text{Y})\text{O}_2$  layers.

The laminates were air-dried and then heated at 2 °C/minute to 1500 °C for one hour to produce dense, laminar specimens. The laminates were sectioned by diamond cutting, polished and then examined with a scanning electron microscope for cracks (SEM) <sup>e</sup>. The layer thickness for which no cracks were observed was determined to be the critical layer thickness.

Bodies of all the compositions used to form laminar specimens were also consolidated to make specimens to measure coefficients of thermal expansion, which were used to help determine the residual stress in the  $\text{Zr}(\text{Y})\text{O}_2$  layer. CTE measurements were made courtesy of both Harrop Industries (Columbus, OH) and Rockwell International Science Center to temperatures of 1500 °C. Theoretical values of the CTE were also calculated [21] for the different alumina/zirconia compositions using the measured CTEs for the two end members and their elastic properties.

The fracture toughness of the embedded zirconia layers was determined using the Single-Edge-Precracked-Beam (SEPB) method [22]. Rectangular beam specimens (3mm x 4mm x 30mm) were used. Three indents were used to introduce small cracks in the center of the tensile face (30kg loads for t- $\text{Zr}(\text{3Y})\text{O}_2$ ; 10 kg loads for c- $\text{Zr}(\text{8Y})\text{O}_2$ ). A precrack was "popped-in" using the bridge-indentation apparatus described in ref. [22]. Once the precrack met the conditions of ASTM E399 8.2 (parallel to the thickness direction, equal length on both sides of the beam), its length was measured, and the beam was loaded to

---

<sup>d</sup> 50 ml polyethylene centrifuge tubes, Nalgene

<sup>e</sup> 840 SEM, JEOL, Tokyo, Japan

failure in four-point bend.  $K_{Ic}$  was calculated using the K function reported by Srawley [23].

### 3. Results

#### 3.1 Thermal Expansion and $K_{Ic}$ values

The CTE results, measured courtesy of Harrop Inc., are shown in Figure 2; data measured courtesy of Rockwell Science Center are reported in Table 1 along with calculated CTE values. It can be seen both experimental data sets are in agreement with one another, and these are in good agreement with theoretical values. The CTE for the various compositions and the  $K_{Ic}$  values for t-Zr(3Y)O<sub>2</sub> and c-Zr(8Y)O<sub>2</sub> are listed in Table II along with other relevant material properties.

#### 3.2 Tunnel Crack Observations

Two types of cracks were observed in the Zr(Y)O<sub>2</sub> layers, i.e., cracks with a large opening displacement ( $\geq 30 \mu\text{m}$ ) as shown in Fig. 3a and cracks with a small opening displacement ( $\leq 2 \mu\text{m}$ ) shown in Fig. 4a. Evidence suggested that the cracks with a large opening displacement were caused by differential shrinkage before densification. This was concluded from three observations. First, the large crack opening could only be caused by the differential shrinkage strain associated with the differential particle packing of the materials that formed the two different layers. The relative density of the alumina/zirconia compositions, which varied from 0.56 (high Al<sub>2</sub>O<sub>3</sub> content) to 0.47, was much higher than that of pure zirconia ( $\approx 0.40$ ). Thus the zirconia layers would shrink more than the adjacent alumina/zirconia layers during densification. Second, the surface morphology of the crack with the large opening displacement was composed of smooth, round grains, identical to that of a free surface of the densified body as shown in Fig. 3b. Third, Fig. 3c shows that the ends of the crack partially re-sintered where it penetrated into the adjacent Al<sub>2</sub>O<sub>3</sub>/Zr(Y)O<sub>2</sub> layer. Based on this evidence, it was concluded that the cracks

with the large opening displacement were more than likely formed during drying, and that their large opening displacement was produced by differential shrinkage during densification. (Most of the cracks with the large opening displacement were observed during initial experiments, before a systematic method was developed to dry the specimens for densification.)

The surface of cracks with the small opening displacement was exposed by fracturing diamond cutting beams that include the crack. These surfaces (Fig. 4b) were identical to surfaces that were known to be produced by fracture. Figure 4c shows the fracture surface of a tunnel crack that extended into the adjacent  $\text{Al}_2\text{O}_3/\text{Zr(Y)O}_2$  layer, which occurred when the thickness of the adjacent  $\text{Zr(Y)O}_2$  layer was greater than the critical value as discussed below. In general, at least two crack front positions could be observed associated with the tunnel crack as shown in Fig. 4c. This observation showed that the tunnel crack extended at least twice during cooling. The second position was produced when the beam was fractured to reveal the surface of the tunnel crack. Only cracks with the small opening displacement, produced during cooling, will be of continued concern here.

The thickness of the  $\text{Zr(Y)O}_2$  layer above which tunnel cracks were observed is detailed in Fig. 5 for both the tetragonal and cubic layers as a function of the composition of the adjacent  $\text{Al}_2\text{O}_3/\text{Zr(Y)O}_2$  layers. The extension of the tunnel crack into the adjacent  $\text{Al}_2\text{O}_3/\text{Zr(Y)O}_2$  layers, detailed for laminates containing the  $0.5\text{Al}_2\text{O}_3/0.5\text{Zr(Y)O}_2$  layers, is shown in Fig. 6 as  $a/t$  vs  $t$ , where  $a$  is the full length of the crack, including the portion that extends into the adjacent  $\text{Al}_2\text{O}_3/\text{Zr(Y)O}_2$  layers, and  $t$  is the thickness of the  $\text{Zr(Y)O}_2$  layer.

## 4. Discussion

### 4.1 Crack Penetration and Tunneling Analysis

The previously reported [14] fracture mechanics analysis that defined the critical thickness for tunnel cracking did not consider crack extension into the adjacent layers, which is observed here and is obvious in hindsight. The analysis that combines this extension into the adjacent layers with the tunneling phenomena will be described in the following paragraphs.

Consider a crack of length  $a$ , that pre-exists within a layer of material, of thickness  $t$ , under biaxial, residual tension due to the constraint of much thicker, adjacent layers. For the moment, we will consider that both materials have identical elastic properties. Let us assume that the crack is allowed to extend because its strain energy release rate is greater than the material's critical value. We also assume that the crack can extend across the interface into the adjacent, thicker layers and continue its extension as a tunnel crack, i.e., a crack that extends the length of the layer. During tunneling, the cross-section of the crack can be described as a slit crack. The strain energy release rate function for a slit crack within a layer subjected to tension and bounded by adjacent layers that contain no stress is given in Tada, et. al. [24] by

$$G_s = \left( \frac{2}{\pi} \right) \frac{\sigma^2}{E_1^*} \left( \frac{a}{t} \right) \left( \sin^{-1} \left( \frac{t}{a} \right) \right)^2 t, \quad (4)$$

where,  $E_1^*$  is  $E_1/(1-\nu_1^2)$ ,  $E_1$  and  $\nu_1$  being the elastic modulus and Poisson's ratio of the tensile layer. As previously detailed, the condition for crack extension along the layer (tunneling) is given by

$$G_t = \frac{Z\sigma^2 t}{E_1^*}, \quad (5)$$

where  $Z = \pi/4$  when the elastic properties of the two materials are identical. In general,  $Z$  is a dimensionless driving force dependent upon elastic mismatch, crack geometry and loading conditions [25].

As shown in Fig. 7, both  $G_s$  (eq. 4) and  $G_t$  (eq. 5) can be normalized by  $\frac{\sigma^2 t}{E_1^*}$ , and plotted as a function of  $a/t$ . The extension of a pre-existing crack with a normalized size,  $a/t < 1$ , will require that the value of the strain energy release rate function,  $G_s$ , given by eq. 4, must become  $\geq G_c$ , the critical strain energy release rate for the material under tension. On the other hand, for such a crack to tunnel along the layer, the value of  $G_t$  given by eq. 5, must become  $\geq G_c$ .

With knowledge of  $G_c$  and  $E^*$  for the tensile layer material, and  $\sigma$  within the layer, Fig. 7 can be used as a 'map' to describe the conditions for crack extension within a tensile layer of a thickness  $t$ . For a given layer thickness, the value of  $\frac{G_c E_1^*}{\sigma^2 t}$  will decrease during cooling due to an increase in the residual stress; or, for a given residual stress, the value of  $\frac{G_c E_1^*}{\sigma^2 t}$  will decrease with increasing layer thickness. The conditions for crack extension (either  $G_s$  or  $G_t \geq G_c$ ) occur when the normalized  $G_c$  crosses into the 'hatched area' of this graph. This hatched area contains two different regions. One is where the pre-existing crack simply extends into the adjacent layers, but does not tunnel. Of greater interest is the second region where the crack both extends into the adjacent layers and tunnels.

We can describe these two regions for a layer of a given thickness by examining the cracking phenomena for different pre-existing cracks during cooling from the processing temperature. If  $\frac{a}{t} \geq \left(\frac{a}{t}\right)_i$  (and  $\leq 1$ ), during cooling, the tensile stress will increase (eq 3) until the value of  $\frac{G_c E_1^*}{\sigma^2 t}$  crosses into the hatched area where the crack will suddenly extend and penetrate the adjacent layers. The extent of this penetration depends on the initial crack size; greatest penetration will occur when  $\frac{a}{t} \approx \left(\frac{a}{t}\right)_i$ . Further cooling will cause the crack to tunnel when  $\frac{G_c E_1^*}{\sigma^2 t} < \frac{\pi}{4}$ . If  $\frac{a}{t} < \left(\frac{a}{t}\right)_i$ , cooling into the hatched area will cause

the crack to extend and penetrate the adjacent layers and tunnel at the same time. In both cases, further cooling will cause the tunneled crack to continue to penetrate the adjacent layers. The final extent of crack penetration will be given by eq (4). Although continued penetration should occur by continuous, stable crack extension, the observation (Fig. 4c) that more than one crack front is observed in the adjacent layers, suggests that further penetration during cooling is a sudden event.

We can also use Fig. 7 to interpret crack extension for the case where the laminar material contains tensile layers of different thicknesses that has been cooled to room temperature, thus fixing the tensile stress. Similar to the case where the stress changes during cooling, two types of crack extension can occur. One where the value of  $\frac{G_c E_1^*}{\sigma^2 t}$  causes the pre-existing crack to propagate into the adjacent layers without tunneling, and one that cause both penetration and tunneling. Since the latter case is of more interest, one can rearrange eq (5) and show that tunnel cracks will only be observed when the thickness of the tensile layer is greater than a critical value

$$t \geq t_c = \left( \frac{4}{\pi} \right) \frac{G_c E_1^*}{\sigma^2}. \quad (6)$$

Thus, regardless of the magnitude of the stress developed during cooling, crack tunneling can not occur when  $t < t_c$ . It should also be noted that when  $t \geq t_c$  the probability of tunneling will depend on the size of the flaw that pre-exists within the tensile layer.

The above analysis assumes identical elastic properties for both materials. When the material that forms the adjacent layers is more compliant than the tensile layer (smaller elastic modulus), the normalized energy release rate increases and the slit crack will extend a greater distance into the bulk material. The opposite conditions occur when the tensile layer is more compliant than the adjacent material. This is similar to behavior seen in thin film cracking [26], where a compliant substrate will 'attract' a crack more than a stiff substrate. However, an interesting anomaly develops when the adjacent layer is much stiffer than the embedded layer. As seen in Fig. 8, the G function for the slit crack approaches zero on both sides of the interface. That is, the very stiff material blocks

extension of the slit crack beyond the embedded layer. The effect is real, but if either the residual stress or the layer thickness is large enough, this 'energy barrier' can be overcome, and the slit crack will extend into the bulk material.

#### 4.2 Comparison of Experiments with Analysis

Using the material parameters given in Table II, a predicted residual strain was calculated from equation (1). The initial temperature,  $T_i$ , used to determine the residual strain, was assumed to be 1200 °C instead of the sintering temperature of 1500 °C. This assumption was made because previous studies [27,28] have shown that zirconia exhibits significant plasticity above 1200 °C. Therefore, it can be postulated that the  $\text{Zr(Y)O}_2$  layers were sufficiently plastic to maintain a zero stress state above 1200 °C. Although the temperature where crack extension occurred during cooling is unknown, room temperature was selected as the final temperature,  $T_f$ . While tunnel cracking may occur at higher temperatures, the analysis suggests that crack will continue to penetrate the adjacent layer during cooling. Predicted values of residual stress were determined by substituting the results from eq. (1) into eq. (3). The results from eq. (3) for various compositions of  $\text{Al}_2\text{O}_3/\text{Zr(Y)O}_2$  were then inserted into eq. (6) to determine the critical layer thicknesses. The effect of the elastic mismatch between the embedded layers of  $\text{Zr(Y)O}_2$  and the bulk material was considered. However, based on finite element analysis by Ho and Suo [14], the value of  $Z$ , the driving force for crack propagation, does not change appreciably over the experimental range of the Dundurs Parameter,  $\alpha_D$  ( $-0.3 < \alpha_D < -0.1$ ). The values of the predicted critical thickness for various compositions are compared to the observed critical thicknesses for embedded layers of  $t\text{-Zr(3Y)O}_2$  and  $c\text{-Zr(8Y)O}_2$  in Figures 5a and b, respectively.

In Figure 5a, the predicted values of the critical thickness are in reasonable agreement with the observed critical thicknesses, i.e. agreement within a factor of 2 to 3. The predicted critical thickness is not a conservative solution: the predicted values are *larger* than the experimental results. This is because the tunnel cracks apparently



propagate at higher temperatures than assumed in the analysis. The fracture toughness of t-Zr(3Y)O<sub>2</sub> decreases with increasing temperature. [32]<sup>f</sup> Therefore, the fracture toughness of the t-Zr(3Y)O<sub>2</sub> layer during tunneling is lower than the value measured at room temperature. Using the room temperature value for fracture toughness for t-Zr(3Y)O<sub>2</sub> overestimates the critical thickness for crack extension.

Figure 5b shows the results of c-Zr(8Y)O<sub>2</sub>, which is not transformation-toughened and therefore its fracture toughness is not expected to be as temperature dependent as the tetragonal phase. As shown, the observed critical layer thickness is in good agreement with predicted values, and the predicted values maintain a conservative solution (no tunnel cracks were observed below the predicted critical layer thickness).

Experimental observations of crack extension into 0.50/0.50-Al<sub>2</sub>O<sub>3</sub>/t-Zr(3Y)O<sub>2</sub> layer is shown in Fig. 6 and compared to theoretical predictions. On the basis of equation (6) and the relation  $G = K^2/E^*$  ( $K$  being the stress intensity factor), the slope of the plot should be constant and equal to  $K_{IC}/\sigma$ . Figure 6 shows that the slope is linear. Substituting the value of  $\sigma$  in the tensile layer of 567 MPa, the fracture toughness,  $K_{IC}$ , of the 0.50/0.50-Al<sub>2</sub>O<sub>3</sub>/t-Zr(3Y)O<sub>2</sub> layer was calculated to be 4.20 MPa·m<sup>1/2</sup>, which is smaller by  $\approx 25\%$  than previously reported values. [29,30]

Equation (6) assumes crack extension will occur when stress intensity factor,  $K$  is greater than the fracture toughness,  $K_{IC}$  of the adjacent layers. As the residual stress in the layer increases during cooling, and thus  $K$  at the crack tip increases, crack propagation should occur in a steady, continuous fashion, until room temperature. However, Fig. 4c shows two apparent 'jumps' in crack growth. There are two possible explanations for this behavior. First, there appears to be an 'energy barrier' that must be overcome to extend the tunnel crack a second time. That is, the crack must be 'overdriven' in order for it to extend farther into the adjacent alumina/zirconia layers. In this circumstance, equation (6) will underestimate the  $K_{IC}$  of the adjacent layers since the measured crack extension is less than the expected crack length should the crack grow stably. Or, since the kinetics of crack

---

<sup>f</sup> This is due to a lower driving force for transformation

extension is not addressed in eq. (6), it is possible the crack propagated unstably to some length where  $K \ll K_{Ic}$ . From there, further cooling is required to build up a stress concentration at the crack tip in order for further extension to occur.

## 5. Conclusion

An existing analysis for the extension of cracks in a layer under biaxial, residual tension is reported to take into account crack penetration into the adjacent layers. Theoretical predictions of the critical layer thickness for tunnel cracks were then compared to experimental observations and were found to be in reasonable agreement and useful as a conservative solution in fabricating crack-free laminates. Experimental measurements of crack extension into the adjacent layers were found to be in good agreement with the analysis of a slit-crack.

**Acknowledgements:** The authors would like to thank Alex Blum of Harrop Industries, Dr. Wolfgang Pompe of the Max-Planck Institute in Dresden, and Dr. David Marshall of the Rockwell Science Center for measuring the coefficient of thermal expansion. The authors would also like to express their gratitude towards Mark Cornish for his assistance in electron microscopy and sample preparation.

## References

1. G. Behrens and A.H. Heuer, "Microstructural Characterization of Cofired Tungsten-Metallized High-Alumina Electronic Substrates," *J. Am. Ceram. Soc.*, 75 [10] 2815-24 (1992).
2. S. Bruno, D. Swanson, and I. Burn, "High-Performance Multilayer Capacitor Dielectrics from Chemically Prepared Powders," *J. Am. Ceram. Soc.*, 76 [5] 1233-41 (1993).
3. S. Iwanaga, T. Fujita, R. Iwamura, H. Yokono, S. Ueno, and S. Suzuki, "Fabrication Process of Air-Fuel Ratio Sensor by Using the Green-Sheet Laminating Materials,"

Advances in Ceramics: Multilayer Ceramic Devices, Vol. 19, ed. by J. Blum and W. R. Cannon, 49-68, The American Ceramic Society, Westerville, OH, 1987.

4. T. Chartier, J. L. Besson, and P. Boch, "Mechanical Properties of  $\text{ZrO}_2\text{-Al}_2\text{O}_3$  Laminated Composites," Advances in Ceramics: Science and Technology of Zirconia III, Vol. 24B, ed. by S. Somiya, N. Yamamoto, and H. Yanagida, 1131-38, The American Ceramic Society, Westerville, OH, 1988.

5. J. Requena, R. Moreno, and J. S. Moya, "Alumina and Alumina/Zirconia Multilayer Composites Obtained by Slip Casting," *J. Am. Ceram. Soc.*, 72 [8] 1511-13 (1989).

6. D. B. Marshall, J. J. Ratto, and F. F. Lange, "Enhanced Fracture Toughness in Layered Microcomposites of  $\text{Ce-ZrO}_2$  and  $\text{Al}_2\text{O}_3$ ," *J. Am. Ceram. Soc.*, 74 [12] 2979-87 (1991).

7. P. Sarkar, X. Huang, and P. S. Nicholson, "Structural Ceramic Microlaminates by Electrophoretic Deposition," *J. Am. Ceram. Soc.*, 75 [10] 2907-909 (1992).

8. C. J. Russo, M. P. Harmer, H. M. Chan, and G. A. Miller, "Design of a Laminated Ceramic Composite for Improved Strength and Toughness," *J. Am. Ceram. Soc.*, 75 [12] 3396-400 (1992).

9. W. Cutler, F. Zok, and F. F. Lange, "Processing and Mechanical Properties of High Temperature Hybrid Multilayer Composites," manuscript in preparation.

10. (a). H. Kirchner, J. Conway, and A.E. Segall, "Effect of Joint Thickness and Residual Stresses on the Properties of Ceramic Adhesive Joints: I, Finite Element Analysis of Stresses in Joints," *J. Am. Ceram. Soc.*, 70 [2] 104-09 (1987).

(b). W. Zdaniewski, J. Conway, and H. Kirchner, "Effect of Joint Thickness and Residual Stresses on the Properties of Ceramic Adhesive Joints: II, Experimental Results," *J. Am. Ceram. Soc.*, 70 [2] 110-18 (1987).

11. S. Johnson and D. Rowcliffe, "Mechanical Properties of Joined Silicon Nitride," *J. Am. Ceram. Soc.*, 68 [9] 468-72 (1985).

12. A. Levy, "Thermal Residual Stresses in Ceramic-to-Metal Brazed Joints," *J. Am. Ceram. Soc.*, 74 [9] 2141-47 (1991).

13. T. Garino and H. Bowen, "Deposition and Sintering of Particle Films on a Rigid Substrate," *J. Am. Ceram. Soc.*, 70 [11] C315-C317 (1987).
14. S. Ho and Z. Suo, "Tunneling Cracks in Constrained Layers," *J. of App. Mech.*, 60 [12] 890-94 (1993).
15. M.S. Hu and A.G. Evans, "The Cracking and Decohesion of Thin Films on Ductile Substrates," *Acta Metall.*, 37 [3] 917-25 (1989).
16. S. Ho, C. Hillman, F.F. Lange, and Z. Suo, "Surface Cracking in Layers Under Biaxial, Residual Compressive Stress," *J. Am. Ceram. Soc.*, currently under review
17. J.C. Chang, F.F. Lange, and D.S. Pearson, "Viscosity and Yield Stress of Alumina Slurries Containing Large Concentrations of Electrolyte," *J. Am. Ceram. Soc.*, 77 [1] 19-26 (1994).
18. B.V. Velamakanni, J.C. Chang, F.F. Lange, and D.S. Pearson, "New Method for Efficient Colloidal Particle Packing via Modulation of Repulsive Lubricating Hydration Forces," *Langmuir*, 6, 1323-25 (1990).
19. J.C. Chang, F.F. Lange, D.S. Pearson, and J.P. Pollinger, "Pressure Sensitivity for Particle Packing of Aqueous  $\text{Al}_2\text{O}_3$  Slurries vs. Interparticle Potential," *J. Am. Ceram. Soc.*, 77 [5] 1357-60 (1994).
20. J.C. Chang, B.V. Velamakanni, F.F. Lange, and D.S. Pearson, "Centrifugal Consolidation of  $\text{Al}_2\text{O}_3$  and  $\text{Al}_2\text{O}_3/\text{ZrO}_2$  Composite Slurries vs. Interparticle Potentials: Particle Packing and Mass Segregation," *J. Am. Ceram. Soc.*, 74 [9] 2201-04 (1991).
21. W. Kreher and W. Pompe, Physical Research: Internal Stresses in Heterogeneous Solids, Vol. 9, Akademie-Verlag, Berlin, 1989.
22. T. Nose and T. Fujii, "Evaluation of Fracture Toughness for Ceramic Materials by a Single-Edge-Pre-cracked-Beam Method," *J. Am. Ceram. Soc.*, 71 [5] 328-33 (1988).
23. J.E. Srawley, "Wide Range Stress Intensity Factor Expressions for ASTM E399 Standard Fracture Toughness Specimens," *Int. J. Fract.*, 12, 475-6 (1976).

24. J.W. Hutchinson and Z. Suo, "Mixed Mode Cracking in Layered Materials," *Advances in Applied Mechanics*, Vol. 29, ed. by J.W. Hutchinson and T. Y. Wu, Academic Press, 1991.
25. H. Tada, P. C. Paris, and G. R. Irwin, *The Stress Analysis of Cracks Handbook*, 2nd ed., Del Research, St. Louis, MO, 1985.
26. T. Ye, Z. Suo, and A.G. Evans, "Thin Film Cracking and the Roles of Substrate and Interface," *Int. J. Solids Structures*, 29 [21] 2639-48 (1992).
27. T. Nieh and J. Wadsworth, "Superplastic Behaviour of a Fine-Grained, Yttria-Stabilized, Tetragonal Zirconia Polycrystal (Y-TZP)," *Acta Metall. Mater.*, 38 [6] 1121-33 (1990).
28. D.S. Cheong, A. Dominguez-Rodriguez, and A.H. Heuer, "High-Temperature Plastic Deformation of  $Y_2O_3$ -Stabilized  $ZrO_2$  Single Crystals: III. Variation in Work Hardening Between 1200 and 1500° C," *Phil. Mag. A*, 63 [3] 377-88 (1991).
29. E. Bischoff and M. Ruhle, "Microcrack and Transformation Toughening of Zirconia-Containing Alumina," Advances in Ceramics: Science and Technology of Zirconia III, Vol. 24B, ed. by S. Somiya, N. Yamamoto, and H. Yanagida, 635-43, The American Ceramic Society, Westerville, OH, 1988.
30. K. Tsukuma, T. Takahata, and M. Shiomi, "Strength and Fracture Toughness of Y-TZP, Ce-TZP, Y-TZP/ $Al_2O_3$ , and Ce-TZP/ $Al_2O_3$ ," Advances in Ceramics: Science and Technology of Zirconia III, Vol. 24B, ed. by S. Somiya, N. Yamamoto, and H. Yanagida, 721-28, The American Ceramic Society, Westerville, OH, 1988.
31. Y.S. Touloukian, ed., Thermophysical Properties of Matter: Thermal Expansion of Nonmetallic Solids, Vol. 13, Plenum Publishing, New York, 1977.
32. F.F. Lange, "Transformation Toughening, Part 4: Fabrication, Fracture Toughness and Strength of  $Al_2O_3$ - $ZrO_2$  Composites," *J. Mater. Sci.*, 17, 247-54 (1982).
33. Dr. Dieter Schneider, private communication

34. R.L. Lehman, "Overview of Ceramic Design and Process Engineering," Engineered Materials Handbook: Ceramics and Glasses, Vol. 4, ASM International, Materials Park, OH, 1991, p. 30.
35. B. Eigenmann, B. Scholtes, and E. Macherauch, "Roentgenologic Stress Determination in Ceramics and Metal-Ceramic Composites, Theory and Applications," *Mat.-wiss.u.Werksstofftech.*, 20, 314-25 (1989).
36. K. Wefers and C. Misra, Oxides and Hydroxides of Aluminum, Alcoa Laboratories, Pittsburgh, 1987.

**Table I: Average Coefficient of Thermal Expansion**  
**(20 °C - 1000 °C)(10<sup>-6</sup>/K)**

	Average CTE (Harrop)	Average CTE (Rockwell)	Average CTE (Theory)
Zr(Y)O <sub>2</sub>	11.30	11.4	N/A
0.33Al/0.66Zr	10.56	N/A	10.05
0.5Al/0.5Zr	9.51	9.5	9.66
0.66Al/0.33Zr	9.31	N/A	9.11
0.9Al/0.1Zr	8.64	N/A	8.62
Al <sub>2</sub> O <sub>3</sub>	8.39 §	N/A	N/A

---

§ The coefficient of thermal expansion for alumina was taken from ref. [31]

Table II: Material Properties

	$\alpha$ ( $10^{-6}/K$ ) 25 - 1500 °C	E (GPa)	$\nu$	$K_{Ic}$ (MPa*m <sup>1/2</sup> )
Zr(Y)O <sub>2</sub>	$9.75 \times 10^{-6} + (4.00 \times 10^{-9})T - (1.44 \times 10^{-12})T^2$	205 [32]	0.32 [35]	6.2 <sup>h</sup> , 2.1 <sup>i</sup>
0.33Al/0.66Zr	$8.97 \times 10^{-6} + (3.38 \times 10^{-9})T - (3.90 \times 10^{-13})T^2$	260 <sup>j</sup>	0.32	-
0.5Al/0.5Zr	$7.06 \times 10^{-6} + (7.80 \times 10^{-9})T - (5.83 \times 10^{-12})T^2$	300 [32,33]	0.32 [35]	-
0.66Al/0.33Zr	$7.29 \times 10^{-6} + (4.28 \times 10^{-9})T - (1.28 \times 10^{-12})T^2$	320 <sup>j</sup>	0.32	-
0.9Al/0.1Zr	$6.42 \times 10^{-6} + (5.64 \times 10^{-9})T - (1.92 \times 10^{-12})T^2$	360 <sup>j</sup>	0.32	-
Al <sub>2</sub> O <sub>3</sub>	$6.6 \times 10^{-6} + (4.1 \times 10^{-9})T - (8.9 \times 10^{-13})T^2$ [31]	380 [34]	0.32 [36]	-

<sup>h</sup> Value for t-Zr(3Y)O<sub>2</sub>

<sup>i</sup> Value for c-Zr(8Y)O<sub>2</sub>

<sup>j</sup> These values of elastic modulus were calculated by rule of mixtures



## Figure Captions

Figure 1: (a) An embedded layer of  $\text{Zr(Y)O}_2$  sandwiched between two bulk layers of  $\text{Al}_2\text{O}_3/\text{Zr(Y)O}_2$ . (b) During cooling from processing temperatures, the  $\text{Zr(Y)O}_2$  layer would shrink more due to its higher coefficient of thermal expansion,  $\alpha$ . (c) Due to strong interfaces, the  $\text{Zr(Y)O}_2$  layer is constrained from shrinking, producing a biaxial, residual tensile stress in the embedded layer.

Figure 2: Plot of coefficient of thermal expansion (CTE) versus temperature (0 °C - 1000 °C) for  $\text{Zr(Y)O}_2$  and various compositions of  $\text{Al}_2\text{O}_3/\text{Zr(Y)O}_2$ .

Figure 3: (a) SEM micrograph of an open tunnel crack in an embedded layer of  $\text{Zr(Y)O}_2$ . (b) The crack surface of the open tunnel crack, composed of smooth, round grains. (c) Crack healing of the crack extension into the bulk material of  $\text{Al}_2\text{O}_3/\text{Zr(Y)O}_2$ .

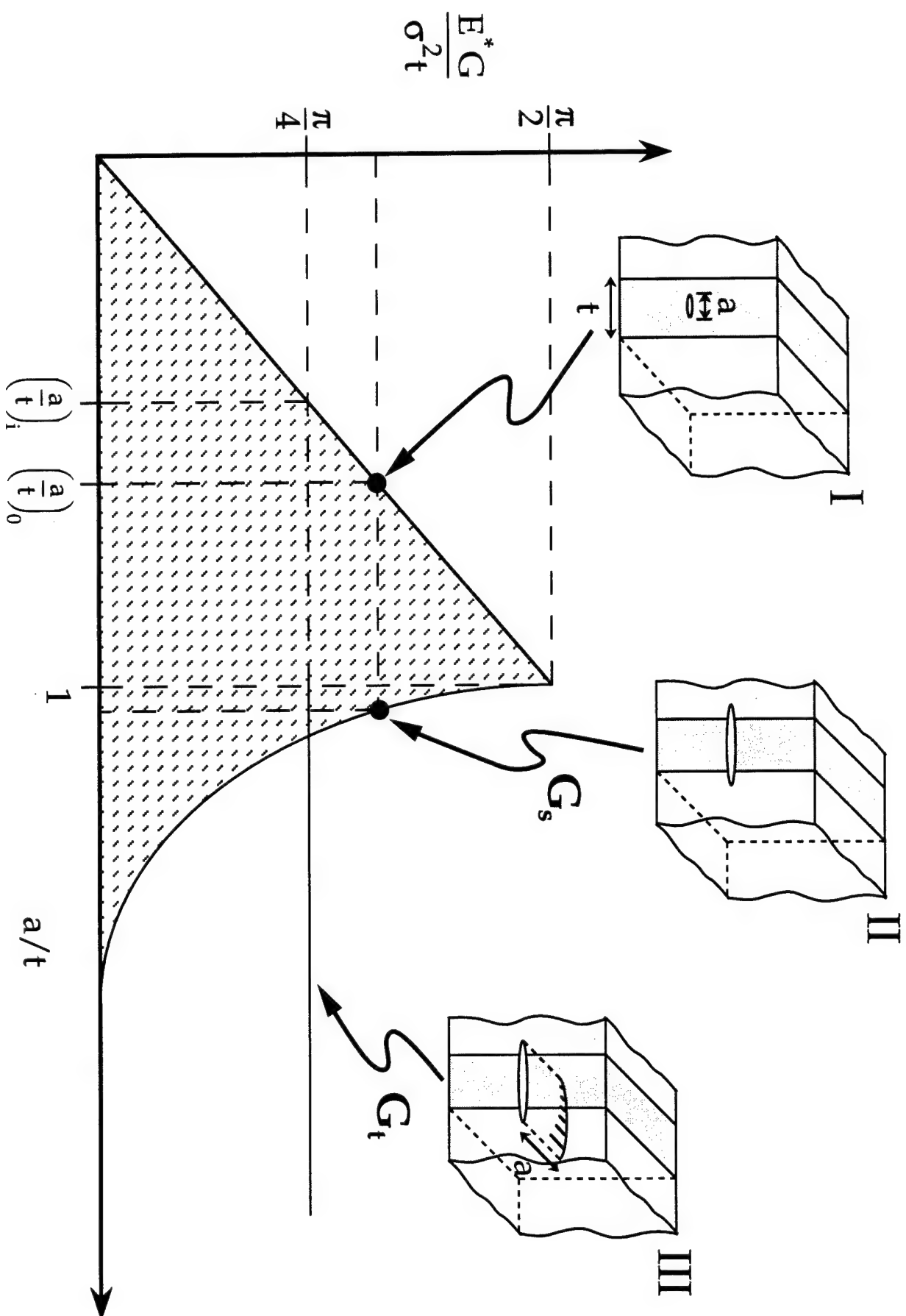
Figure 4: (a) SEM micrograph of a closed tunnel crack in an embedded layer of  $\text{Zr(Y)O}_2$ . (b) The crack surface of the closed tunnel crack, composed of heavily faceted grains. (c) The fracture surface of a closed tunnel crack, showing two distinct crack front positions during crack extension into the adjacent  $\text{Al}_2\text{O}_3/\text{Zr(Y)O}_2$  layer.

Figure 5: (a) Plot of the critical layer thickness ( $t_c$ ) observed in t- $\text{Zr(3Y)O}_2$  versus predicted critical layer thickness for varying percentage of  $\text{Al}_2\text{O}_3$  in the adjacent layer (the greater the percentage of  $\text{Al}_2\text{O}_3$  in the adjacent layer the greater the residual stress in the embedded t- $\text{Zr(3Y)O}_2$  layer). (b) Plot of the critical layer thickness ( $t_c$ ) observed in c- $\text{Zr(8Y)O}_2$  versus predicted critical layer thickness for varying percentage of  $\text{Al}_2\text{O}_3$  in the adjacent layer.

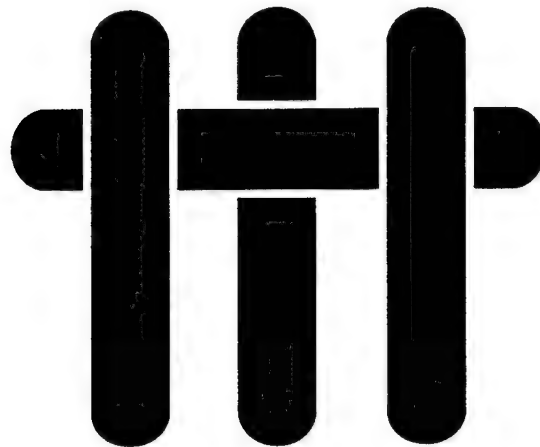
Figure 6: Plot of crack length,  $a$  versus embedded layer thickness,  $t$ . This plot is arranged based upon eq. (6). The slope of the plot is linear and is equal to  $K_{Ic}/\sigma_r$ .

Figure 7: I. Consider a flaw in an embedded layer,  $(a/t)_0 > (a/t)_i$ . II. The strain energy release rate for the flaw,  $G_s$ , becomes greater than the critical strain energy release rate,  $G_c$ , during cooling, and the crack extends into the adjacent layers without tunneling. III. Further cooling causes the strain energy release rate for tunneling,  $G_t$ , to become greater than  $G_c$  and the crack tunnels through the embedded layer. If the initial flaw size,  $(a/t)_0$  is less than  $(a/t)_i$ , the crack will extend and tunnel at the same time.

Figure 8: (a) The change in the normalized energy release rate of a flaw,  $G$ , in an embedded layer with increasing crack length,  $a$ , when  $E_2/E_1=1$  and when  $E_2/E_1>1$ . As the crack approaches the interface ( $a/t=1$ ), the normalized  $G_s$  reduces to 0, creating an "energy barrier", which can be overcome when the residual stress or the embedded layer thickness is large.



# **M A T E R I A L S**



**Technical Report Number 17**

## **Crack Bifurcation in laminar Ceramic Composites**

**M. Oechsner, C. Hillman, and F. F. Lange**

**Sent to: J. Amer. Ceramic Society**

**February 1, 1994 through January 31, 1995**

**Office of Naval Research**

**Grant No. N00014-90-J-1441**

**Fred F. Lange**

**Principal Investigator**

**Materials Department  
University of California  
Santa Barbara, CA 93106**

# Crack Bifurcation in Laminar Ceramic Composites

M. Oechsner\*, C. Hillman<sup>†</sup> and F. F. Lange<sup>†</sup>

Material Department  
University of California at Santa Barbara  
Santa Barbara, CA 93106

## Abstract

Crack bifurcation was observed in laminar ceramic composites when cracks entered thin  $\text{Al}_2\text{O}_3$  layers sandwiched between thicker layers of  $\text{Zr}(\text{12Ce})\text{O}_2$ . The  $\text{Al}_2\text{O}_3$  layers contained a biaxial, residual, compressive stress of  $\approx 2$  GPa developed due to differential contraction upon cooling from the processing temperature. The  $\text{Zr}(\text{12Ce})\text{O}_2$  layers were nearly free of residual, tensile stresses because they were much thicker than the  $\text{Al}_2\text{O}_3$  layers. The ceramic composites were fabricated by a green tape and co-densification method. Different specimens were fabricated to examine the effect of the thickness of the  $\text{Al}_2\text{O}_3$  layer on the bifurcation phenomena. Bar specimens were fractured in 4-point bending. When the propagating crack encountered the  $\text{Al}_2\text{O}_3$  layer, it bifurcated as it approached the  $\text{Zr}(\text{12Ce})\text{O}_2/\text{Al}_2\text{O}_3$  interface. After the crack bifurcated, it continued to propagate close to the center line of the  $\text{Al}_2\text{O}_3$  layer. Fracture of the laminate continued after the primary crack reinitiated to propagate through the next  $\text{Zr}(\text{12Ce})\text{O}_2$  layer, where it bifurcated again as it entered the next  $\text{Al}_2\text{O}_3$  layer. If the loading was stopped during bifurcation, the specimen could be unloaded prior to complete fracture. Although the residual stresses were nearly identical in all  $\text{Al}_2\text{O}_3$  layers, crack bifurcation was only observed when the layer thickness was greater than  $\approx 70 \mu\text{m}$ .

\* Diplomarbeit, Universität Karlsruhe, Institut für Werkstoffkunde I,  
Aufgabensteller: Prof. O. Vöhringer

---

<sup>†</sup> Member, American Ceramic Society

## 1. Introduction

Two different classes of crack deflecting composites are known that are made of brittle components. One is composed of brittle, but extremely strong components (viz., fibers) within a brittle matrix. In this type of composite, a crack deflecting interface exists between the fibers and matrix which allows cracks to extend through the matrix, but not through the fibers. [1] In this well known class of composites, once the matrix is saturated with cracks, the low modulus, high strength fibers fail at a high strain, either in flexural or tensile loading, to impart damage tolerance.

The second class is composed of a components that need not be strong, which are bonded together with a crack deflecting phase. Some of these composites occur in nature and have a plate-like architecture that include shell [2,3] and teeth. For these natural composites, the brittle entities are single crystal plates of either calcite, aragonite or hydroxyapite and the crack deflecting phase is a bio-polymer. Others are man-made to include laminates bonded together with a crack deflecting interphase material [4-7], materials described as 'fibrous monoliths' [8,9], and fiber composites with low density matrices [10]. In all of these cases the key feature that imparts apparent damage tolerance is the presence of an interphase between brittle components that supports crack extension as the interphase induces crack deflection. In general, composites in this second class exhibit different stress-strain characteristics under flexural and tensile loading. Notably, under flexural loading, the sequential crack extension through the 'brittle' components and crack deflection along the interphase gives rise to a series of step-like drops in the stress-strain response instead of a single, catastrophic drop characteristic of brittle materials that do not contain crack deflecting interphases. [6] When the crack deflection phenomena is present, the nominal failure strain is substantially higher than the failure strain measured in uniaxial tension. [11]

Some understanding of the crack deflection phenomena exists. Evans et al. [1] and He and Hutchinson [12] have considered the effect of an interface between two dissimilar materials (e.g., matrix/fiber interface). Their analysis concerns the case of a crack that exists in one material (e.g., matrix) with its front residing at the interface. Their analysis defines the conditions where the crack will extend along the interface instead of through the adjacent material; it includes the effect of the elastic mismatch between the two material. Later, He and Evans [13] modify the analysis to include the effect of a compressive stress in the adjacent material. The higher the compressive stress in the adjacent material (fiber), the more likely a crack will deflect along the interface.

More recently, [14] a phenomena was reported at first appeared unrelated to the

problem of crack deflection. This phenomenon was the formation of an edge crack along the center line of the layer under compression. As described below, this edge cracking phenomenon now appears to be directly related to a new crack defection mechanism, i.e., the bifurcation of a crack as it enters a compressive layer. To our knowledge, this bifurcation phenomenon has never been described before, and it may be important to the development of new ceramic composites. The following paragraphs will describe how the experiments to uncover the bifurcation phenomena were initiated.

Consider a ceramic laminate consisting of thin layers of one material sandwiched between thicker layers of another. In general, since the thermal expansion coefficients of the two materials are different, residual strain can develop during cooling from the fabrication temperature. The residual strain in thin layer is given by

$$\epsilon_r = \int_{T_i}^{T_f} (\alpha_E - \alpha_M) dT \quad (1)$$

where  $T_i$  and  $T_f$  are the initial and final temperatures during cooling and  $\alpha_E$  and  $\alpha_M$  are the coefficients of thermal expansion (CTE) for the thin layer material and the adjacent, thick layer material, respectively. The biaxial residual stress in the thin layer can be calculated as [14]

$$\sigma_R = \epsilon_r E_E' \left[ 1 + \frac{t_E}{t_M} \frac{E_E'}{E_M'} \right]^{-1}, \quad (2)$$

where  $E_i' = \frac{E_i}{1 - \nu_i}$  and  $E$  and  $\nu$  are Young's modulus and Poisson's ratio of the two materials,  $t_E$  and  $t_M$  are the thickness of the thin and adjacent layers.

In previous experiments, Ho et al. [14] observed edge cracks on the surface of the thin layers that were under nominal, residual compressive stress due to the biaxial constraint of adjacent, thicker layer with a larger CTE. These edge cracks appeared near the center of the layer (Fig. 1), propagating into the layer and running parallel to the center line. They showed that although biaxial compressive stresses exist in the layer far from the free surface, the stress distribution near the free surface is triaxial. Specifically, the component of the triaxial stress perpendicular to the center line of the layer,  $\sigma_{yy}$ , is a highly localized tensile stress which diminishes in magnitude from the surface to the interior.

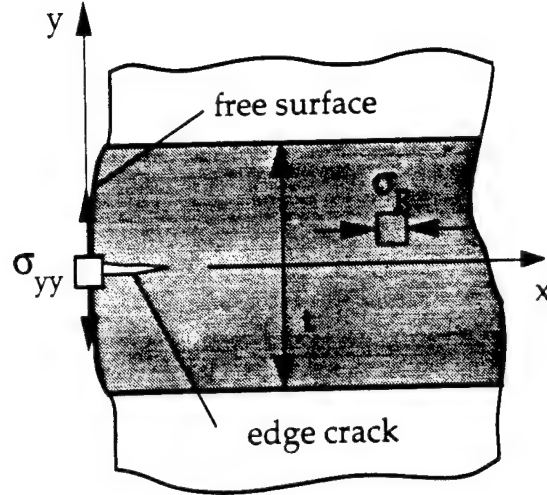


Figure 1: Tensile stresses at the free surface of a layer which is under biaxial compressive residual stress far away from the surface.

The magnitude of the tensile stress,  $\sigma_{yy}$ , along the centerline of the layer is given by [14]

$$\sigma_{yy}(x)|_{y=0} = \frac{2}{\pi} \left[ \theta - \frac{1}{2} \sin 2\theta \right] \sigma_R, \quad (3)$$

where

$$\tan \theta = \frac{t}{2x}, \quad (4)$$

and  $\sigma_R$  is the absolute value of the residual biaxial compressive stress far from the free surface. Note that the stress distribution along the centerline is strongly dependent on the thickness  $t$  of the embedded layer. Ho *et al.* [14] observed that the occurrence of edge cracks was dependent on the thickness of the embedded layer and the magnitude of the residual compressive stress in the embedded layer. They developed a strain energy release rate function for a crack in this localized, tensile stress field

$$G = \frac{0.34 \sigma_R^2 (1 - \nu^2)}{E} t. \quad (5)$$

The critical layer thickness below which edge cracking does not occur is thus given by

$$t_c = \frac{G_c E}{0.34 (1 - \nu^2) \sigma_R^2}, \quad (6)$$



where  $G_c$ ,  $E$ , and  $\nu$  are the critical strain energy release rate, Young's modulus, and Poisson's ratio of the thin layer material, respectively.

To understand the thinking that lead to experiments concerning crack bifurcation and its possible relation to the edge cracking phenomenon outlined above, consider a crack propagating through a laminate shown in Fig. 2.

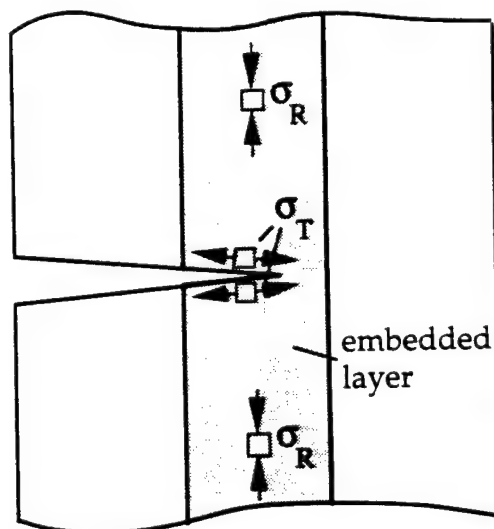


Figure 2: Propagating crack in a laminate under residual compressive stress.

When a crack propagates through the laminate, it creates a free surface. When it approaches a layer that is under a residual compressive stress,  $\sigma_R$ , it creates a situation similar to the free edge of a laminate, as discussed previously. The tensile stress,  $\sigma_T$ , which now arises due to the introduction of the free surface, may cause the propagating crack to bifurcate into the compressive layer. Because this behavior is similar to the edge cracking problem, there is expected to be a critical layer thickness for this phenomenon, below which no crack bifurcation will occur.

## 2. Experimental Method

**Table 1: Material Properties**

	$\alpha$ ( $10^{-6}$ / K) 25-1500 °C	Young's modulus E (GPa)	Poison's ratio $\nu$
Al <sub>2</sub> O <sub>3</sub>	9.0 [15]	380 [16]	0.32 [17]
Zr(12Ce)O <sub>2</sub>	11.5 [18]	205 [19]	0.32 [19]

Thin layers of Al<sub>2</sub>O<sub>3</sub> were sandwiched between much thicker Zr(12Ce)O<sub>2</sub> layers. Table 1 lists material properties for both materials. Laminates were formed with two plastic, green tapes<sup>a</sup>, each containing one of the two ceramic powders. The thicknesses of the green tapes were 35  $\mu$ m for the Zr(12Ce)O<sub>2</sub> tape and either 30  $\mu$ m or 20  $\mu$ m for the Al<sub>2</sub>O<sub>3</sub> tape (two different batches were used). The tapes were cut and then assembled to assure a thickness ratio of Al<sub>2</sub>O<sub>3</sub>/Zr(12Ce)O<sub>2</sub> < 0.1. The stacked sheets were sealed in a plastic bag<sup>b</sup> containing a plastic tube to evacuate air during warm pressing (150°C, 18 MPa for 1 hour). After warm pressing, the bonded, green laminate was placed in a special binder burnout oven and heated to 350°C at a very slow ramp rate in order to avoid cracking due to rapid sublimation. After binder burnout, the laminate was fully sintered at 1500 °C for 3 hours. Table 2 lists the heating rates for binder burnout and densification.

**Table 2: Heating Rates for Binder Burnout and Densification**

	temperature range	ramp rate
<b>binder burnout:</b>	room temperature - 180 °C	1 °C / min.
	180 °C - 350 °C	1.2 °C / hour (0.02 °C / min.)
	350 °C - room temperature	furnace cooled
<b>densification:</b>	room temperature - 1500 °C	2 °C / min.
	1500 °C - room temperature	5 °C / min.

<sup>a</sup> DSM Solutech, Netherlands, brand name Solufill™ (Solufill™ is a polymer film containing 20 vol.-% ceramic powder, 30 vol.-% organic binder and 50 vol.-% porosity)

<sup>b</sup> Kapton™, Du Pont

The laminates were machined into bar specimens for mechanical testing (length: 30 - 60 mm, width: 2.5 - 7 mm, thickness: 2 - 4 mm). The surface was polished down to 1  $\mu\text{m}$  in order to observe the edge of the  $\text{Al}_2\text{O}_3$  layers in the scanning electron microscope<sup>c</sup> (SEM), before and after fracture. The specimens were loaded in four-point bend to initiate crack propagation perpendicular to the  $\text{Al}_2\text{O}_3$  layers.

### 3. Results and Discussion

The residual stresses due to differential shrinkage during cooling was calculated using eq. (2) and the material properties listed in Table 1. The biaxial compressive stress in the  $\text{Al}_2\text{O}_3$  layers was calculated as  $\sim 1.9$  GPa and the residual biaxial tensile stress in the  $\text{Zr}(\text{12Ce})\text{O}_2$  layers was calculated as  $\sim 90$  MPa. Piezospectrographic data ( $\text{Cr}^{+3}$  fluorescence in  $\alpha\text{-Al}_2\text{O}_3$ ) obtained by He and Clarke [20, 21] on the surface of the bifurcated  $\text{Al}_2\text{O}_3$  layers revealed a compressive stress of 2.09 GPa. This is within reasonable agreement of calculated values.

SEM observations of the  $\text{Al}_2\text{O}_3$  layers revealed edge cracks in all of the layers ( $\geq 30$   $\mu\text{m}$ ) prior to fracture. This was expected since eq. (6) suggests that the critical thickness for the  $\text{Al}_2\text{O}_3$  layers should be  $\approx 18$   $\mu\text{m}$ , using a  $G_c$  for  $\text{Al}_2\text{O}_3$  of  $58 \text{ J/m}^2$  [22]. The depth of the edge cracks observed in the SEM were only revealed for those layers that produced bifurcation as reported below.

The strength of the specimens loaded to failure was dependent on whether the outer material (layer under maximum tensile stress) was either a thick layer (usually  $\approx 800$   $\mu\text{m}$ ) of  $\text{Zr}(\text{12Ce})\text{O}_2$  or a thin layer ( $\approx 50$   $\mu\text{m}$ ) of  $\text{Al}_2\text{O}_3$ .  $\text{Zr}(\text{12Ce})\text{O}_2$  was the outer layer for most of the specimens tested; they failed within the stress range of 480 to 550 MPa. Higher strengths (650 and 700 MPa) were measured when the outer layer was  $\text{Al}_2\text{O}_3$ . It is assumed that these higher strengths are due to the high residual compressive stresses that exist in the  $\text{Al}_2\text{O}_3$  outer layer. The outer  $\text{Al}_2\text{O}_3$  layers did not contain edge cracks nor did they produce any bifurcation. In no case were flaw populations controlled to optimize strength. A linear stress-strain behavior was observed in all cases.

Crack bifurcation could be observed with the unaided eye. When cracks bifurcated at thicker  $\text{Al}_2\text{O}_3$  layers, the macroscopic fracture path included the  $\text{Al}_2\text{O}_3$  layer and crack propagation through the next  $\text{Zr}(\text{12Ce})\text{O}_2$  layer initiated at some distance from the initial crack path. For two specimens, the mechanical testing machine was turned off and the partially

---

<sup>c</sup> Jeol 840, Tokyo Japan

fractured specimen was unloaded before the crack, which had bifurcated in at least one layer, could reinitiate the fracture process and extend through remaining specimen.

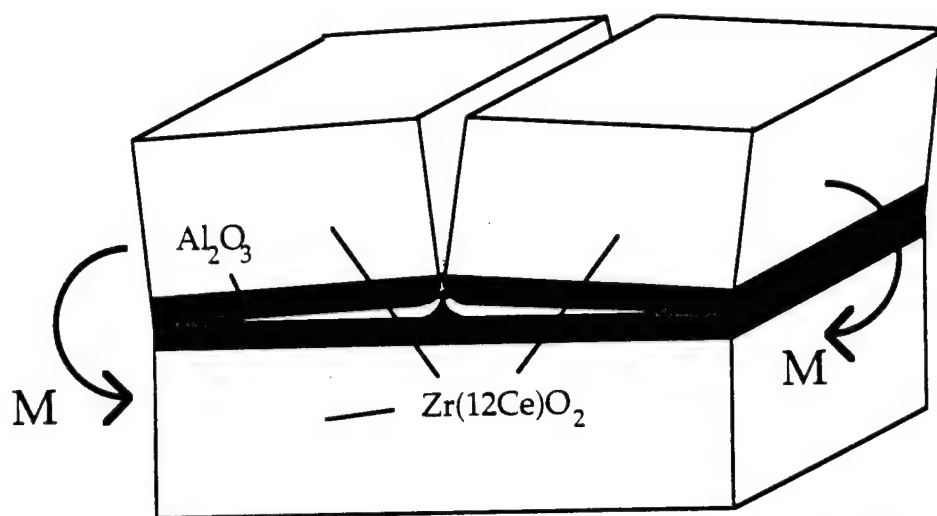


Figure 3: Schematic of crack bifurcation as the crack enters the  $\text{Al}_2\text{O}_3$  layer.

Figure 3 is a schematic of the bifurcated crack path to help explain the SEM observations shown in Figs. 4 and 5, which are different SEM views of the same  $\text{Al}_2\text{O}_3$  fracture layer produced by crack bifurcation. Figure 4 shows the cusp-shaped 'mountain' that extends across the specimen, from one edge crack to the other. This cusp 'mountain' is produced as the crack makes a gradual,  $90^\circ$  turn upon entering the  $\text{Al}_2\text{O}_3$  layer in the two directions that extend along the layer (see Fig 3). Figure 5 illustrates a top view of the same cusp; it terminates at the position where edge cracks had previously extended, i.e., it marks the extent of the edge cracks ( $\sim 0.6$  mm, for the case shown). The white areas in both SEM micrographs are  $\text{Zr(12Ce)O}_2$ , whereas the darker areas are  $\text{Al}_2\text{O}_3$ . Both Figs. 4 and 5 show that the crack began to bifurcate within the much thicker  $\text{Zr(12Ce)O}_2$  layer; namely the white 'snow' on the 'mountain peak' is  $\text{Zr(12Ce)O}_2$ . Also, both figures show that as the crack bifurcates within the  $\text{Al}_2\text{O}_3$  layer (dark material), it nearly extends to the 'bottom' interface between the two materials, which is clearly seen by the bright  $\text{Zr(12Ce)O}_2$  patches on the fracture surface (not illustrated in Fig. 3). Since no bright  $\text{Zr(12Ce)O}_2$  patches are observed further along the  $\text{Al}_2\text{O}_3$  layer (not shown), the crack appears to seek the mid-plane of the  $\text{Al}_2\text{O}_3$  layer as it continues to extend. The interaction of the pre-existing edge cracks and the bifurcating crack were clear from the fracture topography (not shown in the micrographs). The thickness of the  $\text{Al}_2\text{O}_3$  layer shown in Figures 4 and 5 is  $\approx 76$   $\mu\text{m}$  and the layer thickness of the  $\text{Zr(12Ce)O}_2$  layer is  $\approx 800$   $\mu\text{m}$ . When the  $\text{Al}_2\text{O}_3$  layer was  $> 90$   $\mu\text{m}$ , most of the specimens failed by delamination during machining. One specimen that did survive produce a bifurcated cusp which was only a small fraction of the specimen width, suggesting the depth of the pre-existing edge cracks were

nearly half the specimen width.

Bifurcation was not observed, when the  $\text{Al}_2\text{O}_3$  layers were too thin. This is illustrated with a specimen that contained 3  $\text{Al}_2\text{O}_3$  layers (see Fig. 6) where the center layer ( $\approx 33 \mu\text{m}$ ) was approximately half the thickness of the two outer layers ( $\approx 76 \mu\text{m}$ ). Calculations using eq. (2) based on the measured thicknesses of the  $\text{Zr}(\text{12Ce})\text{O}_2$  and  $\text{Al}_2\text{O}_3$  layers and their physical properties given in Table 1 suggested that the residual, biaxial compressive stresses in the thinner  $\text{Al}_2\text{O}_3$  layer at the center of the specimen was 1.98 GPa whereas the compressive stress in the two outer layers was slightly smaller, 1.83 GPa.

Figure 6 illustrates a portion of the fracture specimen, where crack bifurcation was observed for the two thicker layers, but not for the thinner layer. Also shown, the applied bending moment was released before the specimen completely failed; thus the third  $\text{Al}_2\text{O}_3$  layer supports a bifurcated crack, but has not completely failed. When the crack that initiated on the surface of the  $\text{Zr}(\text{12Ce})\text{O}_2$  layer propagated to the first  $\text{Al}_2\text{O}_3$  layer ( $\approx 76 \mu\text{m}$ ), it bifurcated and propagated in the  $\text{Al}_2\text{O}_3$  layer near the centerline. Note that the fracture parts of the first  $\text{Zr}(\text{12Ce})\text{O}_2$  layer, still attached at the far ends of the specimen (not shown), are bent upwards. It can be seen that the specimen was elastically bent, apparently due to the release of the large residual compressive stresses, as shown in Fig. 6, stored in the specimen during cooling from the fabrication temperature. Approximately one-half of the first  $\text{Al}_2\text{O}_3$  layer is still well bonded to the 'bottom' surface of first  $\text{Zr}(\text{12Ce})\text{O}_2$  layer. As shown in Fig. 7, the crack reinitiated in the first, delaminated  $\text{Al}_2\text{O}_3$  layer away from the original crack path, and propagated through the second  $\text{Zr}(\text{12Ce})\text{O}_2$  layer.

As the crack reached the second  $\text{Al}_2\text{O}_3$  layer in the middle of the specimen ( $\approx 33 \mu\text{m}$ ), it passed through this layer without any bifurcation as shown in Fig. 8. The jog shown in Fig. 8, occurred only on the surface of the sample due to the pre-existing edge cracks. When the propagating crack reached the third  $\text{Al}_2\text{O}_3$  layer ( $\approx 76 \mu\text{m}$ ), the crack bifurcated again and extended through the middle of the third  $\text{Al}_2\text{O}_3$  layer as shown in Fig. 9. The specimen was unloaded at this point to preserve the specimen.

Other specimens containing  $\text{Al}_2\text{O}_3$  layers with a thickness of  $33 \mu\text{m}$  did not show crack bifurcation behavior. In addition, specimens containing  $\text{Al}_2\text{O}_3$  layers with a thickness  $< 70 \mu\text{m}$  also showed no crack bifurcation, even though the calculated magnitude of the residual compressive stress was slightly higher (due to a smaller  $\text{Al}_2\text{O}_3/\text{Zr}(\text{12Ce})\text{O}_2$  thickness ratio). These observations show that layer thickness is an important factor in crack bifurcation behavior, and similar to the strain energy release rate function that governs edge cracking (eq. (5)). Experimental results strongly suggest that crack bifurcation must be proportional to the product of the residual stress,  $\sigma_R$ , and layer thickness,  $t$ . That is, bifurcation will occur when  $\sigma_R^2 t > \text{critical value}$ . However, further research is required to uncover this relation.

#### 4. Conclusion

Experimental results show that crack bifurcation is dependent on the thickness of the embedded  $\text{Al}_2\text{O}_3$  layer under residual compressive stress. The influence of the magnitude of the residual compressive stress was not investigated. However, based on the experimental results presented here, analytical calculations by Xu et al. [23] predict that crack bifurcation is caused by compressive stress in a laminar material and therefore the magnitude of that stress should have some influence on crack bifurcation behavior. Xu et al. also show that crack bifurcation is influenced by the mismatch of the elastic moduli and the mismatch in the fracture toughness of the two bonded materials on either side of the interface. Currently, their analytical calculations do not predict any effect of the layer thickness on crack bifurcation.

This discovery of crack bifurcation should lead to a better design for crack deflecting fiber coatings and a better understanding of a new composite material recently discovered [10], where the fibers and matrix are well bonded, and crack deflection occurs within a low density matrix that is subjected to residual compressive stresses.

#### References

- [1] A.G. Evans, M.Y. He, and J.W. Hutchinson, "Interface Debonding and Fiber Cracking in Brittle Matrix Composites", *J. Am. Ceram. Soc.*, 72, [12], 2300-2303, (1989).
- [2] J.D. Currey and A.J. Kohn, "Fracture in the Crossed-Lamellar Structure of Conus Shells," *J. Mater. Sci.*, 11, pp. 1615-73 (1976).
- [3] V.J. Laraia and A.H. Heuer, "Novel Composite Microstructure and Mechanical Behavior of Mollusk Shells," *J. Am. Ceram. Soc.*, 72 [11] pp. 2177-79 (1989).
- [4] W.J. Clegg, K. Kendall, N.McN. Alford, T.W. Burton and J.D. Birchall, "A Simple Way to Make Tough Ceramics, *Nature* [347], No. 6292, pp. 455-57, Oct. 4 (1991).
- [5] C.A. Folsom, F.W. Zok, F.F. Lange and D.B. Marshall, "Mechanical Behavior of a Laminar Ceramic/Fiber-Reinforced Epoxy Composite," *J. Am. Ceram. Soc.*, 75 [11] pp. 2969-75 (1992).
- [6] C. A. Folsom, F. W. Zok and F. F. Lange, "On the Flexural Properties of Brittle Multilayer Materials: Modeling," *J. Am. Ceram. Soc.*, 77 [3] 689-96 (1994).
- [7] C. A. Folsom, F. W. Zok and F. F. Lange, "On the Flexural Properties of Brittle Multilayer Materials: II Experiments," *J. Am. Ceram. Soc.*, 77 [8] 2081-87 (1994).
- [8] S. Baskaran, S. D. Nunn, D. Popovic, J. W. Halloran, "Fibrous Monolithic Ceramics. I. Fabrication, Microstructure, and Indentation Behavior," *J. Am. Ceramic Soc.*, 76, [9] 2209-

16 (1993)

- [9] S. Baskaran and J.W. Halloran, "Fibrous monolithic ceramics. II. Flexural strength and Fracture Behavior of the Silicon Carbide/Graphite System," *J. Am. Ceramic Soc.*, 76 [9] 2217-24 (1993).
- [10] W. C. Tu , F. F. Lange and A. G. Evans "Processing of Damage Tolerant, Oxidation Resistant CMC's by a Precursor Infiltration and Pyrolysis Method," *Mat. Eng. and Sci.* (in press)
- [11] J. Holmes and J.W. Halloran, University of Michigan, <http://www.engin.umich.edu/~usama/> (May, 1995)
- [12] M.Y. He and J.W. Hutchinson, "Crack Deflection at an Interface between Dissimilar Elastic Materials", *Int. J. Solids. Structures*, 25 [9], 1053-1067, (1989)
- [13] M.Y. He and A. G. Evans, "Crack Deflection at an Interface between Dissimilar Elastic Materials: Role of Residual Stresses", *Int. J. Solids. Structures*, 31 [24] 3443-3455 (1994).
- [14] S. Ho, C.D. Hillman, F.F. Lange, and Z. Suo, "Surface Cracking in Layers Under Biaxial, Residual Compressive Stress", *J. Am. Ceram. Soc.* (in press)
- [15] Y.S. Touloukian (ed.), "Thermophysical Properties of Matter: Thermal Expansion of Nonmetallic Solids", Vol. 13, Plenum Publishing, New York, (1977).
- [16] R.L. Lehman, "Overview of Ceramic Design and Process Engineering", *Engineered Materials Handbook: Ceramics and Glasses*, Vol. 4, ASM International, Materials Park, OH, p.30, (1991)
- [17] K. Wefers and C. Misra, "Oxides and Hydroxides of Aluminum", Alcoa Laboratories, Pittsburgh, (1987).
- [18] P. Scardi, R. Di Maggio, L. Lutterotti, "Thermal Expansion Anisotropy of Ceria-stabilized Zirconia", *J. Am. Ceram. Soc.*, 75, [10], 2828-32, (1992)
- [19] F. F. Lange, "Transformation Toughening, Part IV: Fabrication, Fracture Toughness and Strength of  $\text{Al}_2\text{O}_3$  -  $\text{ZrO}_2$  Composites", *J. Mater. Sci.*, 17, 247-254, (1982)
- [20] J. He and D.R. Clarke, private communication.
- [21] Q. Ma and D. R. Clarke, "Piezo-Spectroscopic Determination of Residual Stresses in Polycrystalline Alumina", *J. Am. Ceram. Soc.*, 77, 298-302 (1994)
- [22] C. Hillman, Z. Suo, and F.F. Lange, "Cracking in Laminates Subjected to Biaxial Tensile Stresses," submitted to *J. Am. Ceram. Soc.*
- [23] X.-P. Xu, M. Oechsner, Z. Suo and F.F. Lange, "Crack Deflection in Oxide - Oxide Composites with strong Interfaces", *to be published*

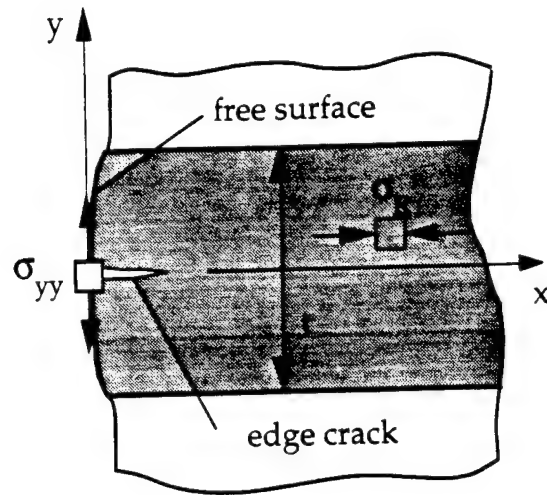


Figure 1: Tensile stresses at the free surface of a layer which is under biaxial compressive residual stress far away from the surface.



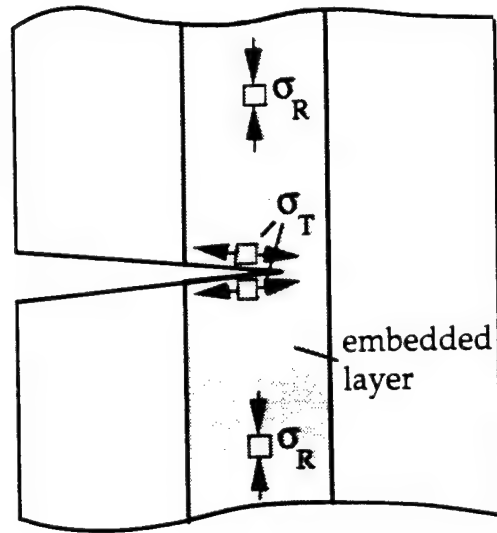


Figure 2: Propagating crack in a laminate under residual compressive stress.

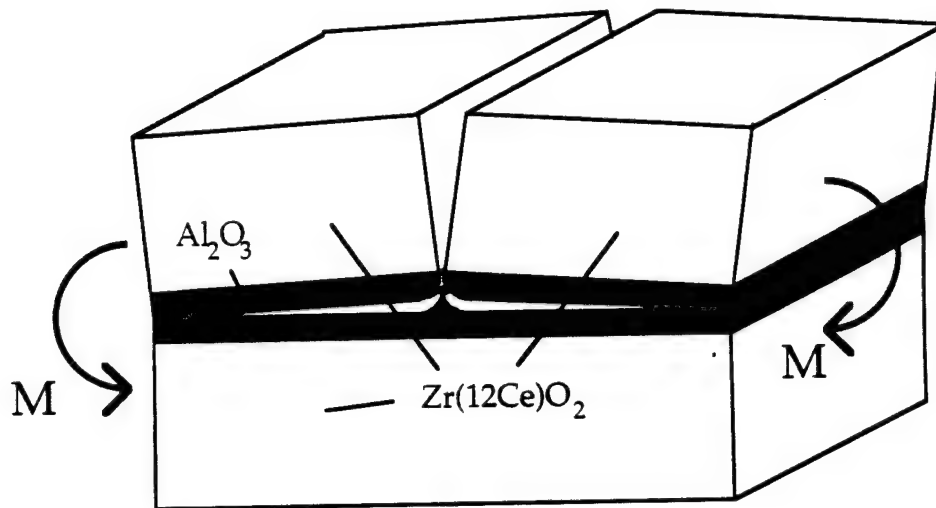
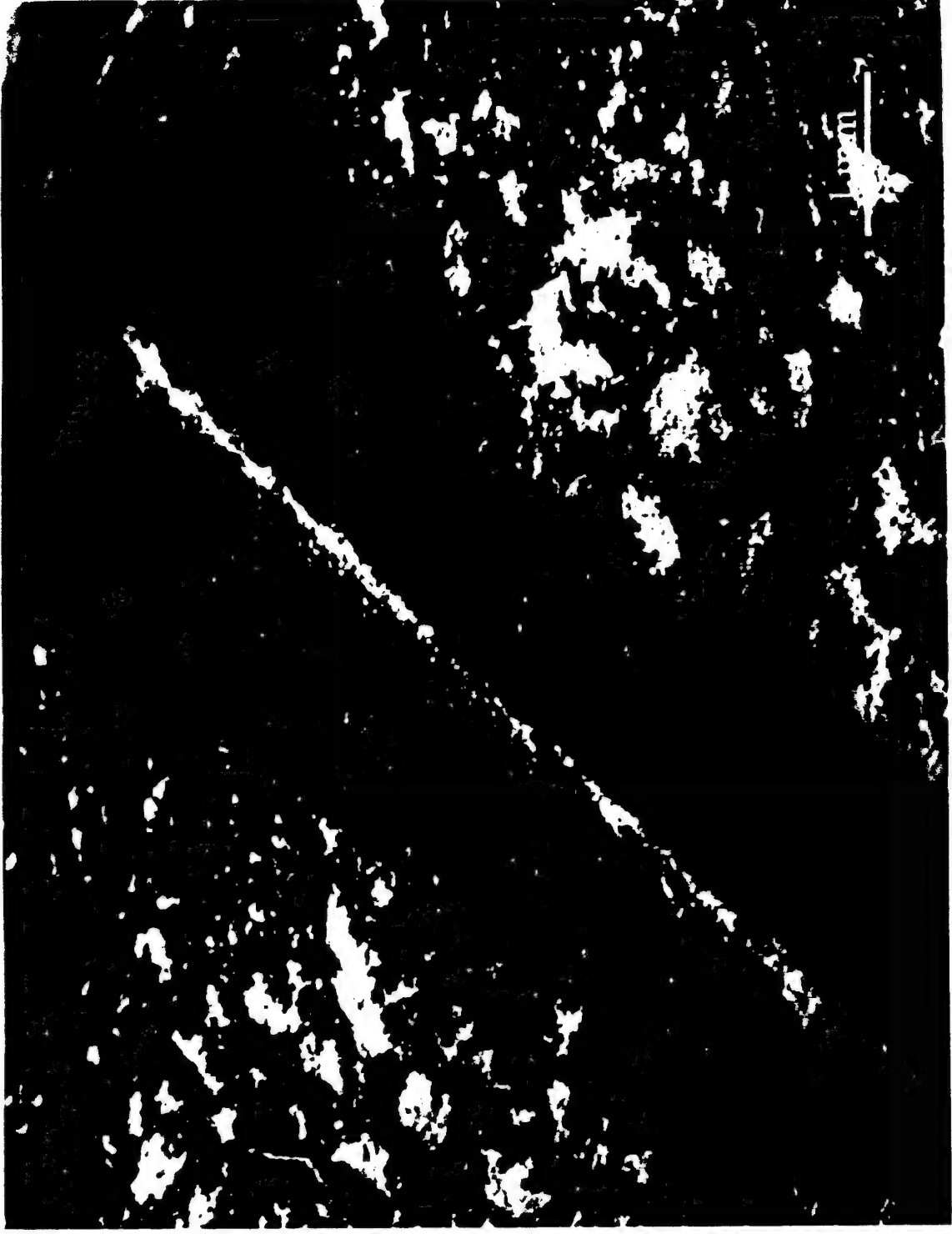
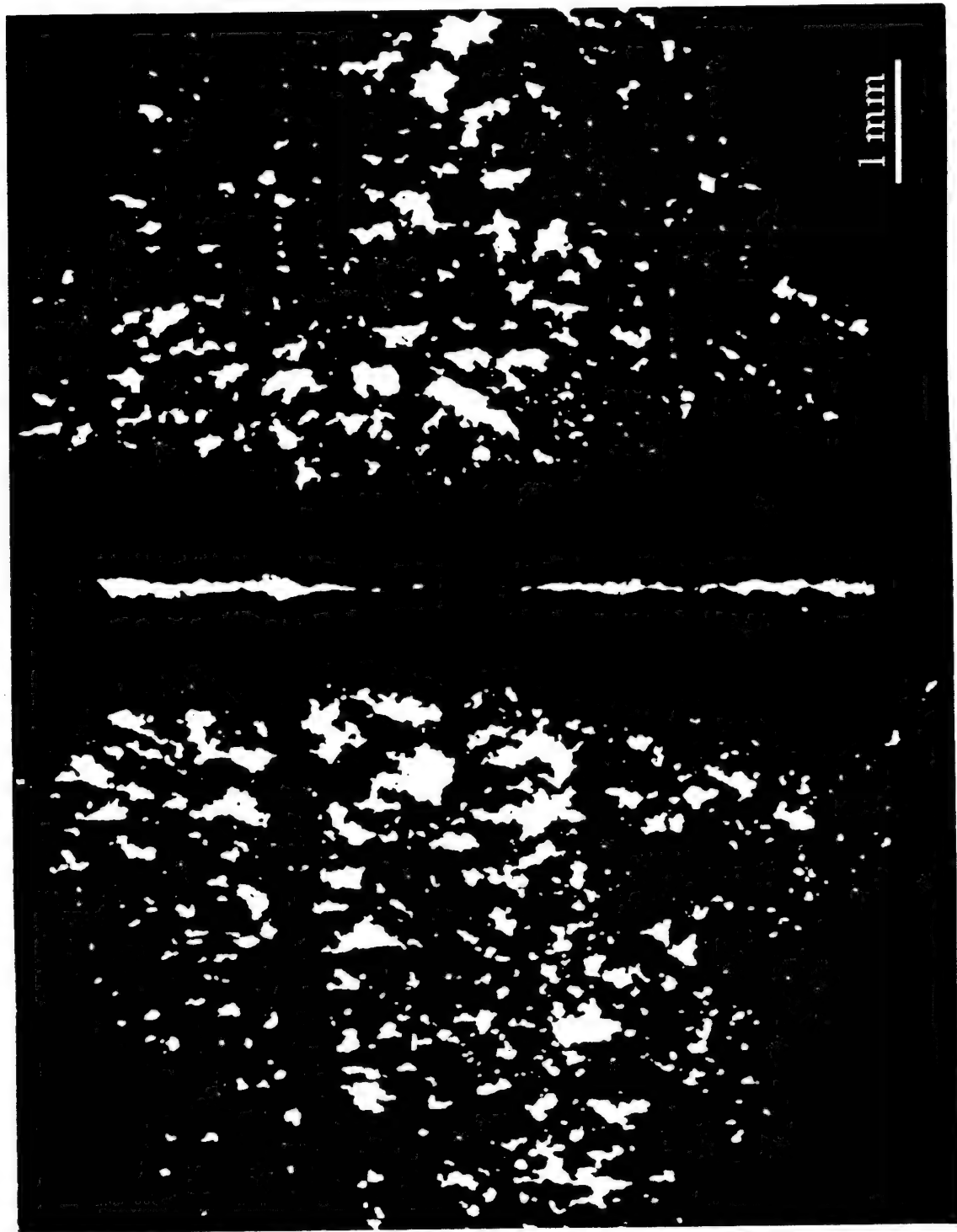


Figure 3: Schematic of crack bifurcation as the crack enters the  $\text{Al}_2\text{O}_3$  layer.



*Darkener et al. Fig 4*



*Oechina et al Fig 5*



Oechsner et al Fig 6



As-generated Fig 7

